Annual Research Journal

Electrical Engineering
Research Experience for Undergraduates

Vol. X

August 2012

National Science Foundation
Grant No. EEC-1062984

PENNSTATE

Department of Electrical Engineering
University Park, Pennsylvania

EEREU Annual Research Journal

Sven Bilén (editor)

Volume X
Published in 2012 by
The Department of Electrical Engineering
The Pennsylvania State University
University Park, Pennsylvania 16802

NSF EE REU Site Program Contact

121 Electrical Engineering East
The Pennsylvania State University
University Park, PA 16802
Telephone (814) 863-6315
Fax (814) 865-7065
E-Mail: eereu@engr.psu.edu
Web Site: http://www.ee.psu.edu/reu/

PREFACE

We are happy to present the ***2012 Annual Research Journal – Electrical Engineering Research Experience for Undergraduates, Vol. X.*** This volume contains highlights of the EEREU program activities for summer 2012 and twelve technical papers written by EEREU scholars as primary authors.

Summer 2012 marks our tenth year hosting the National Science Foundation–sponsored Research Experience for Undergraduates (REU) Site Program, in the Department of Electrical Engineering, Penn State. Twelve outstanding young men and women participated in this year's EEREU program at Penn State's University Park Campus. These EEREU scholars, selected from nation-wide applicants, consisted of college first-year, sophomore, or junior students with outstanding academic backgrounds and intense interests in exploring research in electrical engineering and related areas.

During the nine-week summer program, EEREU students carried out research projects under the guidance of his or her faculty mentor(s), in laboratories hosted by the Department of Electrical Engineering and the Materials Research Institute at Penn State. The students also presented their research experience and findings at the 2012 Annual *EEREU Symposium*, held at University Park, in July 2012.

Besides research activities, the EEREU program organized an array of group activities including a ***Weekly Scientific Seminar Series*** that introduced a broad range of research topics to the REU students, a ***field trip program*** that offered EEREU students opportunities to visit prominent local and regional industrial and research sites, and a ***Weekly Workshop on Ethics and Entrepreneurship*** through which students were engaged in debate and analysis of issues in ethics and company start-ups in engineering. For more information about Penn State's EEREU program, please visit our website at: < http://www.ee.psu.edu/reu/ >.

We are confident that readers will find that the series of EEREU Journals showcases the achievement of our EEREU students and effective mentorship provided by the faculty and graduate student mentoring teams. We are also hopeful that this publication will not only document original research contributions that are of value for scientific dissemination and publication, but it may also stimulate more college students to consider research careers and to pursue graduate studies in electrical engineering.

W. Kenneth Jenkins and Sven G. Bilén
Co-Directors of the NSF EE REU Site Program
Dept. of Electrical Engineering
The Pennsylvania State University

July 2012
University Park, PA

TABLE OF CONTENTS

Research Articles (* indicates REU student author)

2012 NSF EEREU FACULTY & STAFF MEMBERS

Faculty Mentors:

Prof. Sven Bilén, Co-Director
Prof. Ken Jenkins, Co-Director
Prof. Michael Lanagan
Prof. Zhiwen Liu
Prof. John Mathews
Prof. Vishal Monga
Prof. Joan Redwing
Prof. David Salvia
Prof. Victor Pasko
Prof. Jeff Schiano
Prof. Srinivas Tadigadapa
Prof. Julio Urbina

Prof. Phil Boyer, Entrepreneurship Chair
Ms. Amy Freeman, Adviser, Engineering Diversity
Mrs. Lena Getman, Administration
Prof. Andy Lau, Ethics Chair
Prof. Jack Mitchell, Seminar Chair
Prof. David Salvia, Activities and Web Chair
Mr. Thomas Tyson, Assistant Director

NSF EE REU 2012 Summer Program
Research Seminar Series

Room 101 E E East, 9:40–10:30 AM

(*Seminars are on Wednesday unless otherwise noted*)

Department of Electrical Engineering
The Pennsylvania State University, University Park, PA 16802

Date	*Topic*	*Speaker*
June 6, 2012	Integrating Nanowire-based Sensors with CMOS Electronics Using Directed Self Assembly	Theresa Mayer
June 13, 2012	Sensors Using Micro and Nanoscale Structures	Srinivas Tadigadapa
June 20, 2012	Magnetic Resonance Imaging	Jeff Schiano
June 27, 2012	What's Next? Graduate School, of Course!	David Salvia
July 5, 2012 (Thursday)	Systems Design Lab	Sven Bilén
July 11, 2012	Lightning-related Transient Luminous Events in the Middle Atmosphere	Victor Pasko
July 18, 2012	Emerging Techniques in Radar Remote Sensing: Cognitive Radars and Beyond	Julio Urbina
July 26, 2012 (Thursday)	2012 NSF EEREU Symposium	REU Students

NSF EEREU 2012 Summer Program
Ethics & Entrepreneurship Workshop

Room 101 E E East, 10:50–11:50 am, Wednesdays

Department of Electrical Engineering
Pennsylvania State University, University Park, PA 16802

Date	*Topic*	*Speaker*
June 6, 2012	Introduction to Ethics: The Responsible Business	Andy Lau
June 13, 2012	Intellectual Property Issues	Phil Boyer
June 20, 2012	Research Ethics	Andy Lau
June 27, 2012	Sustainability	Andy Lau
July 5, 2012 (note: Thurs.)	Student Entrepreneur Panel: "What's it take to be an entrepreneur?"	Erik Weir and Dan Weiss (Buzby Networks, LLC)
July 11, 2012	Ethics Issues in Entrepreneurship	Andy Lau
July 18, 2012	Getting Funding to Pursue Your Idea	Phil Boyer
July 25, 2012	Student Presentations on Tech Transfer Ideas of Research Projects	REU students

2012 NSF EE REU Field Trip Program
Academic/Industrial Sponsors and Tour Hosts

Department of Electrical Engineering
Penn State University, University Park, Pennsylvania

Breazeale Nuclear Reactor
Penn State University, University Park, Pennsylvania

Accuweather, Inc.
State College, Pennsylvania

Penn State Center for Sustainability
State College, Pennsylvania

State of the Art, Inc.
State College, Pennsylvania

Energy Efficiency Buildings HUB
Philadelphia, Pennsylvania

W. L. Gore and Associates
Elkton, Maryland

2012 NSF EE REU SYMPOSIUM

Final Program

8:30 am to 3:00 pm, Thursday, July 26, 2012
Room 101 Electrical Engineering East Building
Pennsylvania State University, University Park, PA 16802

Time	Sessions and Topics	Chairs and Speakers
8:30 – 8:55 am	**Symposium Registration (Refreshments Provided)**	**(Lena Getman/ Tom Tyson)**
8:55 – 9:00 am	**Welcome**	**Ken Jenkins**
9:00 – 10:00 am	**Session I** Session Chairs:	**Pasko/Urbina/ Monga**
9:00– 9:15	INVESTIGATION OF LONG-DELAYED SPRITE INCEPTION MECHANISM AND THE ROLE OF ELECTRON DETACHMENT (MENTOR: PASKO)	Jeremy Pachter
9:15 – 9:30	CORONA MODELING FOR LIGHTNING PROTECTION APPLICATIONS (MENTOR: PASKO)	Joe Tucker
9:30 – 9:45	ON THE ROLE OF TURBULENCE ON THE EVOLUTION OF SPECULAR METEOR ECHOES: STATISTICS (MENTOR: URBINA)	Carlos Mulero
9:45 – 10:00	JOINT SPARSITY BASED COLOR IMAGE CLASSIFICATION (MENTOR: MONGA)	Charles Jeon
10:00 – 10:15 am	**Coffee Break**	
10:15 – 11:30 am	**Session II** Session Chairs:	**Mathews/Bilén Jenkins/Schiano**
10:15 – 10:30	THERE AND BACK AGAIN—LUNAR ROBOTIC LAUNCH AND LANDING SYSTEM (MENTOR: MATHEWS)	François M. Rice
10:30 – 10:45	DESIGN OF THE GEOPEBBLE ACCESS POINT WIRELESS CONTROL SYSTEM AND SENSOR NETWORK (MENTOR: BILÉN)	Amanda Sweat
10:45 – 11:00	ADAPTIVE SIGNAL PROCESSING METHODS FOR REMOVING MATERNAL INTERFERENCE NOISE FROM FETAL ELECTRO-CARDIOGRAMS (MENTORS: JENKINS/SALVIA)	Jamilya Sultanova
11:00 – 11:15	OBSERVATION OF QUADRUPOLE RESONANCE TRANSITIONS USING A CONTINUOUS-WAVE SPECTROMETER (MENTOR: SCHIANO)	Jazmyne Claggett

2012 NSF EE REU SYMPOSIUM (cont.)

8:30 am to 3:00 pm,

Final Program

Thursday, July 26, 2012
Room 101 Electrical Engineering East Building
Pennsylvania State University, University Park, PA 16802

Time	Sessions and Topics	Chairs and Speakers
11:30 – 11:45 am	**(Group Photo – All are invited. Please plan to be available.)**	(Tom Tyson)
12:00 – 1:30 pm	**Luncheon (Nittany Lion Inn)**	
1:45 – 2:45 pm	**Session III** Session Chairs:	**Tadigadapa/Liu/ Khoo/Lanagan**
1:45 – 2:00	CHARACTERIZATION OF POROUS SILICON FOR MICROPYROTECHNIC APPLICATIONS (MENTOR: TADIGADAPA)	Alfredo Bermúdez
2:00 – 2:15	GROWTH OF PYRAMIDAL NANOWIRES ON ALUMINUM DIFFUSED SILICON WAFERS FOR PHOTOVOLTAIC DEVICES (MENTOR: REDWING)	Katelynn Jourdan
2:15 – 2:30	CHARACTERIZATION OF FLUORESCENT MICROSPHERES FOR USE AS A LASER GAIN MEDIUM AND RESONATOR (MENTOR: LIU)	Porter Beus
2:30 – 2:45	OPTIMIZATION OF ELECTROMAGNETIC COUPLING IN CERAMIC RESONATORS FOR MAGNETIC RESONANCE IMAGING APPLICATIONS (MENTOR: LANAGAN)	Matthew Pyrz
2:45 – 3:00 pm	**CONGRATULATIONS AND CONCLUDING REMARKS**	**Jenkins/Bilén**

3:00 pm Adjournment

Picnic at Sunset Park, 5:00 pm – sunset, ALL ARE INVITED

Resources:	Tom Tyson and Lena Getman
Special Notes:	Laser pointer, desktop PC and LCD PC projector are provided. Speakers please upload presentation files to EEREU group web in Angel by Wednesday, July 25. It is strongly recommended that speakers test-run presentation files for audio, video, or special applications on a Windows PC prior to their Thursday presentation. Each presentation is 15 minutes – chair introduction, questions, and answers included.

NSF EE REU PENN STATE Annual Research Journal Vol. X (2012)

INVESTIGATION OF LONG-DELAYED SPRITE INCEPTION MECHANISM AND THE ROLE OF ELECTRON DETACHMENT

Jeremy Pachter,* Jianqi Qin[+], and Victor Pasko[#]

Department of Electrical Engineering
The Pennsylvania State University, University Park, PA 16802

*Undergraduate Student of
Department of Physics
Brandeis University
Waltham, MA 02454

ABSTRACT

Sprites with extensive vertical streamer structures are spectacular luminous gas discharges in the mesosphere and lower ionosphere, and are usually produced by intense positive cloud-to-ground lightning discharges (+CGs) in the underlying thunderstorms. Sprite streamers spawn from electron density inhomogeneities in the ambient ionosphere, and often appear only several milliseconds after the causative +CGs that produce large charge moment changes in the first few milliseconds. Observations have also shown that in some sprite events, long-delayed sprites can be initiated more than 100 ms after the causative +CGs associated with small initial charge moment changes, followed by additional removal of thundercloud charge by continuing lightning current. Recently, long-delayed sprite ignition was studied by *Luque and Gordillo-Vazquez* [2011] using a chemical kinetic model, which suggested that the electron detachment processes might play a significant role in the production of long-delayed sprites. However, our results indicate that the detachment process decreases the dielectric relaxation time of the lightning-induced quasi-static electric field, suggesting that it is an unfavorable process in terms of sprite initiation. We also found that the attachment process is favorable for sprite initiation, which in conjunction with continuing current, enhances the mesospheric electric field for long-delay sprite initiation from preexisting inhomogeneities in the ambient ionosphere.

[+] Graduate Mentor
[#] Faculty Mentor

INTRODUCTION

Since their initial serendipitous image capture [*Franz et al*., 1990], large-scale upper atmospheric gas discharges known as sprites [*Sentman et al*., 1995] have been studied extensively. Sprites are large-scale optical manifestations of filamentary streamers [*Stanley et al*., 1999] initiated at mesospheric altitudes, usually by intense positive cloud-to-ground lightning discharges (+CGs) [*Lyons*, 1996]. Since the first high-speed video observations of sprites [*Stanley et al*., 1999], sprite streamer analysis has evolved with technological improvements in temporal and spatial resolution, revealing significant temporal relations with the causative +CGs [e.g., *Cummer and Fullekrug*, 2001; *Li et al*., 2008]. As a result, two classifications of sprites based on their time delays with respect to the onset of the causative +CGs have surfaced, namely short and long-delayed sprites; the former term describes sprites forming typically only several milliseconds after the causative +CGs, and the latter describes sprites with onset time up to 100s of milliseconds later [e.g., *Bell et al*., 1998; *Cummer and Fullekrug*, 2001; *Li et al*., 2008].

Pasko et al. [1997, 1998] proposed the conventional breakdown theory to account for the sprite phenomena, suggesting that sprites are produced by strong quasi-static lightning-induced electric fields at upper atmospheric altitudes. Since this electric field is linearly proportional to the lightning-induced vertical charge moment change, defined as the amount of charge Q transferred to ground by the lightning discharge times the altitude h_Q from which the charge was removed, the charge moment change (Qh_Q) is one of the most important parameters in sprite events. This theory was confirmed with the observations of *Hu et al.* [2007] over the timescale of short-delayed sprites, and the observations of *Cummer and Fullekrug* [2001, and references therein] and *Cummer and Lyons* [2005] over the timescale of long-delay sprites with continuing current identified as the primary mechanism in achieving the necessary charge moment changes. On the other hand, long-delayed sprite ignition was studied recently by *Luque and Gordillo-Vazquez* [2011] using a chemical kinetic model, which served to modify the conventional breakdown model to include the associated detachment process (see Reaction 4). The conclusion of this investigation suggested that this electron detachment process might play a significant role in the production of long-delayed sprites by releasing free electrons in the low electric field conditions. However, the role of electron detachment has not yet been quantitatively investigated in the previous literature. The present study is dedicated to the understanding of the inception mechanism of long-delayed sprites, particularly the role of the electron detachment and attachment processes, as well as the role of continuing lightning current.

NUMERICAL METHODS

Chemical Reactions

In the conventional breakdown model used prior to that of *Luque and Gordillo-Vázquez* [2011], free electrons are primarily released through electron

impact ionization of N_2 and O_2 [e.g., *Pasko et al*., 1997; *Liu and Pasko*, 2004; *Qin et al.*, 2012]:

$$e + \mathrm{N_2} \rightarrow 2e + \mathrm{N_2^+} \tag{1a}$$

$$e + \mathrm{O_2} \rightarrow 2e + \mathrm{O_2^+} \tag{1b}$$

Electron losses are primarily due to dissociative attachment to molecular oxygen:

$$e + \mathrm{O_2} \rightarrow \mathrm{O} + \mathrm{O^-} \tag{2}$$

This model defines the threshold breakdown field E_k as the field at which the ionization and attachment frequencies are equal [e.g., *Raizer*, 1991, p.135].

Electrons attached via process (2) cannot further ionize molecules, and are ignored in the model. However, over a short time scale, the O^- ions either form stable ozone ions by a three-body reaction

$$\mathrm{O^-} + \mathrm{O_2} + \mathrm{Z} \rightarrow \mathrm{O_3^-} + \mathrm{Z} \tag{3}$$

(Z is any species) or release electrons via associative detachment to N_2:

$$\mathrm{O^-} + \mathrm{N_2} \rightarrow \mathrm{N_2O} + e \tag{4}$$

Reaction (3) can be ignored at high altitudes because of lower air densities, and the importance of Reaction (4) was suggested recently by *Luque and Gordillo-Vázquez* [2011].

Chemical Reactions

To incorporate associative detachment in the conventional breakdown model, we shall assume that the air density is low enough to neglect Reaction (3). This is the case in the upper atmosphere. By combining the relevant reactions, we can model the growth rate of electrons as [*Luque and Gordillo-Vázquez*, 2011]:

$$\frac{1}{n_\mathrm{e}}\frac{\mathrm{d}n_\mathrm{e}}{\mathrm{d}t} = \nu_\mathrm{ion}(E/N) - \nu_\mathrm{attach}(E/N) + \eta\nu_\mathrm{detach}(E/N) \tag{5}$$

where n_e is the electron density, $\eta = n_O\text{-}/n_e$ is the ratio of O^- ion density to electron density, υ_{ion} is the ionization frequency, υ_{attach} is the two body attachment frequency, υ_{detach} is the detachment frequency, and E/N is the reduced electric field.

The growth rate of O^- ions can be calculated as follows:

$$\frac{1}{n_{\mathrm{e}}}\frac{\mathrm{d}n_{\mathrm{O}-}}{\mathrm{d}t} = \nu_{\mathrm{attach}}(E/N) - \eta\nu_{\mathrm{detach}}(E/N) \tag{6}$$

where $n_{\mathrm{O}-}$ is the number density of O^- ions.

To understand the role of associative detachment, we simulate the dynamics of the total electric field with respect to these important parameters. The electric field can be calculated as follows [*Luque and Gordillo-Vázquez*, 2011]:

$$\epsilon_0\frac{\mathrm{d}E}{\mathrm{d}t} = -\sigma E + J_T(t) \tag{7}$$

where σ is the local conductivity, ε_0 is the dielectric constant of free space, and $J_T(t)$ is a function of the cloud-to-ground current. To estimate J_T we adopt the approach in [*Luque and Gordillo-Vázquez*, 2011] and treat the field E_p created by the electric dipole $p = 2Qh_{\mathrm{Q}}$ as homogeneous in a layer far above the ground from altitude $z_0 = 65$ km to $z_1 = 80$ km. We treat the conductivity in the lower boundary of that layer to be low enough to neglect the conduction current, and

$$J_T = \epsilon_0\frac{\partial E_p}{\partial t} \tag{8}$$

The cloud electric field is approximated by averaging the lower and upper dipole fields,

$$E_p = \frac{Qh_Q}{\pi\epsilon_0}\left[\frac{1}{z_0^3} + \frac{1}{z_1^3}\right] \tag{9}$$

with the inclusion of an extra factor of 2 resulting from the complete screening of the field at ~ 80 km. Conductivity is defined as $\sigma = q_e n_e \mu_e$, where q_e is the elementary charge, μ_e is the mobility of free electrons at altitude h. The electron mobility μ_e, ionization frequency υ_{ion}, and two-body attachment frequency $\upsilon_{\mathrm{attach}}$ are defined as functions of the reduced electric field E/N using formulations of *Morrow and Lowke* [1997]. The detachment frequency $\upsilon_{\mathrm{detach}}$ is defined as a function of the reduced electric field E/N using formulations of *Luque and Gordillo-Vázquez* [2011].

It is important to note that in this simple model, the electric field at a given location changes only as a function of conductivity of the ambient medium, which mainly depends on the corresponding electron density [*Luque and Gordillo-Vázquez*, 2011]. The dielectric relaxation time τ is inversely proportional to the electron density:

$$\tau = \frac{\epsilon_0}{q_e n_e \mu_e} \tag{10}$$

By increasing the electron density, the dielectric relaxation time is decreased. As defined above, the electron density is affected by all the important chemical processes (i.e., ionization, attachment, and detachment processes) we seek to investigate. By removing and holding the contributions of certain reactions in our modeling, the resulting temporal variations of electron density and electric field at a given altitude provide means to investigate the roles of individual chemical reactions during the entire process.

SIMULATION RESULTS

The current moment waveform used in the present study is the same as that used by *Luque and Gordillo-Vázquez* [2011] and it was obtained by *Gamerota et al.* [2011] directly from observations of a lightning discharge on 3 July 2008 (see Figure 1). The sprite was initiated approximately 55 ms after the causative +CG at an altitude of ~75 km.

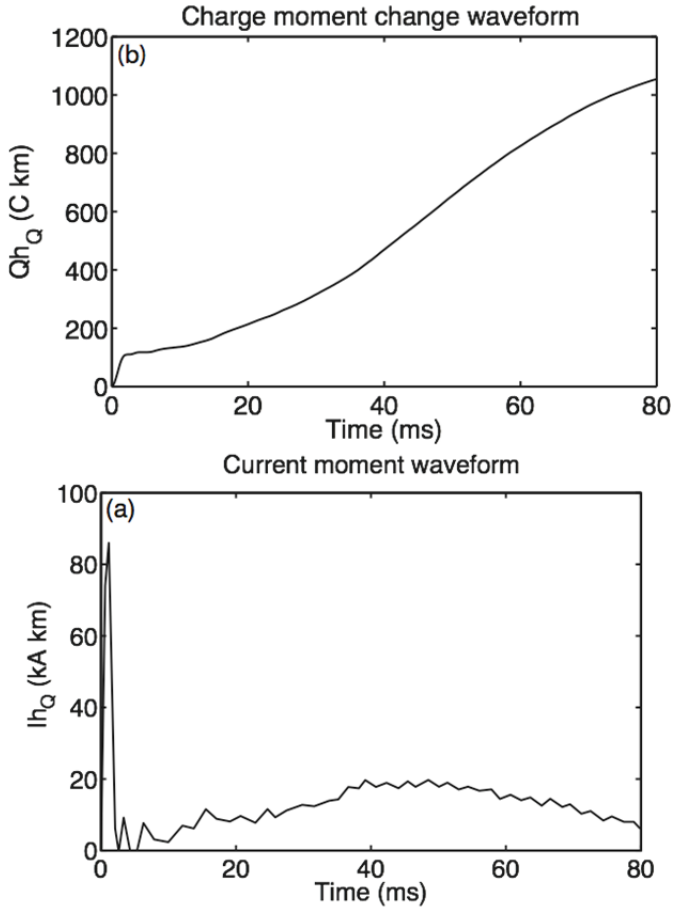

Figure 1: (a) Current moment (Ih_Q) waveform of a lightning discharge on July 3, 2008, [*Gamerota et al.*, 2011]. (b) Charge moment change (Qh_Q) waveform calculated by integrating the current moment over time.

Figure 2 shows the electron density variations at a 75 km altitude as a function of time associated with different combinations of ionization, attachment, and detachment processes. In the case of ionization only, the electron density increases slowly over time without experiencing any drop. At 80 ms it reaches a value of ~3.6 × 10^6 m^{-3}. With ionization and attachment processes, the electron density experiences a rapid decrease starting at 42 ms, reaches a minimum of ~3.8 m^{-3} at ~58 ms, and then has a dramatic spike of increase at ~66 ms to a maximum value of ~1.6 × 10^7 m^{-3}. In the case of full chemistry, the electron density drops only slightly between 43 and 51 ms, and then experiences a rapid growth between 52 and 67 ms to a maximum value of ~9 × 10^6 m^{-3}.

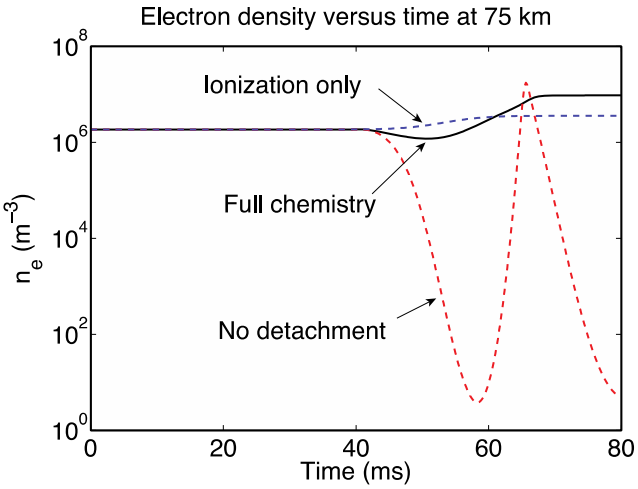

Figure 2: Temporal variations of the electron density at 75 km altitude.

Figure 3(a) shows the temporal variations of the dielectric relaxation time at 75 km altitude corresponding to the temporal variations of the electron density shown in Figure 2. In the cases of the full chemistry and ionization only processes, the peak dielectric relaxation time τ is much smaller than that of the ionization and attachment processes during most of the simulation time. The timescales of the ionization ($1/\upsilon_{ion}$), attachment ($1/\upsilon_{attach}$), and detachment ($1/[\eta\upsilon_{detach}]$) processes are illustrated in Figure 3(b).

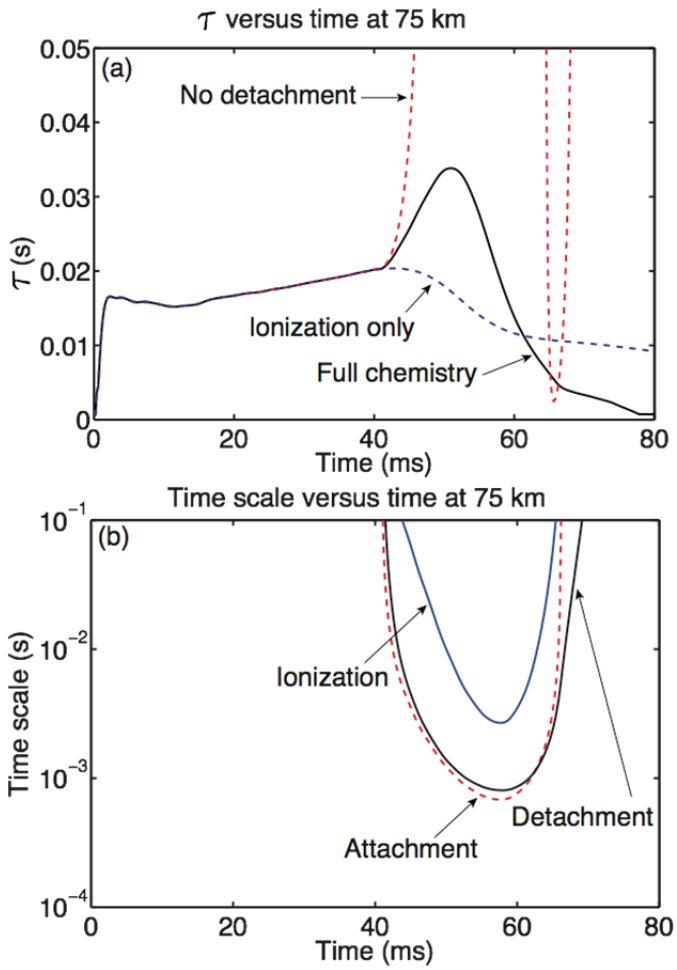

Figure 3: (a) Dielectric relaxation time at different moments of time at 75 km altitude. (b) Timescales of the ionization, attachment, and detachment processes.

We now compare the time dynamics of the electric field at 75 km altitude as a result of different combinations of attachment, detachment, and ionization processes. At 75 km altitude, the breakdown field is approximately 95.4 V/m. As shown in Figure 4, when taking into account only ionization processes in our simulation, the electric field reaches its peak value of ~55 V/m at ~53 ms and then decreases gradually. In the case of including both ionization and attachment processes, the electric field increases rapidly between 45 and 65 ms, and exceeds the breakdown field at ~58 ms. In this case, the electric field reaches a maximum value of ~114 V/m at ~65 ms, and is above the breakdown field from ~58 to 66 ms. This effect is a direct result of electron density and conductivity reduction due to attachment (Figure 2) and therefore significant lengthening of the dielectric relaxation time (Figure 3). With all ionization, attachment, and detachment processes (i.e., full chemistry), the peak value of the electric field is ~69 V/m at

~57 ms but cannot exceed the breakdown field, and the electric field decreases more rapidly than that in the case of ionization only between ~59 and 80 ms.

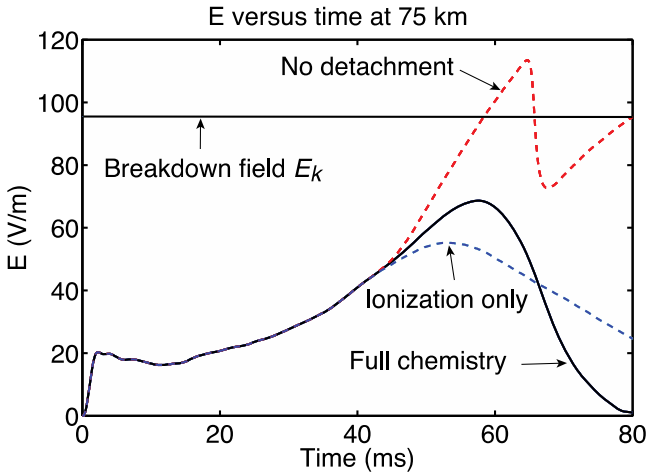

Figure 4: Temporal variation of the electric field at 75 km altitude as a result of different combinations of attachment, detachment, and ionization processes.

DISCUSSION

Inception Mechanism of Short-delayed Sprites and its Implication on the Initiation of Long-delayed Sprites

Qin et al. [2011] studied the inception mechanism of short-delayed sprites. It was found that an intense +CG associated with a large charge moment change induces strong quasi-static electric fields in the upper atmosphere that lead to large-scale diffuse optical emissions in the lower ionosphere at locations where perturbations in the ambient electron density are weak. The same fields can lead to streamer discharges in regions where strong electron density inhomogeneities are present in the ambient ionosphere [*Qin et al.*, 2011]. Since streamers are narrow filamentary plasmas driven mainly by their own space charge field in the streamer head [e.g., *Raizer*, 1991, p. 327], to initiate a sprite streamer, the local space charge field in a compact region with a size of ~10 m at ~75 km needs to increase significantly to be comparable to the breakdown field E_k. This process requires: (1) a strong lightning-induced electric field with its persistence longer than the time required for streamer initiation in the lower ionosphere; (2) an electron density inhomogeneity from which a strong local space charge field can develop [*Qin et al.*, 2011].

Based on the above analysis of the inception mechanism of short-delayed sprites, we see that the roles of ionization, attachment, and detachment processes on the initiation of long-delayed sprites can be investigated by analyzing their effects on (1) the relaxation of the large-scale lightning-induced electric field during long time periods; and (2) the possible creation of electron density inhomogeneities.

The Effect of Ionization on the Dielectric Relaxation Time

The processes of ionization create free electrons via Reactions (1a) and (1b). These processes increase the electron density over time (see the curve labeled "ionization only" in Figure 2). Since ionization is the only process considered in this case, the electron density enhancements are strictly positive over time. This leads to a decrease in dielectric relaxation time τ after 44 ms (see Figure 3). Note that the effects of ionization processes are twofold. On one hand, ionization processes create free electrons in a large-scale region (i.e., in a halo region), which enhances the conductivity and reduces the relaxation time of the lightning-induced electric field. On the other hand, ionization processes that occur in a localized region are critical for streamer initiation since they are the processes that produce large amounts of free electrons to create a strong local space charge field. So far we only discuss the effect of ionization processes on the relaxation of the lightning-induced electric field. Apparently, ionization processes in a large-scale region (i.e., ionization processes that produce the sprite halo) are unfavorable for sprite streamer initiation, since they enhance the conductivity and thus lead to shorter dielectric relaxation time, and therefore shorter persistence of the electric field.

The Effect of Attachment on the Dielectric Relaxation Time

Based on the discussion in the above section, it appears that the attachment process is favorable for streamer initiation, since it removes free electrons from the upper atmosphere via Reaction (2) and therefore leads to longer persistence of the lightning-induced electric field, as has been emphasized by *Qin et al*. [2011]. By taking into account the attachment process, the electron density drops ~5 orders of magnitude between 42 and 58 ms (see Figure 2). Consequently, dielectric relaxation time τ increases drastically causing the electric field to exceed the breakdown field of 95.4 V/m at ~58 ms, suggesting that in this scenario, the attachment process enhances the electric field significantly. Once $E > E_k$, the process of ionization dominates, and the electron density responds with a sharp peak at 66 ms, causing relaxation time τ and electric field to decrease after that.

The Effect of Detachment on the Dielectric Relaxation Time

The associated detachment process creates free electrons via Reaction (4). The temporal variation of electron density in the full chemistry case shown in Figure 2 demonstrates the role of detachment over the 80 ms period. Between 43 and 51 ms, the electron density drops slightly, suggesting that attachment removes electrons at a dominant rate. However, these losses are much less dramatic with detachment than without detachment, and hence the resulting increase of τ is much smaller, causing the peak electric field to be below the breakdown field. Note that *Liu* [2012] also found that the detachment processes can significantly weaken the effect of electron depletion by attachment processes. These results

emphasize that the detachment process serves to diminish the effect of the attachment process in lowering the conductivity and therefore is unfavorable for sustaining high electric fields and maximizing sprite initiation potential.

Breakdown Field as a Function of n_{O^-}/n_e

As discussed in the section above, the detachment process is unfavorable for the persistence of the mesospheric lightning-induced electric field. This leads to less favorable conditions for streamer initiation. On the other hand, in a localized region where a sprite streamer initiates, the detachment process serves as a mechanism to lower the electric field required to produce a net increase of free electrons.

In light of the importance of the detachment process suggested by *Luque and Gordillo-Vázquez* [2011], an amendment of the breakdown field definition follows from simple analysis. Presently, the definition of E_k is produced by the equality of attachment and ionization frequencies [*Raizer*, 1991, p.135]. This definition only takes into account Reactions (1) and (2), which create or remove free electrons. Since the detachment process (4) also releases free electrons, we incorporate this process in the definition of electric breakdown field by defining E_k as:

$$\nu_{ion}(E_k/N) + \frac{n_{o^-}}{n_e}\nu_{detach}(E_k/N) = \nu_{attach}(E_k/N) \tag{11}$$

This definition suggests that the breakdown field E_k is not only a function of the air density N, but also a function of the ratio n_{O^-}/n_e as seen in Figure 5. It is important to note that on the short-delay sprite time scales, the role of detachment is negligible [*Liu*, 2012], and the original E_k definition holds.

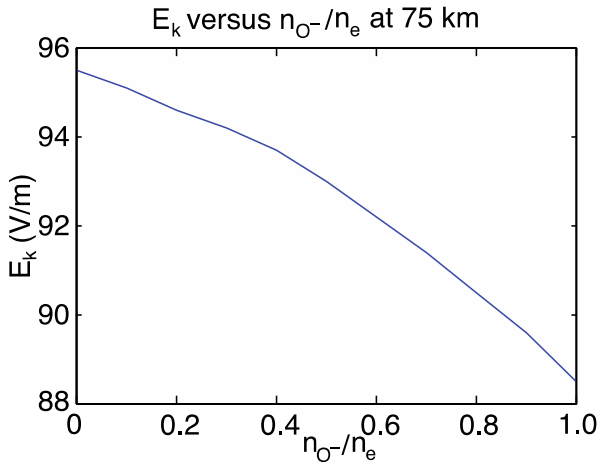

Figure 5: The breakdown field E_k at 75 km altitude as a function of n_{O^-}/n_e.

As we can see in Figure 5, the increase of the ratio n_{O^-}/n_e from 0 to 1 lowers the breakdown field by ~7.33%. This effect is not significant when compared to the lowering of the lightning-induced electric field by ~39.47% when comparing the combined ionization-attachment and full chemistry processes (see Figure 4). Therefore, we conclude that the detachment process is unfavorable for the initiation of long-delayed sprites.

CONCLUSIONS

By analyzing their effects on the relaxation of the large-scale lightning-induced electric fields and on the lowering of the breakdown field E_k, we successfully classified the roles of ionization, detachment, and attachment reactions in the process of long-delay sprite initiation. By decreasing the dielectric relaxation time, ionization and detachment processes decrease the magnitude of the lightning-induced electric field, deeming them unfavorable in sprite initiation. It is the attachment process that plays a major role in increasing the dielectric relaxation time, hence sustaining the external electric field. As a mean to reach the essential electric field required for long-delay sprite inception, the lightning continuing current providing the necessary charge moment changes is to be considered as the primary factor on long time scales.

ACKNOWLEDGMENTS

This material is based upon work supported by the National Science Foundation under Grant No. EEC-1062984.

REFERENCES

Bell, T. F., S. C. Reising, and U. S. Inan (1998), Intense continuing currents following positive cloud-to-ground lightning associated with red sprites. *Geophys. Res. Lett., 25*(8), 1285–1288, doi:10.1029/98GL00734.

Cummer, S. A., and M. Füllekrug, (2001), Unusually intense continuing current in lightning produces delayed mesospheric breakdown. *Geophys. Res. Lett., 28*(3), 495–498, doi:10.1029/2000GL012214.

Cummer, S. A., and W. A. Lyons (2005), Implications of lightning charge moment changes for sprite initiation, *J. Geophys. Res., 110*, A04304, doi:10.1029/2004JA010812.

Franz, R. C., R. J. Nemzek, and J. R. Winckler (1990), Television image of a large upward electrical discharge above a thunderstorm system, *Science, 249*, 48–51.

Gamerota, W. R. et al. (2011), Comparison of sprite initiation altitudes between observations and models. J. *Geophys. Res., 116*, A02317.

Hu, W., S. A. Cummer, and W. A. Lyons (2007), Testing sprite initiation theory using lightning measurements and modeled electromagnetic fields. *J. Geophys. Res., 112*, D13115, doi:10.1029/2006JD007939.

Li, J., S. A. Cummer, W. A. Lyons, and T. E. Nelson (2008), Coordinated analysis of delayed sprites with high-speed images and remote electromagnetic fields. *J. Geophys. Res., 113*, D20206, doi:10.1029/2008JD010008.

Liu, N., and V. P. Pasko (2004), Effects of photoionization on propagation and branching of positive and negative streamers in sprites, *J. Geophys. Res., 109*, A04301, doi:10.1029/2003JA010064.

Liu, N.Y. (2012), Multiple ion species fluid modeling of sprite halos and the role of electron detachment of O^- in their dynamics, *J. Geophys. Res., 117*, A03308,

doi:10.1029/2011JA017062.
Luque, A., and F. J. Gordillo-Vázquez, (2011), Mesospheric electric breakdown and delayed sprite ignition caused by electron detachment. *Nature Geosci., 5*, 22, doi:10.1038/NGEO1314.
Lyons, W. A. (1996), Sprite observations above the U.S. High Plains in relation to their parent thunderstorm systems, *J. Geophys. Res., 101(D23), 29*, 641–29,652, doi:10.1029/96JD01866.
Morrow, R., and J. J. Lowke (1997), Streamer propagation in air, *J. Phys. D Appl. Phys., 30*, 614–627.
Pasko, V. P., U. S. Inan, T. F. Bell, and Y. N. Taranenko (1997), Sprites produced by quasi-electrostatic heating and ionization in the lower ionosphere. *J. Geophys. Res., 102*(A3), 4529–4561, doi:10.1029/96JA03528.
Pasko, V. P., U. S. Inan, and T. F. Bell (1998), Spatial structure of sprites, *Geophys. Res. Lett., 25*, 2123–2126, doi:10.1029/98GL01242.
Qin, J., S. Celestin, and V. P. Pasko (2011), On the inception of streamers from sprite halo events produced by lightning discharges with positive and negative polarity, *J. Geophys. Res., 116*, A06305, doi:10.1029/2010JA016366.
Qin, J., S. Celestin, and V. P. Pasko (2012), Formation of single and double-headed streamers in sprite-halo events, *Geophys. Res. Lett., 39*, L05810, doi:10.1029/2012GL051088.
Raizer, Y. P. (1991), *Gas Discharge Physics*, Springer, New York.
Sentman, D. D., E. M. Wescott, D. L. Osborne, D. L. Hampton, and M. J. Heavner (1995), Preliminary results from the Sprites94 Aircraft Campaign: 1. Red sprites, *Geophys. Res. Lett., 22*(10), 1205–1208, doi:10.1029/95GL00583.
Stanley, M., P. Krehbiel, M. Brook, C. Moore, W. Rison, and B. Abrahams (1999), High speed video of initial sprite development, *Geophys. Res. Lett., 26*(20), 3201–3204, doi:10.1029/1999GL010673.

CORONA MODELING FOR LIGHTNING PROTECTION APPLICATIONS

Joe Tucker* and Victor Pasko[#]

Department of Electrical Engineering
The Pennsylvania State University, University Park, PA 16802

*Undergraduate Student of Department of Electrical Engineering
The Pennsylvania State University
State College, Pennsylvania 16802

ABSTRACT

This paper discusses a numerical model that allows the study of the initiation and development of electrical corona discharges that occur near the tip of a lightning rod. The corona influences the formation of leaders and thus lightning attachment as discussed in [*Bazelyan et al.* 2008]. The model closely follows the approaches developed by *Aleksandrov et al.* [2002] and *Kowalski* [2008], and we first conduct a thorough comparison of our model results with results obtained in the previous studies. We then provide a discussion and comparison of the model results with the analytical theory of corona in spherical geometry summarized recently by *Bazelyan et al.* [2008]. The model proves to be a viable method to simulate the formation of development of a corona near the tip of a lightning rod.

INTRODUCTION

This paper focuses on one specific type of lightning known as cloud-to-ground (CG) lightning. In cloud to ground lightning, the charge accumulation in the thundercloud results in the initiation and propagation of a downward leader. The ground acts a neutral charge reservoir and pulls the leader down due to the difference in electric potential. The approach of the downward leader changes the ambient electric field near the ground. This change in electric conditions results in the formation of a second leader of opposite polarity. This new leader travels upward toward the downward leader until the two meet. Upon contact the two leaders form a conducting channel between the ground and charge layer in the cloud resulting in a lightning flash. This paper focuses solely on the processes and conditions involved in the formation of the upward leader.

[#] Faculty Mentor

Upward leaders tend to form at discontinuities in the ground, such as towers and tall buildings. The model developed in this paper simulates the processes that occur around a "sharp tipped" object such as a lightning rod. The ambient electric fields that occur during a thunderstorm can cause ionization at the tip of the object resulting in the formation of a corona around the tip of the object. This corona significantly influences the electric field conditions around the object. Since the electric field around the tip of the object causes the formation of an upward leader this corona is a vital aspect of modeling of lightning attachment to a lightning rod.

The corona around the tip of a sharp object falls into three distinct categories: glow corona, streamer corona, and leaders [*Aleksandrov et al.,* 2002]. Glow corona occurs when the electric field at the outer surface of the object exceeds the breakdown field for air at ground pressure. Air molecules are ionized at the outer surface of the object resulting in ions leaking out from object along the electric field lines. This ion distribution reduces the electric field near the object and maintains breakdown field magnitude at the outer surface of the object. If the electric field around the object continues to rise, it can eventually support ionization outside of the object in the form of streamer discharges as described by the Meek Condition [*Meek and Craggs,* 1978]. This causes the formation of multiple streamers around the object. Streamers are filamentary plasma discharges near the tip of the object. Many streamers form a streamer corona, which tends to maintain a constant electric field in the region of space through which it propagates. These streamers will eventually act to significantly increase air temperature and form a self-propagating leader that moves upward and facilitates lightning attachment. The model developed in this paper models all three of these regimes around the object as the corona develops.

MODEL DESCRIPTION

The model approximates the lightning rod geometry as a conducting sphere in a spherically isotropic region. The potential on the sphere drives the simulation. Since the lightning rod is a conductor it maintains an equipotential with the ground. Assuming a constant ambient electric field between the ground and the top of the object the potential difference between the sphere and ambient potential is simply the ambient electric field multiplied by the height of the rod [*Aleksandrov et al.,* 2005b; *Kowalski,* 2008]. Since the height of the rod is constant, any rise in the ambient electric field is directly proportional to the rise in potential on the sphere. With the potential defined on the sphere, the model assumes a second remote spherical shell that shares a center with the spherical electrode. This second sphere is assumed to be at zero potential. These two potentials define the boundary conditions of the system. Given any charge distribution between the two boundaries the model can calculate the potential at all points between the two boundaries. The model geometry and simulation domain used in the present studies are illustrated in Figure 1.

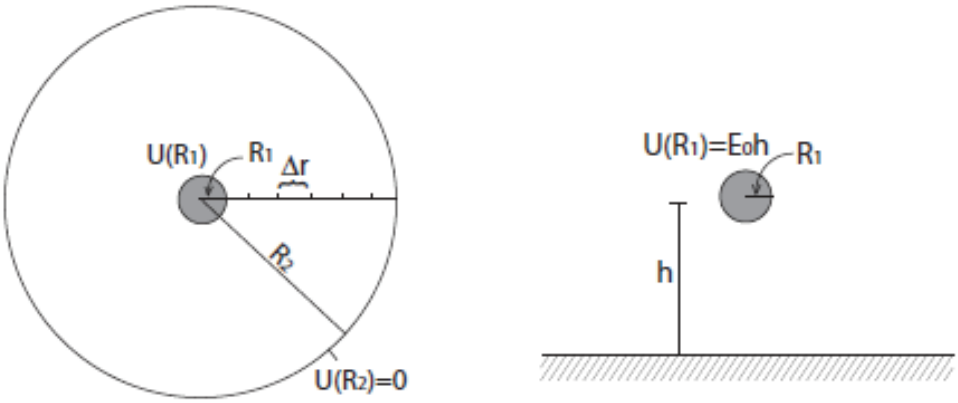

Figure 1: Spherical geometry used in the model. $U(R_1)$ is the potential on the inner electrode, E_0 is the uniform vertical ambient electric field, h is the height of the rod, R_1 and R_2 are the radii of the inner electrode and remote outer shell respectively, and Δr is the step between grid points in the one-dimensional simulation domain [*Kowalski*, 2008].

The simulation begins with a zero potential on the object and no charge between the two spheres. The potential on the inner sphere rises linearly with a slope specified by the investigator. When the potential on the inner sphere reaches the potential corresponding to the breakdown field for air the glow corona forms. At that time of initiation, the model must decide how much charge to inject into the corona to maintain a self-consistent solution for the electric field. The model accomplishes this through guess and check using a simple binary search algorithm [*Roberts,* 1995]. Each guess of charge to inject is used to calculate the resultant charge distribution between the spheres using the injected charge and all previously injected charge. From this charge distribution the model derives the electric field in the system using a Thomas Algorithm [*Hockney and Eastwood,* 1988, p. 185] approach to solve Poisson's Equation at each grid point. The iterations continue until the resultant electric field on the inner sphere is within some tolerance of the breakdown field. This model approach is identical to the one developed originally by *Aleksandrov et al.* [2002] and *Kowalski* [2008].

Once the amount of injected charge is found within the tolerance, the model completes its cycle and steps to the next time instant. As the model moves through these cycles, the corona develops. In order to check for streamer initiation, after the model finds the injected charge and calculates the resultant electric field it uses that electric field to find the ionization and attachment frequencies as well as the mobility of the electrons in the system. These four quantities define the electric field dependent ionization coefficient:

$$\alpha(E) = \frac{\nu_i(E) - \nu_a(E)}{|E||\mu|} \tag{1}$$

where ν_i is the ionization frequency, ν_a is the two-body attachment frequency, μ_e is the electron mobility, and E is the electric field. The electric field dependent quantities ν_i, ν_a, and μ_e are found using the approach described in [*Morrow and Lowke*, 1997]. The Meek Condition states that if

$$\int_{R_1}^{R_2} \alpha(E) dr > 18 \tag{2}$$

streamers will form, where R_1 is the radius of the electrode and R_2 is the radius of the remote outer sphere [*Meek and Craggs,* 1978; *Kowalski,* 2008]. The length of the streamer region is defined by the potential difference between the inner and outer spheres and known phenomenology of streamer corona which establishes a quasi-constant electric field at a value of E_{cr}^{+} = 4.5 kV/cm [e.g., *Pasko et al.,* 2000, and references therein]. The model determines the length of the streamer zone by incrementing the length and calculating the electric field in the system. Once the potential drop across the system is equal to the potential difference defined by the driving potential function the model uses that streamer zone length.

The model continues calculating after streamer initiation but must test to see if the electric field at the inner sphere reaches the breakdown field. If the electric field is below breakdown the simulation propagates the previously injected ions but does not inject any new charge into the system. Once the electric field rises above the breakdown field the model begins injecting glow corona current into the system and the process repeats. In order for a leader to form, the potential drop across the streamer zone must be greater than 400 kV [*Aleksandrov et al.,* 2005a]. Once this occurs, an upward leader has formed and the model ceases operation.

In the following section we test the model described above by (1) comparing our model results with the previous publications of *Aleksandrov et al.* [2005b] and *Kowalski* [2008]; (2) verifying an analytical result: immediately after the formation of streamer corona, half of the potential drop across the system occurs in the corona and half occurs in free space ahead of the streamers; (3) comparing the model results with the analytical theory of glow corona [*Bazelyan et al.,* 2008].

MODEL RESULTS AND DISCUSSION

Comparison with Previous Model Results

First the model was tested against results obtained by *Aleksandrov et al.* [2005b] and *Kowalski* [2008]. For those comparisons we assume a radius of the inner electrode R_1 = 1 cm, outer electrode R_2 = 5 m and consider an applied voltage in the form:

$$U(t) = \begin{cases} U_{\max} \dfrac{t}{\tau}, & t < \tau \\ U_{\max}, & t > \tau \end{cases} \tag{3}$$

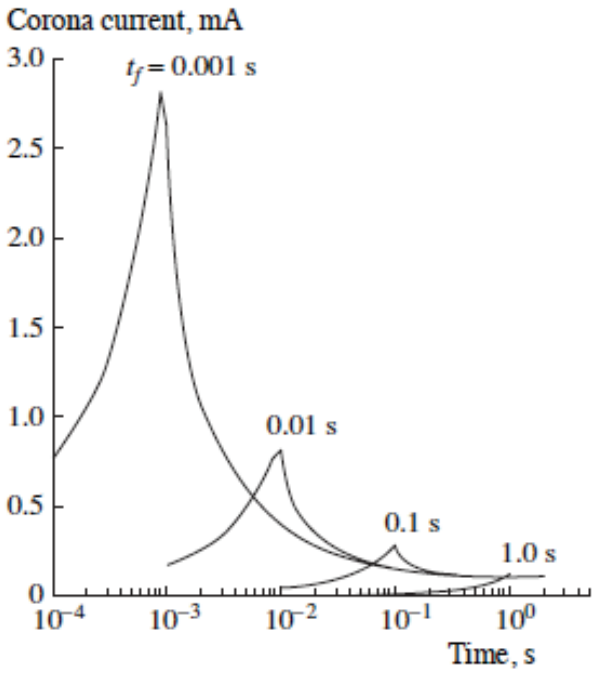

(a)

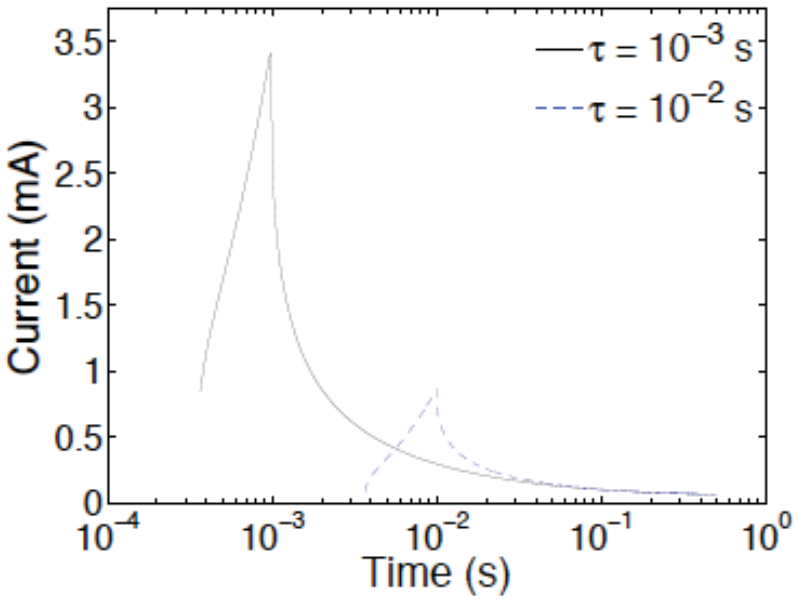

(b)

Figure 2: (a) Corona current from model developed by *Aleksandrov et al.* [2005b]. (b) Corona current from model developed by *Kowalski* [2008].

where U_{max} = 300 kV and the rise time τ takes two values, 10^{-2} and 10^{-3} seconds. Measurements of the corona current over the course of the simulation for different rise times (τ) provided a measure of comparison between the models. Figure 2 results are obtained by the two aforementioned works. The developed model found similar results to both *Aleksandrov et al.* [2005b] and *Kowalski* [2008]. These results are documented in Figure 3.

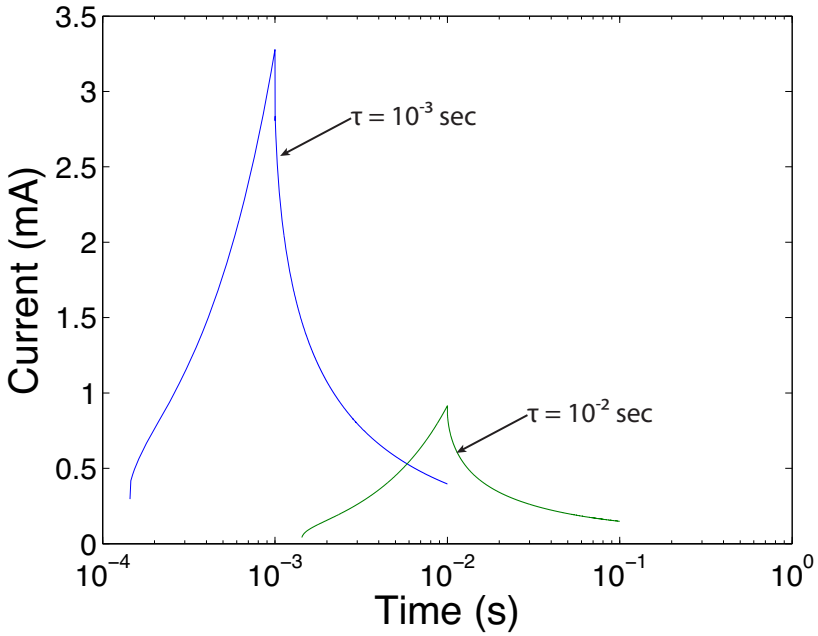

Figure 3: Semilogrithmic plot of the simulated corona current for two different rise times obtained in current work.

Voltage Drops after Formation of Streamer Corona

As stated in the model description, a leader forms when the potential drop across the streamer region is greater than 400 kV. It is simple to show analytically that the potential drop across the streamer region is equal to the potential drop across the free space region. As previously discussed the streamer corona creates a quasi-constant electric field (E_{cr}^{+} = 4.5 kV/cm) in the space through which it propagates. In the free space in front of the streamer corona the electric field falls off as the square of the radius. The electric field is thus defined by

$$E(r) = \begin{cases} E_{\mathrm{cr}}{}^{+} & r < R_{\mathrm{cor}} \\ \frac{C}{r^2} & r > R_{\mathrm{cor}} \end{cases} \tag{4a}$$

where R_{cor} is the radius of the streamer corona. Setting these two equal to each other at $r = R_{cor}$ allows one to find $C = (E_{cr}^{+})\, R_{cor}^{2}$. Having integrated the electric field in space from R_1 to R_2 and assuming V to be the applied potential to the inner electrode we get:

$$V = E_{cr}^{+}[R_{cor} - R_1] + E_{cr}^{+} R_{cor}\left[1 - {}^{R_{cor}}/_{R_2}\right], \tag{4b}$$

where the first term represents the voltage drop across the corona and the second term represents the voltage drop across the free space region. Taking the ratio of the corona voltage drop over the free space voltage drop yields:

$$\text{Ratio} = \frac{1 - {}^{R_1}/_{R_{cor}}}{1 - {}^{R_{cor}}/_{R_2}}. \tag{4c}$$

When R_1 is very small compared to R_{cor} and R_2 is very large compared to R_{cor} this ratio goes to one. Since R_2 in the model is taken to be at infinity, this is always the case. Thus the potential drop across the streamer region is one half of the drop across the system. Since the drop must be greater than 400 kV to initiate a leader, an equivalent condition for leader is the potential across the system must be greater than 800 kV. In order to verify this condition in the framework of the numerical model, the ratio of the potential drop in the corona to the free space drop was plotted during a representative model run illustrated by Figure 4.

For the simulation shown in Figure 4 the radius of the inner electrode was R_1 = 1 cm and the radius of the outer electrode was R_2 = 5 m. The applied voltage represented a uniform linear rise in the form:

$$U(t) = U_0 \frac{t}{\tau}, \tag{5}$$

where U_0 = 300 kV and $\tau = 3 \times 10^{-4}$ seconds. These parameters were chosen to illustrate several streamer flashes. As can be seen the ratio drops to around one at each streamer flash.

One notes that the plotted ratio significantly deviates from unity as the simulation progresses. The simulation ends when a leader forms, i.e., the voltage drop across the streamer zone is greater than 400 kV. This corresponds to a streamer length of about R_{cor} = 1 m. In this simulation the radius of the outer shell was taken to be R_2 = 5 m. This deviation is a result of the length of the streamer discharge zone increasing to a length at which it is comparable to the outer shell radius R_2. Figure 4(b) illustrates a case when R_2 = 10 m As can be seen by comparing Figures 4(a) and 4(b) the deviation decreases drastically when the radius of the outer electrode increases from R_2 = 5 m to R_2 = 10 m.

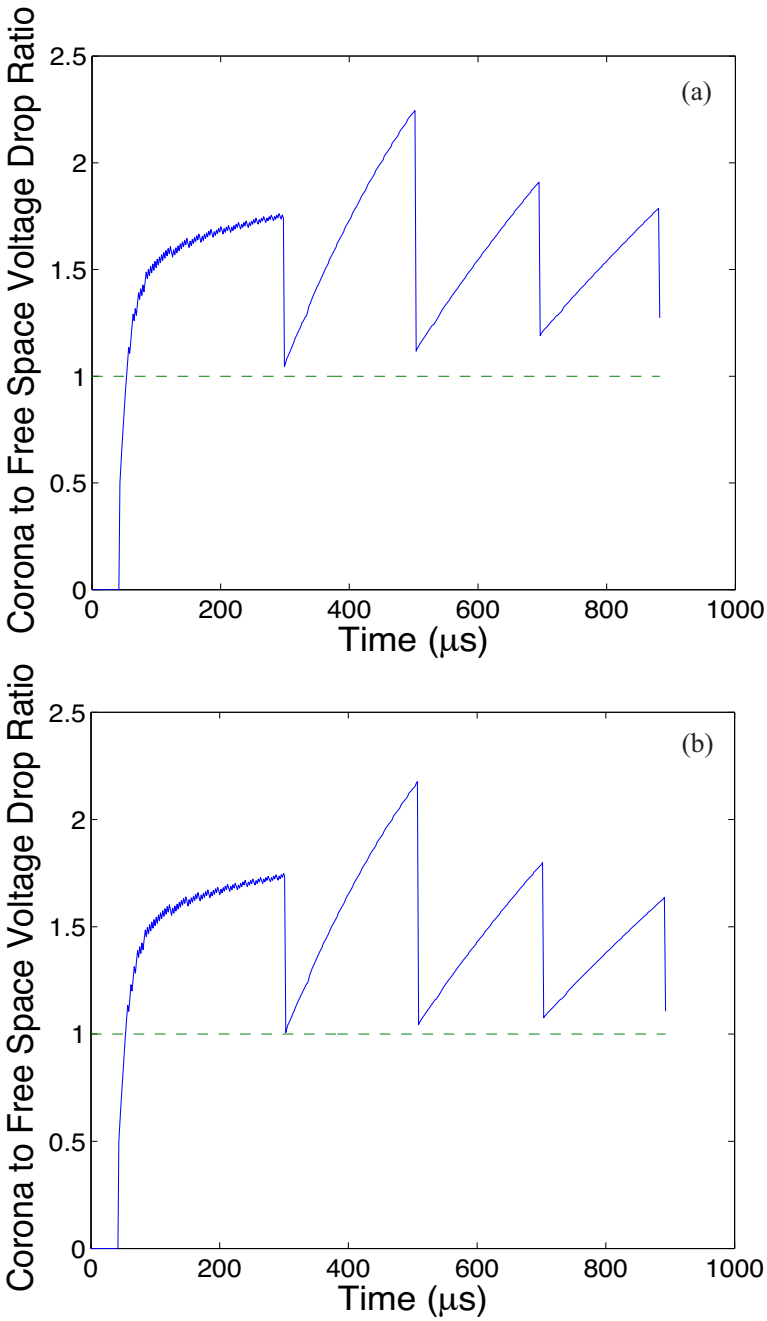

Figure 4: Ratio of the voltage drop across the corona to the voltage drop across the free space region for (a) R_2 = 5 m and (b) R_2 = 10 m.

Comparison with Analytical Corona Models

For the third test of the model, the simulated results were compared to analytical derivations for the current and corona radius found in [*Bazelyan et al.*, 2008]. For these comparisons the applied voltage function is again defined by equation (3) with U_{max} = 100 kV and rise time $\tau = 10^{-4}$ seconds. These parameters

were chosen to ensure the discharge would consist only of a glow corona. Equations (6)–(9) below summarize the analytical theory developed by *Bazelyan et al.* [2008]. *Bazelyan et al.* [2008] also used a one-dimensional spherical geometry for their derivations. *Bazelyan et al.* [2008] define corona radius R and corona current i for $t < \tau$ as:

$$R = \sqrt{\frac{\mu_i U_{\max}}{3\tau}}\, t \tag{6}$$

$$i = 2\pi\varepsilon_0 \sqrt{\frac{\mu_i {U_{\max}}^3}{3\tau^3}}\, t \tag{7}$$

and for $t > \tau$ as:

$$R = \sqrt{\frac{2}{3}\mu_i U_{\max}\left(t - \frac{\tau}{2}\right)} \tag{8}$$

$$i = \pi\varepsilon_0 \sqrt{\frac{2\mu_i {U_{\max}}^3}{3\left(t-\frac{\tau}{2}\right)}}, \tag{9}$$

where $\mu_i = 1.5 \times 10^{-4}$ m^2/V·s [*Kowalski*, 2008] is the mobility of ions at ground air pressure and $\varepsilon_0 = 8.85 \times 10^{-12}$ F/m is the permittivity of free space.

Figures 5 and 6 illustrate the similarities between the shapes of *Bazelyan et al.* [2008] analytical derivations and the simulated results for both current and corona radius, respectively. As the corona continues to develop the model results and analytical results converge. In the calculations of *Bazelyan et al.* [2008], they place two constraints on the parameters of the system. The first is that the radius of the outer electrode is at infinity; a constraint the model can easily accommodate. The second is that the inner radius is zero. This constraint is not easily integrated into the model resulting in the observed differences in Figure 5 and Figure 6 between the analytical and numerical model results. In this context we note that we observe a better agreement between results of the two models for a smaller inner radius as illustrated by Figures 5(b) and 6(b). Figure 5 illustrates that the simulated corona current follows the growth and decay of the current as predicted by the analytical theory. Figure 6 illustrates the growth and propagation of the corona radius as predicted by the analytical theory, particularly agreeing with $R \sim \sqrt{t}$ scaling predicted by the analytical theory.

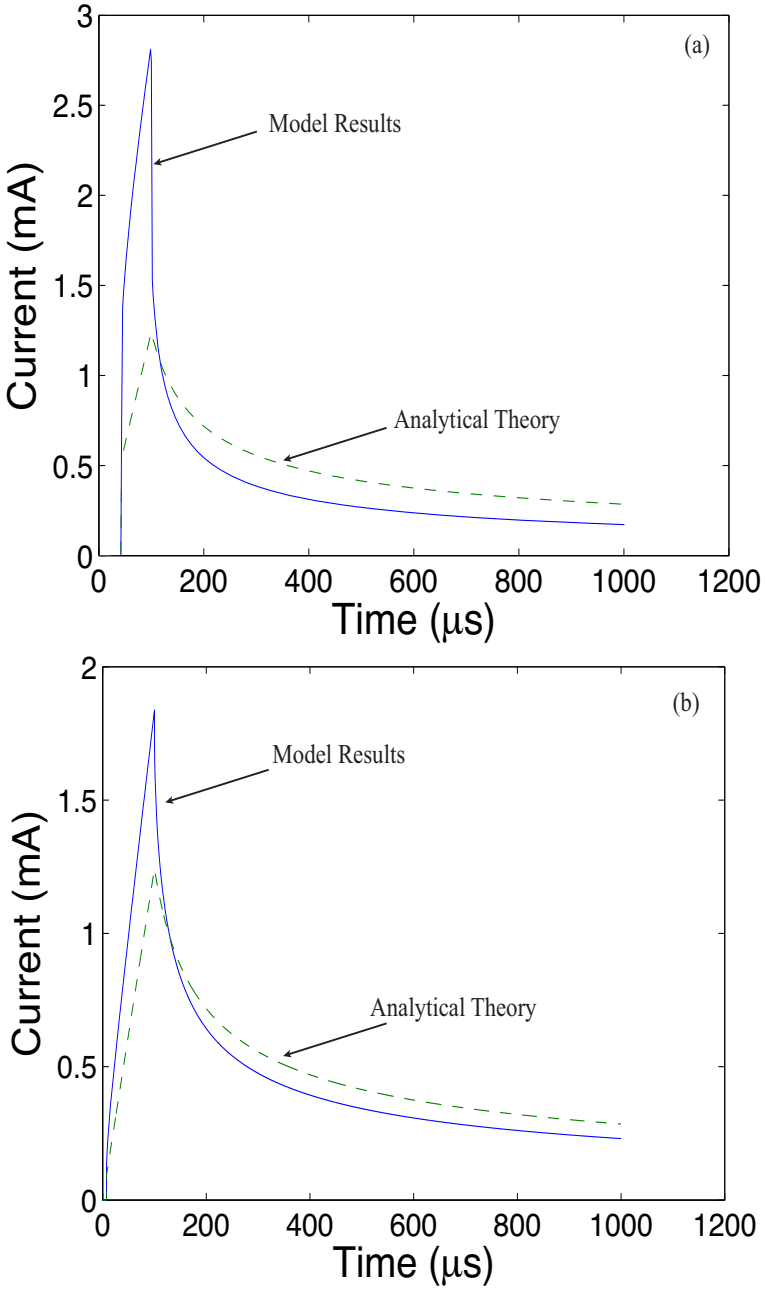

Figure 5: Comparisons between the model results and analytical theory of *Bazelyan et al.* [2008]. The radii of the inner electrode are (a) R_1 = 1 cm and (b) R_1 = 1 mm.

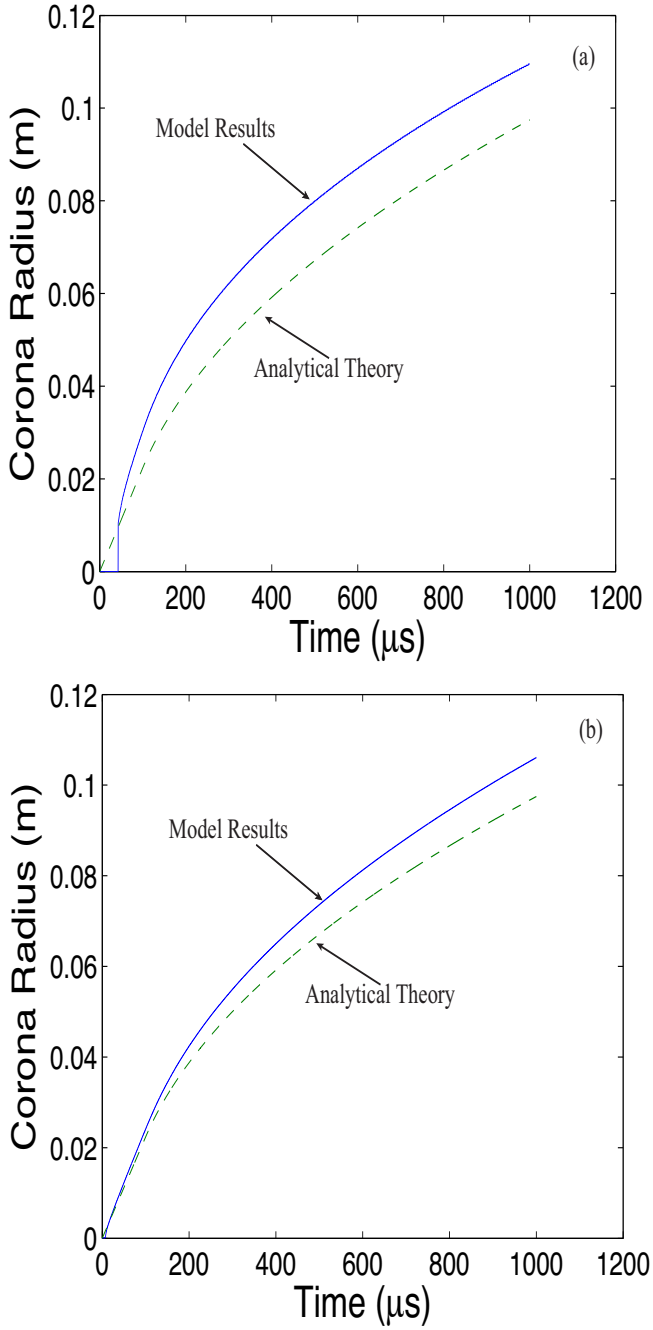

Figure 6: Comparisons between the model results and analytical theory of *Bazelyan et al.* [2008]. The radii of the inner electrode are (a) R_1 = 1 cm and (b) R_1 = 1 mm.

CONCLUSIONS

The model developed for this paper simulates the development of the corona around a lightning rod. The results from the model adhered to established results from other models, specifically those described in [*Aleksandrov et al.*, 2005b; *Kowalski*, 2008]. The model results are compared with the analytical corona model published in [*Bazelyan et al.*, 2008]. These comparisons have shown that the model performs well in simulating the corona discharges that occur near the tip of a lightning rod. The model shows convergence to analytical theory as is illustrated by Figures 5 and 6. The convergence of the model to analytical theory when the radius of the inner electrode is small adheres directly to the restriction set forth in [*Bazelyan et al.*, 2008]. Figure 4 shows the model converging to a separate analytical result, an equal drop in potential across the streamer discharge region and free space region of the system immediately after a streamer corona discharge. The model adheres to analytical theory in both the glow corona and streamer corona regimes. The model has proven to be an effective simulation of the corona discharge near a sharp tipped lightning rod.

ACKNOWLEDGMENTS

This material is based upon work supported by the National Science Foundation under grants No EEC-1062984 and AGS-0652148 to Penn State University.

REFERENCES

Aleksandrov, N. L., E. M. Bazelyan, M. M. Drabkin, R. B. Carpenter, and Y. P. Raizer (2002), Corona discharge at the tip of a tall object in the electric field of a thundercloud, *Plasma Phys. Rep., 28*(11), 953-964.

Aleksandrov, N. L., E. M. Bazelyan, F. D'Alessandro, and Y. P. Raizer (2005a), Dependence of lightning rod efficacy on its geometric dimensions-a computer simulation, *J. Phys. D: Appl. Phys., 38*(1), 1225-1238.

Aleksandrov, N. L., E. M. Bazelyan, and Y. P. Raizer (2005b), The effect of a corona discharge on a lightning attachment, *Plasma Phys. Rep., 31*(1), 75-91.

Bazelyan, E. M., Y. P. Raizer, and N. L. Aleksandrov (2008), Corona initiated from grounded objects under thunderstorm conditions and its influence on lightning attachment, *Plasma Sources Sci. Tech.,* 17,024015.

Hockney, R. W., and J. W. Eastwood (1988), *Computer Simulation Using Particle*, Taylor & Francis Group, New York, NY.

Kowalski, E. J. (2008), Efficient corona models in spherical geometry for lightning protection applications, Honors Thesis. Pa. State Univ., University Park.

Meek, J. M., and J. D. Craggs (1978), *Electrical Breakdown of Gases,* John Wiley and Sons, New York, NY.

Morrow, R., and J. J. Lowke (1997), Streamer propagation in air, *J. Phys. D: Appl. Phys., 30,* 614-627.

Pasko, V. P., U. S. Inan, and T. F. Bell (2000), Fractal structure of sprites, *Geophys. Res. Lett.*, 27, 497-500.

Roberts, E. S. (1995), *The Art and Science of C,* Addison-Wesley Publishing Company, Inc.

ON THE ROLE OF NEUTRAL TURBULENCE ON THE EVOLUTION OF SPECULAR METEOR ECHOES: STATISTICS

Carlos A. Mulero Hernandez,* Julio V. Urbina,[#] Freddy Galindo[+]

Department of Electrical Engineering
The Pennsylvania State University, University Park, PA 16802

*Undergraduate Student of
Department of Electrical & Computer Engineering
University of Puerto Rico Mayagüez
Mayagüez, PR 00681-9000

ABSTRACT

A second type of signal decay has recently been observed in underdense meteor echoes. These events show a slow decay in their signal strength during their initial milliseconds of detection and an abrupt signal amplitude decay later on. These characteristics are related to the temporal evolution of underdense specular meteor trails immersed in a background neutral atmosphere. This paper seeks to establish statistical measurements for this new type of specular underdense meteors displaying a double decay. The data presented in this paper was recorded using the Jicamarca All-sky Specular MEteor Radar (JASMET) system located at the Jicamarca Radio Observatory (JRO), in Lima, Peru. We compare these two types of specular meteor echoes and present their statistical distribution such as height, occurrence during the day, and other parameters.

INTRODUCTION

When meteors enter the Earth's atmosphere they produce a plasma trail from which radio waves may reflect. The amplitude of the radar signal received at the ground shows a rapid increase as the trail forms but then decays exponentially in time. It is generally true that ambipolar diffusion is the dominant factor in the early stages of trail growth, and therefore, primarily determines the echo intensity for underdense trails near mesopause heights. The trail decays in an exponential manner due to ambipolar diffusion which can be modeled with this relationship:

[#] Faculty Mentor
[+] Graduate Mentor

$$A(t) = A_0 e^{-(16\pi^2 D_a t/\lambda^2)} = A_0 e^{-ln2\frac{t}{\tau_{1/2}}} \quad (1)$$

where λ is the radar wavelength, D_a is the ambipolar diffusion coefficient and t is time. $A(t)$ is the radio amplitude at time t and A_0 is the amplitude value at $t = 0$, which is the time when the exponential decay begins. $\tau_{1/2}$ is the time that the amplitude takes to fall to one half of its maximum value [1][2].

Meteoroids have many important consequences in the study of space environments and the Earth's upper atmosphere. The meteoroids damage spacecraft, deposit material in the lower thermosphere and upper mesosphere. They also can create layers of charged materials, which radars and ionosondes can detect. Meteors can also modify the background plasma density and conductivity of the lower ionosphere and deposit plasma columns which can be used to monitor atmospheric conditions in the lower thermosphere and enable meteor burst communication [3]. From Equation (1) it is possible to estimate the parameter D_a which is proportional to atmospheric temperature, pressure and composition by this equation:

$$D_a = K_{amb}\frac{T^2}{P} \quad (2)$$

where T is the temperature and P is pressure[2]. More details on the parameter K_{amb} can be seen in [1].

A second type of signal decay has recently been observed in underdense meteor echoes. These events show a slow decay in their signal strength during their initial milliseconds of detection and an abrupt signal amplitude decay later on. These characteristics are related to the temporal evolution of underdense specular meteor trails immersed in a background neutral atmosphere. This behavior which deviates from the common exponential decay diverges considerably from the behavior described in Equation (1) and could cause a large error when using Equation (2) to estimate atmospheric parameters.

This paper seeks to establish statistical measurements for the population of this new kind of specular underdense meteors displaying a double decay. The data for this experiment was recorded using the Jicamarca All-sky Specular MEteor Radar (JASMET) system located at the Jicamarca Radio Observatory (JRO) in Lima, Peru. The occurrence of these double-decay specular meteors will be compared with the occurrence of the normal specular meteors. The heights at which both, normal decay and double-decay specular meteors, occur will be examined to determine any correlation to their height. Furthermore, the occurrence for both types of specular decay will be examined across time to observe any patterns that develop from temporal variations and the distributions of the received powers are also examined.

EXPERIMENT DESCRIPTION

The data for this experiment were recorded using the JASMET system located at the JRO in Lima, Peru on November 26, 2011 [4]. The data from JASMET were processed to narrow down the number of possible events that would have to be manually classified. The first filtering consisted in calculating the noise for 0.5-second blocks of data and then discarding any data points whose value was less than this noise plus 3dB. Any values higher than this are still considered potential events at this point. A second filter looked at the number of values left in each 0.5-second block after the first filtering. If it was less than three then it would not be possible to identify what kind of event that block contains because there would be too few points to see a specular event. If 0.5-second blocks of time didn't have more than 3 data points in them, they were discarded. A third filter then determined if the points found in the 0.5-second block after the first filtering phase were too far apart from each other. Any blocks that would only contain 3 data points connected to each other in the final plot were also excluded from the manual selection process as the plot resulting from them would have had too few data points joined to see a specular event.

After the automated filtering process, each 0.5 second block was plotted. These plots were used to visually identify, classify and quantify the different specular events recorded in the data. Only the events that decayed as the two shown in Figure 1 were of interest. Henceforth, in this paper, we will label the normal specular decay as type A and the new kind of specular decay will be labeled as type B.

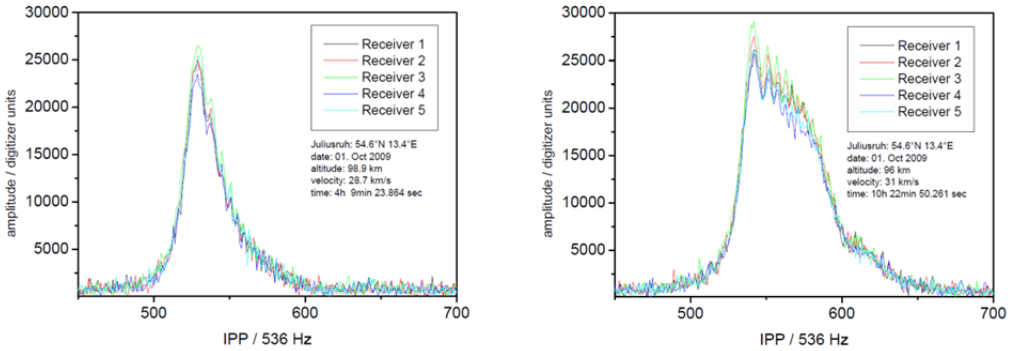

Figure 1: On the left a normal specular event, type A. On the right a specular event with the new kind of signal decay, type B. Recorded on Oct 1, 2009 at Juliusruh, Germany.

EXPERIMENT RESULTS

After they had been classified as type A, normal specular signal decay, or type B, the new signal decay of interest, three parameters were extracted from the groups of events: The heights at which they occur, the times of the day at which they happen and the power received at the radar. The heights in Figure 2 were determined using an implementation of the technique presented in [5] for angle of

arrival estimation and multiplying the cosine of this angle with the range of the event being analyzed. Table 1 summarizes some added information that can be extracted from the plots in Figures 2 to 4.

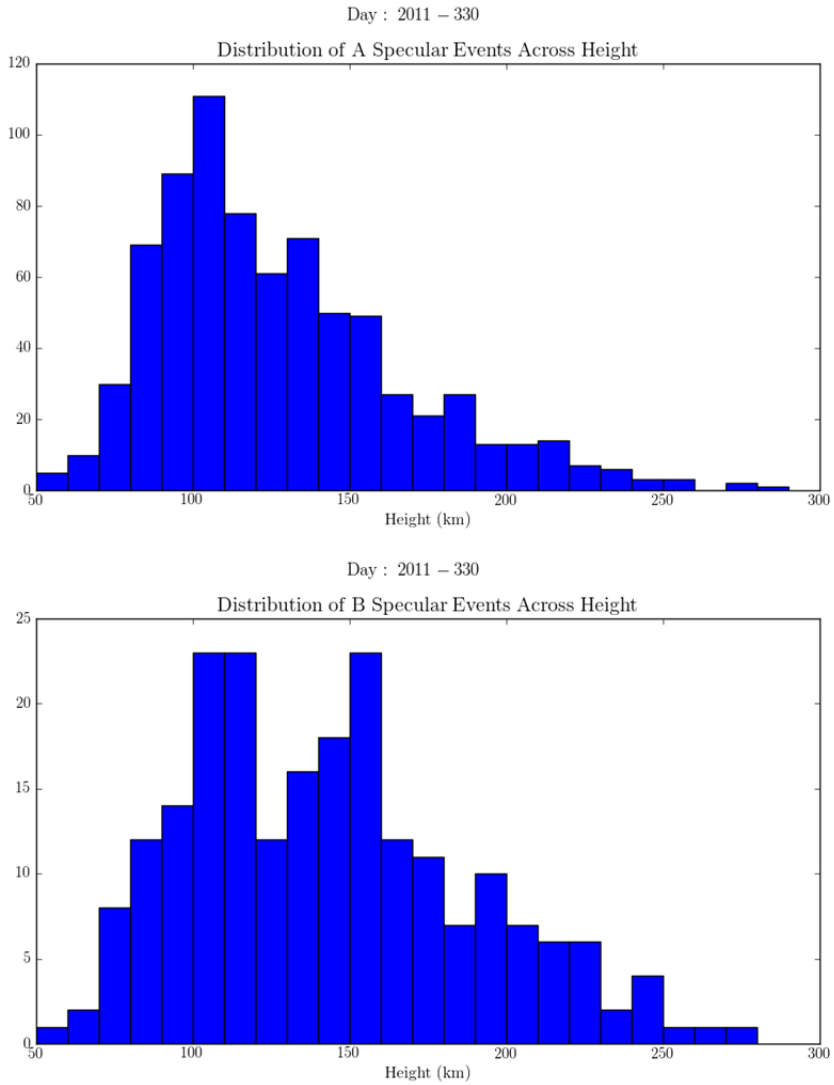

Figure 2: Distribution across height for type A events (top), and type B (bottom). Each bar represents how many events were detected in those 10 km.

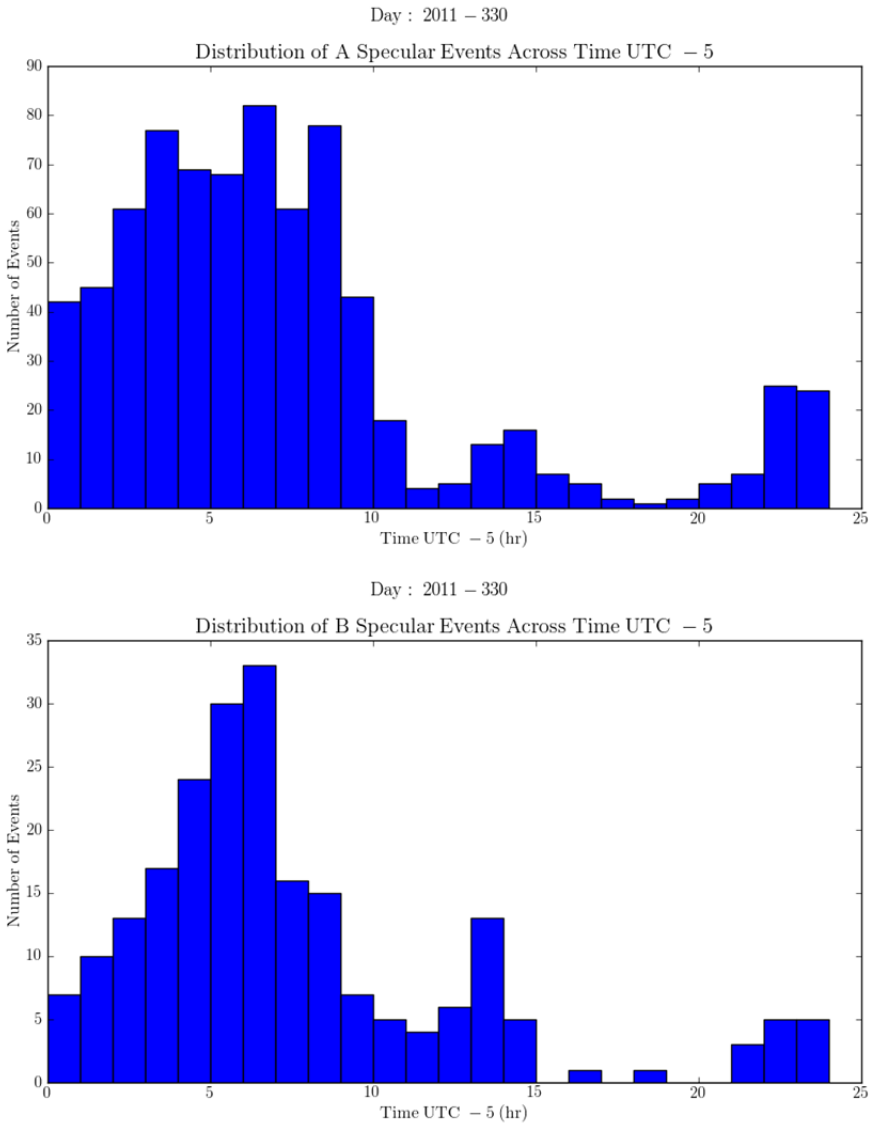

Figure 3: Distribution during the day for type A events (top) and type B (bottom). Each bar represents the number of events registered for that space of one hour.

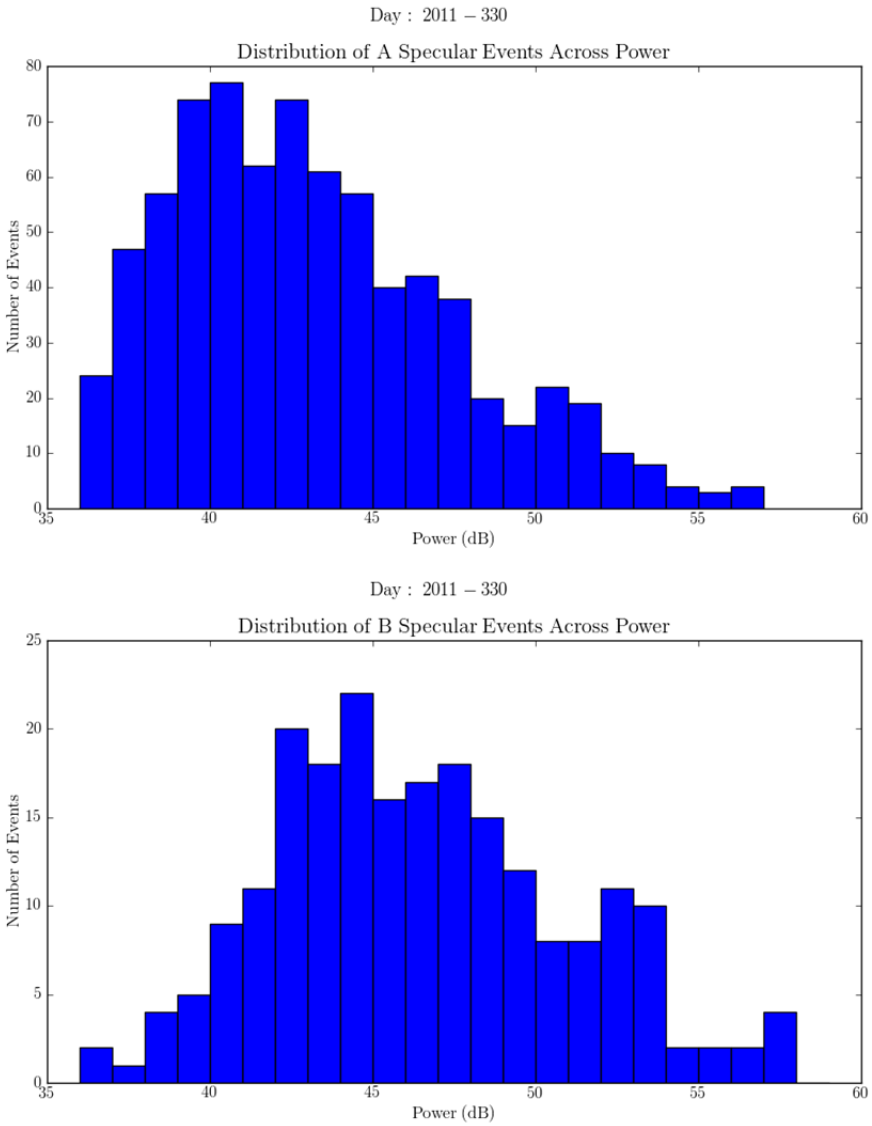

Figure 4: Distribution of Power received for type A events (top) and type B (bottom). Each bar is 1 dB thick

Table 1: Results Summary Table

Specular Type	Height		Hour With Highest Meteor Count (UTC -5)	Power at Receiver	
	Mean (km)	Standard Dev.		Mean (dB)	Standard Dev.
A	127.44	39.84	6am–7am	43.22	4.38
B	142.72	45.01	6am–7am	46.62	4.68

DISCUSSION

A total of 980 events were determined to be specular events, 22% of these events displayed the double signal decay of interest for this paper. The type B events observed appear to occur at a slightly higher altitude than the type A events observed in this dataset as depicted in Table 1. The standard deviation for both populations was very similar. The hour of the day with the highest count was the same for both populations, 6 to 7am (UTC -5), which corresponds to the local sunrise. Both populations also follow similar temporal behavior with a large amount of events occurring in the first few hours of the morning followed by a steep drop in activity as the day progresses. The average signal strength was not very different between both populations with only a difference of 3.4 dB between them.

CONCLUSION

The specular events studied for this paper demonstrate that the new specular signal decay of interest makes up at most 22% of the specular events analyzed in this report. This means that if this trend persists daily for specular meteors, and therefore used to study the ionosphere using Equations (1) and (2), one fifth of them would yield incorrect values. The rest of the results indicate that the population of this type B decay behaves very similarly to the A type population studied. Due to the small dataset used these results will need to be refined through much larger datasets and future research can see larger spans of time along with studies to determine latitudinal dependence for any of the characteristics examined here.

ACKNOWLEDGMENTS

This material is based upon work supported by the National Science Foundation under Grant No. EEC-1062984. Furthermore, I would first like to thank Freddy Galindo Dr Julio V. Urbina and everyone else at the A.S.P.I.R.L lab at Penn. State for patiently mentoring me throughout this summer. I would also like to thank everyone who organized the REU program for this great learning experience.

REFERENCES

[1] W. K. Hocking, T. Thayaparan, and J. Jones “Meteor decay times and their use in determining a diagnostic mesospheric temperature-pressure parameter: methodology and one year of data” *Geophysical Research Letters*, vol. 24, No. 23, pp. 2977-2980, December 1, 1997.

[2] W.K. Hocking “Temperatures using radar-meteor decay times” *Geophysical Research Letters*, Vol. 26, No. 21 pp. 3297-3300, November 1, 1999.

[3] Dimant, Y. S., and M. M. Oppenheim (2006), “Meteor trail diffusion and fields: 1. Simulations”, *J. Geophys. Res.*, *111*, A12312, doi:10.1029/2006JA011797.

[4] “Jicamarca All-sky Specular MEteor Radar (JASMET)” http://jro.igp.gob.pe/english/facilities/JASMET/JASMET.htm [July 7, 2012]

[5] David A. Holdsworth, Iain M. Reid and Maunel A. Cervera “Buckland Park all-sky interferometric meteor radar” *Radio Science*, Vol 36, RS5009, doi:10.1029/203RS003014,2004 October 9, 2004

JOINT SPARSITY BASED COLOR IMAGE CLASSIFICATION

Charles Jeon,* Vishal Monga,[#] and Umamahesh Srinivas[+]

Department of Electrical Engineering
The Pennsylvania State University, University Park, PA 16802

*Undergraduate Student of
Department of Electrical & Systems Engineering
University of Pennsylvania
Philadelphia, PA 19104

ABSTRACT

For many years, sampling theory has been based on Shannon and Nyquist who stated that band-limited signals can be exactly reconstructed using samples acquired at or higher than Nyquist rate (1949). Recently however, the focus has shifted to compressed sensing, where if the underlying signal is sparse, the signal can be represented by a small collection of linear projections. It is now understood that many type of signals, such as images and audio signals, fall into this category. Compressed sensing methods are very useful in applications where taking a large number of measurements of the object is very costly, such as in medical imaging.

Recently norm-minimization ideas from compressed sensing have been adapted for classification tasks via class-specific image dictionaries. The key assumption is that the vectorized versions of training images belonging to the same class lie in a low-dimensional subspace and therefore, any new representation from this image class can be approximated by a linear combination of the training images. The sparse representations of these are naturally discriminative and so, classification can be performed based on reconstruction error. The seminal contribution by Wright *et al.* to face recognition has demonstrated the robustness of this approach to a variety of real-world distortions. In many applications, prior knowledge about a collection of test images belonging to the same class can be exploited to improve classification performance in a joint sparsity setting. In this work, we exploit inter-channel information between the red, green, and blue channels of color images in a joint sparsity framework for the classification of histopathological images.

[#] Faculty Mentor
[+] Graduate Mentor

INTRODUCTION

One of the key theorems that brought many developments in signal processing is the Shannon and Nyquist Sampling Theorem: a band-limited signal can be exactly and uniquely reconstructed by taking samples at twice the highest frequency [1]. For many years, Sampling Theorem has been essential in almost all of the signal acquisition methods used in various electronic applications. For example, a standard digital-to-analog (DAC) and analog-to-digital converter (ADC) relies on the Sampling Theorem extensively to reconstruct or quantize the given signal. However, in the last few years, an alternative theory has been introduced that did not follow the conventional protocol for data acquisition. Compressive Sensing (CS), first introduced by Donoho [2], shows that in special cases, signals can be recovered by far fewer samples or measurements than using traditional methods [3]. The key underlying principle that enables this is that most signals have few non-zero coefficients with respect to some inherent basis, which in CS terminology, is the concept of *sparsity*.

Sparsity suggests that "information rate" of the underlying signal may be much smaller than its bandwidth. In other words, the signal is *compressible*, such that the degree of freedom is smaller than the length of the signal. For instance, a sparse signal can be expressed as a small number of linear combinations in some fixed basis. One of the most common examples of these is found in imaging, using DCT basis for JPEG and wavelets for JPEG2000 [4]. The crucial impact of sparsity is that one can design a new sampling method that can capture the information in a sparse signal and condense it to a small amount of data.

The applications of sparse data representation have been extended to the area of pattern recognition with the development of compressed sensing framework and image processing for sparse modeling of signals. These applications are based on the observation that while the dimension of each individual signal is high, signals in the same class usually share a low-dimensional subspace [5]. Since CS techniques ensure the recoverability of these signals from linear projections, the sample signal can be decomposed over an overcomplete dictionary generated by a set of representative samples. Many applications have been shown in literature in various fields, such as image restoration [6], super-resolution [7], target detection [8], and face recognition [9].

Recently, the applications of sparsity framework have been extended to classification tasks. Wright *et al.*, have demonstrated that sparse signal representations have a robust performance in face recognition. Moreover, the Sparse Representation-based Classification (SRC) approach has been shown to outperform the conventional methods, Principal Component Analysis (PCA) and Independent Component Analysis (ICA) methods under random corruption and contiguous occlusion in images [9]. Face recognition is often times a hard problem due to high variability in the process of acquiring face images, which necessitates robust algorithms. Suppose that we are to collect a number of images for an individual in various settings such as, luminosity, color balance and occlusions. Provided that we have a sufficient number of images, it will be

possible to represent any test image of the individual as a linear combination of the previously collected images. In macroscopic view with many individuals, this representation is sparse, involving only a small number of samples of our image database. In many cases, seeking the sparsest representation automatically discriminates between the various classes present in the training set [9].

In hyperspectral image classification, it is quite typical to observe that a local neighborhood of objects observe similar class behavior. Conversely, if some objects are known to belong to an identical class or share a common class behavior, the additional information can be exploited in using sparse models in classification. Joint sparsity comes from the fact that additional information can be obtained by exploiting correlation, e.g., a common sparsity pattern, across neighboring objects [10].

By using joint sparsity model, we propose the idea of extending image classification to multispectral (color) images. While much research has been focused on grayscale images for representing their spatial structure, additional information could be exploited by utilizing color images. One of the difficulties in straightforward adoption of grayscale classification methods to each individual color channel is that it ignores inherent correlation among the color channels. Also, by considering multiple channels, the overall complexity increases. Although exploiting multispectral images for face recognition has already been introduced in literature [11], we propose a new joint-sparse model for color framework. Since SRC approach has shown robust performance in grayscale images, we expect to observe that color-based SRC will also demonstrate a strong performance in classification.

In this project, we extend the previous ideas of a sparsity-based model to construct a joint sparse model using color channels for image classification. In Section 2, basic classification model along with joint sparsity model proposed in literature [9], [10] is reviewed. In the next section, Section 3, color-based sparse model is formulated along with an additional optimization problem to guarantee optimality. In Section 4, we propose our methodology to solve the introduced problem along with simulation results of histopathological images for bovine organs.

While our simulation results are applied to medical images, our framework is of broad interest to object classification in general. Many feature extraction methods and the use of contrast agents with machine-learning mechanisms have been used in medical imaging [12], [13], but we concentrate on a general SRC based approach here.

CLASSIFICATION BASED ON SPARSE REPRESENTATION

Classification, a general form of automatic (machine) recognition, description, and pattern recognition, is an example of supervised learning, where a training set of correctly identified observations is available, to identify which set of categories an observation belongs [14]. Although unsupervised classification methods exist, our primary focus is on supervised classification. Formally speaking, a

classification problem can be defined as using some set of training samples from M distinct object classes to correctly determine the class to which the new test sample(s) belongs. If we denote N_k as the number of training samples from the k-th class, we can arrange the training samples $\{\boldsymbol{a}_i^k\}$, $i = 1, \ldots N_k$ as the columns of a matrix, $\boldsymbol{A}^k = \left[\boldsymbol{a}_1^k\ \boldsymbol{a}_2^k \cdots \boldsymbol{a}_{N_k}^k\right]$. We will refer to $\boldsymbol{A}^k$ as our dictionary matrix. We follow lexicographical ordering for characterizing images in the following subsections.

General Sparsity Classification Model

Many previous works have been done to exploit the structure of $\boldsymbol{A}^k$ for classification. One particular approach we consider here is approximately modeling the samples from a single class as lying on a linear subspace as subspace models are flexible enough to capture much of the variation in real data [5]. Thus, given sufficient training samples of the m-th class, $\boldsymbol{A}^m \in \mathbb{R}^{B \times N_m}$, any new sample $\boldsymbol{y} \in \mathbb{R}^B$ from the same class can be approximately expressed as a linear combination of the training samples,

$$\begin{aligned} \boldsymbol{y} &= \alpha_1^m \boldsymbol{a}_1^m + \alpha_2^m \boldsymbol{a}_2^m + \cdots + \alpha_{N_m}^m \boldsymbol{a}_{N_m}^m \\ &= \left[\boldsymbol{a}_1^m\ \boldsymbol{a}_2^m\ \cdots\ \boldsymbol{a}_{N_m}^m\right] \left[\alpha_1^m\ \alpha_2^m\ \cdots\ \alpha_{N_m}^m\right]^T = \boldsymbol{A}^m \boldsymbol{\alpha}^m \end{aligned}$$

for some weight vector $\boldsymbol{\alpha}^m \in \mathbb{R}^{N_m}$.

Although the class of the test sample is initially unknown, we can deduce that it is modeled to lie in the union of the M distinct subspaces associated with the M classes. Thus, we can combine the sub-dictionary matrices $\boldsymbol{A}^m$, $m \in \{1, \ldots, M\}$ to define a new dictionary matrix $\boldsymbol{A}$ for the entire collection of training samples,

$$\begin{aligned} \boldsymbol{y} &= \boldsymbol{A}^1 \boldsymbol{\alpha}^1 + \boldsymbol{A}^2 \boldsymbol{\alpha}^2 + \cdots + \boldsymbol{A}^m \boldsymbol{\alpha}^m \\ &= \left[\ \boldsymbol{A}^1 \ \cdots \ \boldsymbol{A}^m\ \right] \begin{bmatrix} \boldsymbol{\alpha}^1 \\ \vdots \\ \boldsymbol{\alpha}^m \end{bmatrix} = \boldsymbol{A}\boldsymbol{\alpha} \end{aligned} \tag{1}$$

where $\boldsymbol{A} \in \mathbb{R}^{B \times N}$ is a dictionary matrix composed of all the training samples with $N = \sum_{i=1}^{M} N_m$ and weight vector $\boldsymbol{\alpha} \in \mathbb{R}^N$ formed by stacking the individual $\boldsymbol{\alpha}^j$ vectors for all $j \in \{1, \ldots, M\}$. Note that ideally, if $\boldsymbol{y}$ belongs to j-th class, then $\boldsymbol{\alpha}^i = \boldsymbol{0}$ for $i = 1, \ldots, M, i \neq j$. In our sparsity model, $\boldsymbol{\alpha}$ is a sparse vector, which corresponds to few non-zero entries. Note that Equation (1) can also be written as a linear combination of only the K active dictionary elements or atoms, $\{\boldsymbol{a}_{\lambda_k}\}$ corresponding to the K non-zero entries of $\{\boldsymbol{a}_{\lambda_k}\}$, $k \in \{1, \ldots, K\}$,

$$\begin{aligned} \boldsymbol{y} &= \alpha_{\lambda_1}\boldsymbol{a}_{\lambda_1} + \alpha_{\lambda_2}\boldsymbol{a}_{\lambda_2} + \cdots + \alpha_{\lambda_K}\boldsymbol{a}_{\lambda_K} \\ &= \begin{bmatrix} \boldsymbol{a}_{\lambda_1} & \cdots & \boldsymbol{a}_{\lambda_K} \end{bmatrix} \begin{bmatrix} \alpha_{\lambda_1} \\ \vdots \\ \alpha_{\lambda_K} \end{bmatrix} = \boldsymbol{A}_{\Lambda_K}\boldsymbol{\alpha}_{\Lambda_K} \end{aligned} \tag{2}$$

where K can be expressed as $K = \|\boldsymbol{\alpha}\|_0$ which denotes the sparsity level or l_0 norm of $\boldsymbol{\alpha}$. The index set $\Lambda_K = \{\lambda_1, \ldots, \lambda_K\}$ denotes the support of $\boldsymbol{\alpha}$, $\boldsymbol{A}_{\Lambda_K}$ is $B \times K$ matrix whose columns are the K dictionary elements of $\{\boldsymbol{a}_k\}, k \in \Lambda_K$ and $\boldsymbol{\alpha}_{\Lambda_K}$ is a K-dimensional vector consisting of the entries of $\boldsymbol{\alpha}$ indexed by Λ_K.

Classification model for joint sparsity

Recall that we can exploit the spatial correlation across neighboring pixels if they share a common sparsity pattern [10]. In other words, we would be able to make a better guess if we are given groups of test samples that are known to belong to the same class.

Suppose that $\boldsymbol{y}_i$ and $\boldsymbol{y}_j$ are images that belong to the same class. Recall from Equation (2) that $\boldsymbol{y}_i$ can be expressed as $\boldsymbol{y}_i = \boldsymbol{A}\boldsymbol{\alpha}_i = \alpha_{i,\lambda_1}\boldsymbol{a}_{\lambda_1} + \cdots + \alpha_{i,\lambda_K}\boldsymbol{a}_{\lambda_K}$ for some index set $\Lambda_K = \{\lambda_i\}_i$, some sparse coefficient vector $\boldsymbol{\alpha}_i$, and some dictionary $\boldsymbol{A}$. Since $\boldsymbol{y}_j$ was defined to be in the same class as $\boldsymbol{y}_i$, $\boldsymbol{y}_j$ can also be approximated by the same set of training samples $\{\boldsymbol{a}_{\Lambda_k}\}_k$,

$$\boldsymbol{y}_j = \boldsymbol{A}\boldsymbol{\alpha}_j = \alpha_{j,\lambda_1}\boldsymbol{a}_{\lambda_1} + \alpha_{j,\lambda_2}\boldsymbol{a}_{\lambda_1} + \cdots + \alpha_{j,\lambda_K}\boldsymbol{a}_{\lambda_K}$$

Now, we extend this idea to a general joint sparsity model. Suppose we have T different images given by $\boldsymbol{Y} = [\boldsymbol{y}_1 \ \cdots \ \boldsymbol{y}_T]$ a $B \times T$ matrix, where each column $\boldsymbol{y}_j$ denotes the j-th image belonging to some class m. Then, using the ideas explained previously, we have that

$$\begin{aligned} \boldsymbol{Y} &= [\boldsymbol{y}_1 \ \boldsymbol{y}_2 \ \cdots \ \boldsymbol{y}_T] = [\boldsymbol{A}\boldsymbol{\alpha}_1 \ \boldsymbol{A}\boldsymbol{\alpha}_2 \ \cdots \ \boldsymbol{A}\boldsymbol{\alpha}_T] \\ &= \boldsymbol{A}\,[\boldsymbol{\alpha}_1 \ \boldsymbol{\alpha}_2 \ \cdots \ \boldsymbol{\alpha}_T] = \boldsymbol{A}\boldsymbol{S} \end{aligned}$$

where $\boldsymbol{S} = [\boldsymbol{\alpha}_1 \ \cdots \ \boldsymbol{\alpha}_T]$ is a $N \times T$ matrix consisting of the sparse vectors $\{\boldsymbol{\alpha}_j\}$ corresponding to each image $\boldsymbol{y}_j$. Note that the sparse vectors $\{\boldsymbol{\alpha}_j\}$ share the same support Λ_K, thus $\boldsymbol{S}$ is a structured *sparse* matrix with only K non-zero rows.

Reconstruction

The first step in the classification process is to consider a reconstruction problem of finding the sparse matrix $\boldsymbol{S}$ for some set of test sample $\boldsymbol{Y}$. Given a dictionary of training image samples $\boldsymbol{A}$ for the test samples $\boldsymbol{y}_j$, we wish to solve the following optimization problem,

$$\hat{\boldsymbol{S}} = \arg\min \|\boldsymbol{S}\|_{row,0} \quad \text{subject to} \quad \boldsymbol{A}\boldsymbol{S} = \boldsymbol{Y} \tag{3}$$

where the operator $\|\boldsymbol{S}\|_{row,0}$ denotes the number of non-zero rows of $\boldsymbol{S}$. Note that for $T = 1$, where we have a single image, the problem reduces to a generic sparsity problem,

$$\hat{\boldsymbol{\alpha}} = \arg\min \|\boldsymbol{\alpha}\|_0 \quad \text{subject to} \quad \boldsymbol{A}\boldsymbol{\alpha} = \boldsymbol{y}$$

Therefore, we will consider the general joint sparsity based model throughout the paper. Now, we can modify Equation (3) to relax the equality constraint for approximation errors in empirical data to

$$\hat{\boldsymbol{S}} = \arg\min \|\boldsymbol{S}\|_{row,0} \quad \text{subject to} \quad \|\boldsymbol{A}\boldsymbol{S} - \boldsymbol{Y}\|_F \leq \sigma \tag{4}$$

where $\sigma > 0$ is the error tolerance and $\|\cdot\|_F$ denotes the Frobenius norm. This can be also interpreted as minimizing the approximation error given some sparsity level [15],

$$\hat{\boldsymbol{S}} = \arg\min \|\boldsymbol{A}\boldsymbol{S} - \boldsymbol{Y}\|_F \quad \text{subject to} \quad \|\boldsymbol{S}\|_{row,0} \leq K_0 \tag{5}$$

where K_0 is an upper bound on the sparsity level. While the problems in Equations (3), (4), and (5) are all NP-hard, many approximation methods have been introduced to make these problems solvable in polynomial time [16], [17], [18]. One particular approximation method that we will exploit in this paper is the greedy pursuit algorithm known as Simultaneous Orthogonal Matching Pursuit (S-OMP) [19], [20]. The intuition behind S-OMP is that it picks the atoms that contribute the most energy to every column of the signal matrix in each iteration. The S-OMP algorithm finds the support of the sparse vector that approximately solves Equation (5). At each iteration, S-OMP picks the dictionary element that maximizes the residual norm and creates an orthogonal projection onto the residual matrix. After K_0 iterations, S-OMP returns the set of K_0 atoms that contribute most of the energy in the signal. The algorithm is summarized below in Algorithm 1. Note for l_p norm, $p = 1$ is used in [19], but we use $p = 2$, used in [20].

Now, the obtained row-sparse matrix $\hat{\boldsymbol{S}}$ can be used to determine the class of $\boldsymbol{Y}$ by considering the error residuals between the original test samples and the approximation obtained from each class sub-dictionary:

$$r^m(\boldsymbol{Y}) = \left\| \boldsymbol{Y} - \boldsymbol{A}^m \hat{\boldsymbol{S}}^m \right\|_F, \qquad m = 1, 2, \ldots, M \tag{6}$$

where $\hat{\boldsymbol{S}}^m$ consists of the N_m rows in $\hat{\boldsymbol{S}}$ that are associated with the m-th class sub-dictionary $\boldsymbol{A}^m$ in Section 2. After computing all the $\{r^m(\boldsymbol{Y})\}_m$, the label of $\boldsymbol{Y}$ is given as the class with minimum total residual,

$$\text{Class}(\boldsymbol{Y}) = \arg \min_{i=1,\ldots,M} r^m(\boldsymbol{Y}) \tag{7}$$

Algorithm 1: S-OMP Algorithm

Input: $B \times N$ dictionary matrix $\boldsymbol{A} = [\boldsymbol{a}_1 \ \cdots \ \boldsymbol{a}_N]$, $B \times T$ signal matrix $\boldsymbol{Y} = [\boldsymbol{y}_1 \ \cdots \ \boldsymbol{y}_T]$, and number of iterations K.

Initialization: residual $\boldsymbol{R}_0 = \boldsymbol{Y}$, index set $\Lambda_0 = \phi$, iteration counter $k = 1$

while $k \leq K$ **do**

(1) Find the index of the atom that best approximates all residuals: $\lambda_k = \arg \max_{i=1,\ldots,N} \left\| \boldsymbol{R}_{k-1}^T \boldsymbol{a}_i \right\|_p, p \geq 1$

(2) Update the index set $\Lambda_k = \Lambda_{k-1} \bigcup \{\lambda_k\}$

(3) Compute the orthogonal projector $\boldsymbol{P}_k = \left(\boldsymbol{A}_{\Lambda_k}^T \boldsymbol{A}_{\Lambda_k}\right)^{-1} \boldsymbol{A}_{\Lambda_k}^T \boldsymbol{Y} \in \mathbb{R}^{k \times T}$ where $\boldsymbol{A}_{\Lambda_k} \in \mathbb{R}^{B \times k}$ consists of the k atoms in $\boldsymbol{A}$ indexed in Λ_k

(4) Update the Residual Matrix $\boldsymbol{R}_k = \boldsymbol{Y} - \boldsymbol{A}_{\Lambda_k} \boldsymbol{P}_k$

(5) Increment k: $k \leftarrow k + 1$

end while

Output: Index set $\Lambda = \Lambda_K$, the sparse representation $\hat{\boldsymbol{S}}$ whose non-zero rows index by Λ are the K rows of the matrix $\left(\boldsymbol{A}_{\Lambda_K}^T \boldsymbol{A}_{\Lambda_K}\right)^{-1} \boldsymbol{A}_{\Lambda_K}^T \boldsymbol{Y}$

COLOR-BASED SPARSE REPRESENTATION

Every color image $\boldsymbol{X}$ is composed of three distinct channels, $\boldsymbol{X} = [\boldsymbol{x}_r \ \boldsymbol{x}_g \ \boldsymbol{x}_b] \in \mathbb{R}^{B \times 3}$ where the subscripts r, g, b correspond to the red, green, and blue color channels respectively. The training dictionary matrix $\boldsymbol{A}$ is redefined as $\boldsymbol{A} = [\boldsymbol{A}_r \ \boldsymbol{A}_g \ \boldsymbol{A}_b] \in \mathbb{R}^{B \times 3N}$. For simplicity, let us assume that we have L training samples from each of the M distinct classes so that $N = ML$. Therefore, we define each *color* dictionary $\boldsymbol{A}_c = \left[\boldsymbol{A}_c^1 \ \boldsymbol{A}_c^2 \ \ldots \ \boldsymbol{A}_c^M\right] \in \mathbb{R}^{B \times ML}$, $c \in \{r, g, b\}$ as the concatenation of the sub-dictionaries from all classes belonging to the same color channel. We note that the color dictionaries are designed to obey column correspondence, i.e., the i-th column of the training samples for the three color channels correspond to the i-th image.

Joint Sparsity Model for Color Images

With the notations in place, the test color image $\boldsymbol{X}$ can now be represented as a linear combination of training samples as follows:

$$\boldsymbol{X} = \boldsymbol{A}\boldsymbol{S} = \left[\boldsymbol{A}_r^1 \ldots \boldsymbol{A}_r^M \ \boldsymbol{A}_g^1 \ldots \boldsymbol{A}_g^M \ \boldsymbol{A}_b^1 \ldots \boldsymbol{A}_b^M\right] [\boldsymbol{\alpha}_r \ \boldsymbol{\alpha}_g \ \boldsymbol{\alpha}_b] \tag{8}$$

where the coefficient vectors $\boldsymbol{\alpha}_r, \boldsymbol{\alpha}_g, \boldsymbol{\alpha}_b \in \mathbb{R}^{3ML}$ and $\boldsymbol{S} = [\boldsymbol{\alpha}_r \ \boldsymbol{\alpha}_g \ \boldsymbol{\alpha}_b] \in \mathbb{R}^{3ML \times 3}$.

We first start by examining the structure of the coefficient matrix $\boldsymbol{S}$. As we can assume that each color channel $c \in \{r, g, b\}$ of the test color image can be approximately represented by the span of the training samples belonging to the same color channel, the columns of $\boldsymbol{S}$ has the following structure,

$$\boldsymbol{\alpha}_r = \begin{bmatrix} \boldsymbol{\alpha}_r^1 \\ \vdots \\ \boldsymbol{\alpha}_r^M \\ \mathbf{0} \\ \mathbf{0} \end{bmatrix}, \boldsymbol{\alpha}_g = \begin{bmatrix} \mathbf{0} \\ \boldsymbol{\alpha}_g^1 \\ \vdots \\ \boldsymbol{\alpha}_g^M \\ \mathbf{0} \end{bmatrix}, \boldsymbol{\alpha}_b = \begin{bmatrix} \mathbf{0} \\ \mathbf{0} \\ \boldsymbol{\alpha}_b^1 \\ \vdots \\ \boldsymbol{\alpha}_b^M \end{bmatrix}$$

where each of the sub-vectors $\left\{\boldsymbol{\alpha}_c^k\right\}_k \in \mathbb{R}^L$ for all $c \in \{r, g, b\}$ and $\mathbf{0} \in \mathbb{R}^{ML}$ denotes the zero vector. We note that $\boldsymbol{S}$ exhibits block-diagonal structure.

Recalling the similarity to our model formation for grayscale images in Section 2, each color channel of the test image can be represented by a sparse linear combination of the sub-dictionaries of the training samples in that color channel. Furthermore, the non-zero weights of color training samples in the linear combination exhibit one-to-one correspondence across channels. In mathematical notation, this implies that if l-th training sample from the m-th class has a non-zero coefficient in its weights for some color channel c, it is also necessarily non-zero for the other color channels. This suggests a joint sparsity model similar to the model introduced previously. However, the construction of $\boldsymbol{S}$ does not permit us to apply previous l_0 row-sparsity framework. Since $\boldsymbol{S}$ obeys column correspondence, we introduce matrix $\boldsymbol{S}' \in \mathbb{R}^{ML \times 3}$ as the transformation of matrix $\boldsymbol{S}$ with the zero coefficients removed,

$$\boldsymbol{S}' = \begin{bmatrix} \boldsymbol{\alpha}_r^1 & \boldsymbol{\alpha}_g^1 & \boldsymbol{\alpha}_b^1 \\ \vdots & \vdots & \vdots \\ \boldsymbol{\alpha}_r^M & \boldsymbol{\alpha}_g^M & \boldsymbol{\alpha}_b^M \end{bmatrix}$$

With the clever formation of $\boldsymbol{S}'$, we can now apply row-sparsity similar to Equation (4). By taking into account the approximation error, our problem becomes

$$\hat{\boldsymbol{S}}' = \arg\min \|\boldsymbol{S}'\|_{row,0} \quad \text{subject to} \quad \|\boldsymbol{X} - \boldsymbol{A}\boldsymbol{S}\|_F \leq \epsilon \tag{9}$$

for some tolerance $\epsilon > 0$. Note that we are trying to minimize the number of non-zero rows, while the constraint guarantees a good approximation.

Transformation of $\boldsymbol{S}$

We wish to address the particular method of transforming $\boldsymbol{S}$ by introducing matrices $\boldsymbol{H} \in \mathbb{R}^{3ML \times 3}$ and $\boldsymbol{J} \in \mathbb{R}^{ML \times 3ML}$,

$$\boldsymbol{H} = \begin{bmatrix} \mathbf{1} & \mathbf{0} & \mathbf{0} \\ \mathbf{0} & \mathbf{1} & \mathbf{0} \\ \mathbf{0} & \mathbf{0} & \mathbf{1} \end{bmatrix}, \boldsymbol{J} = [\boldsymbol{I}_{ML}\ \boldsymbol{I}_{ML}\ \boldsymbol{I}_{ML}]$$

where $\mathbf{1}, \mathbf{0} \in \mathbb{R}^{ML}$ are vector containing all ones and zeros respectively, and $\boldsymbol{I}_{ML}$ denotes the ML-dimensional identity matrix. Thus we have the operation $\boldsymbol{S}' = \boldsymbol{J}(\boldsymbol{H} \circ \boldsymbol{S})$ where $\circ$ denotes the Hadamard product, where $(\boldsymbol{H} \circ \boldsymbol{S})_{ij} \triangleq h_{ij} s_{ij}$ for all i, j.

Refining the Choice of $\boldsymbol{S}$

The cost function of Equation (9) is non-convex, and thus any solution obtained is suboptimal. To improve the solution, we propose a convex auxiliary optimization problem, thus guaranteeing a unique minimum solution for the additional problem. From the initially obtained solution $\hat{\boldsymbol{S}}'$ we construct $\hat{\boldsymbol{S}}$ by inserting zeros appropriately. Then, we design a membership matrix $\boldsymbol{E} \in \mathbb{R}^{3ML \times 3}$ which has zeros at locations of non-zero entries in $\hat{\boldsymbol{S}}$ and ones elsewhere, that is, $e_{ij} = \mathbf{1}\{\hat{s}_{ij} = 0\}$ for all i, j, where $\mathbf{1}$ is the indicator function. With the introduction of the membership matrix $\boldsymbol{E}$, we have the following optimization problem,

$$\hat{\boldsymbol{S}} = \arg\min \|\boldsymbol{X} - \boldsymbol{A}\boldsymbol{S}\|_F \quad \text{subject to} \quad \boldsymbol{s}_i^T \boldsymbol{e}_i = 0, i = 1, 2, 3 \tag{10}$$

where $\boldsymbol{s}_i$ and $\boldsymbol{e}_i$ denotes the i-th column of $\boldsymbol{S}$ and $\boldsymbol{E}$.

To mitigate computational complexity, we can simplify the problem further. Each column of $\boldsymbol{S}$ can be optimized in parallel since the constraints are separable. Therefore, the preceding optimization problem can be simplified to:

$$\hat{\boldsymbol{s}}_1 = \arg\min \|\boldsymbol{x}_r - \boldsymbol{A}\boldsymbol{s}_1\|_2 \quad \text{subject to} \quad \boldsymbol{e}_1^T \boldsymbol{s}_1 = 0 \tag{11}$$

and similarly for $\hat{\boldsymbol{s}}_2$ and $\hat{\boldsymbol{s}}_3$ for green and blue channels respectively. If we denote the three columns of $\boldsymbol{S}'$ as $\boldsymbol{s}_r, \boldsymbol{s}_g, \boldsymbol{s}_b$ and the corresponding columns of $\boldsymbol{E}$ as $\boldsymbol{e}_r, \boldsymbol{e}_g, \boldsymbol{e}_b$, we can exploit the knowledge of the locations of the non-zero coefficients to remove the redundant columns from dictionary matrix $\boldsymbol{A}$ and solve three quadratic programming problems for $c \in \{r, g, b\}$ in parallel:

$$\hat{\boldsymbol{s}}_c = \arg\min \|\boldsymbol{x}_c - \boldsymbol{A}_c \boldsymbol{s}_c\|_2 \quad \text{subject to} \quad \boldsymbol{e}_c^T \boldsymbol{s}_c = 0 \tag{12}$$

S-OMP Algorithm for Color Joint Sparsity Model

While Equation (9) looks quite similar to our proposed joint sparsity model in Equation (4), the Hadamard operator from $\boldsymbol{S}$ to $\boldsymbol{S}'$ makes the problem much more complex. Without the Hadamard operator in Equation (12), we can relax the row-sparse l_0 norm to a general $\|\cdot\|_{p,q}$ norm [22]. We note the fact that we can make a unique $\boldsymbol{S}$ from $\boldsymbol{S}'$ by inserting zeros appropriately, while the converse does not hold.

Since the original S-OMP algorithm effectively gives K_0 distinct atoms from a dictionary $\boldsymbol{A}$ that best approximates the data matrix $\boldsymbol{Y}$ for K_0 iterations, we apply the general formulation even when the Hadamard operator is present. Recall that

at every iteration k, S-OMP measures the residual for each atom in $\boldsymbol{A}$ and creates an orthogonal projection with the highest correlation. If we adopt this scheme to color image setting, for every color channel c, we can identify the index set $\Lambda_k = [\Lambda_{r,k}\ \Lambda_{g,k}\ \Lambda_{b,k}]$ that give the highest correlation value:

$$\lambda_k = \arg \max_{i=1,\ldots,M} \sum_{c\in\{r,g,b\}} w(c) \left\| \boldsymbol{R}_c^T \boldsymbol{a}_{c,i} \right\|_p$$

where $w(c)$ denotes the weight of each color channel and $p \geq 1$. After finding λ_k, we modify the index setup to, $\{\Lambda_{c,k}\} = \{\Lambda_{c,k-1} \bigcup \lambda_{c,k}\}$ for $c \in \{r,g,b\}$. Thus, by finding the index set for the three distinct color channels based on some weight vector, we can create an orthogonal projection with each of the atoms in their corresponding color channels. The algorithm is summarized below in Algorithm 2.

Algorithm 2: Color Channel S-OMP Algorithm

Input: $B \times 3ML$ dictionary matrix $\boldsymbol{A} = [\boldsymbol{A}_r\ \boldsymbol{A}_g\ \boldsymbol{A}_b\ ]$ with $\boldsymbol{A}_c = \left[\boldsymbol{A}_c^1\ \cdots \boldsymbol{A}_c^M\right] \in \mathbb{R}^{B\times ML}$ for $c \in \{r,g,b\}$, $B \times 3$ signal matrix $\boldsymbol{Y} = \left[\boldsymbol{y}_r\ \boldsymbol{y}_g\ \boldsymbol{y}_b\right]$, and number of iterations K

Initialization: Residual $\boldsymbol{R}_0 = \boldsymbol{Y}$, index set $\Lambda_0 = \phi$, iteration counter $k = 1$

while $k \leq K$ **do**

(1) Find the index of the atom that best approximates all residuals: $\lambda_k = \arg \max_{i=1,\ldots,M} \sum_{c\in\{r,g,b\}} w(c) \left\| \boldsymbol{R}_c^T \boldsymbol{a}_{c,i} \right\|_p, p \geq 1$

(2) Update the index set $\Lambda_{c,k} = \Lambda_{c,k-1} \bigcup \{\lambda_{c,k}\}$ for each $c \in \{r,g,b\}$

(3) Compute the orthogonal projector $\boldsymbol{P}_{c,k} = \left(\boldsymbol{A}_{\Lambda_{c,k}}^T \boldsymbol{A}_{\Lambda_{c,k}}\right)^{-1} \boldsymbol{A}_{\Lambda_{c,k}}^T \boldsymbol{Y}_c \in \mathbb{R}^k$ where $\boldsymbol{A}_{\Lambda_{c,k}} \in \mathbb{R}^{B\times k}$ consists of the k atoms in $\boldsymbol{A}$ indexed in $\Lambda_{c,k}$ for each color channel $c \in \{r,g,b\}$

(4) Update the Residual Matrix $\boldsymbol{R}_k = \boldsymbol{Y} - \left[\boldsymbol{A}_{\Lambda_{r,k}} \boldsymbol{P}_{r,k}\ \boldsymbol{A}_{\Lambda_{g,k}} \boldsymbol{P}_{g,k}\ \boldsymbol{A}_{\Lambda_{b,k}} \boldsymbol{P}_{b,k}\right]$

(5) Increment k: $k \leftarrow k+1$

end while

Output: Index set $\Lambda_c = \Lambda_{c,K}$, the sparse representation $\hat{\boldsymbol{S}}$ whose non-zero rows index for each color channel $c \in \{r,g,b\}$ by Λ_c are the K rows of the matrix $\left(\boldsymbol{A}_{\Lambda_{c,K}}^T \boldsymbol{A}_{\Lambda_{c,K}}\right)^{-1} \boldsymbol{A}_{\Lambda_{c,K}}^T \boldsymbol{Y}_c$

Solving the Auxiliary Optimization Problem

The optimization problem in Equation (12) is convex and thus there exists a unique $\boldsymbol{s}_c^*$ for each $c \in \{r,g,b\}$ that solves the problem. We use the $\hat{\boldsymbol{S}}'$ from the modified S-OMP to construct the initial membership matrix $\boldsymbol{E}$. Without any additional constraints, we obtain a closed form solution for $\boldsymbol{s}_c^*$.

Problem 1: The unique solution $\boldsymbol{s}_c^*$ for the optimization problem in Equation (12) is given as

$$\boldsymbol{s}_c^* = -\boldsymbol{H}_c^{-1}\left(\boldsymbol{c}_c - \boldsymbol{e}_c\lambda\right) \tag{13}$$

where $\boldsymbol{H}_c = \boldsymbol{A}_c^T\boldsymbol{A}_c$, $\boldsymbol{c}_c = -\boldsymbol{A}_c^T\boldsymbol{x}_c$, and $\lambda = \left(\boldsymbol{e}_c^T\boldsymbol{H}_c^{-1}\boldsymbol{e}_c\right)^{-1}\boldsymbol{e}_c^T\boldsymbol{H}_c^{-1}\boldsymbol{c}_c$. Proof is shown in Appendix.

While Equation (15) gives the unique minimizer solution in Equation (12), we require a positivity constraint as negative coefficient in images would not have a physical meaning. Thus, we introduce a constraint $\boldsymbol{s}_c \geq 0$ to solve Equation (12). Note that with the additional inequality constraint, we forgo the closed form solution found above. Therefore, we use iterative methods to solve the problem. More specifically, we utilize interior point convex method for MATLAB's `quadprog` in the Optimization Toolbox.

Therefore, with the addition of the positivity constraint, solving the auxiliary optimization problem has two implications. If we use $\hat{\boldsymbol{S}}'$ obtained from any numerical solvers using any algorithms, the auxiliary optimization problem may improve the solution while guaranteeing sparsity. On the other hand, if we use S-OMP, the auxiliary problem only imposes positivity conditions since S-OMP results in the best selection of atoms in a given sparsity level.

Classification

After solving the auxiliary optimization problem to get an improved solution $\hat{\boldsymbol{s}}_c$ for all $c \in \{r, g, b\}$ and obtaining the sparse coefficient matrix $\boldsymbol{S}$, we compute the class-specific residual errors and finally identify the class of the test image $\boldsymbol{X}$ which gives the minimum residual as Equations (6) and (7):

$$\text{Class}\left(\boldsymbol{X}\right) = \arg\min_{i=1,\ldots,M} \left\|\boldsymbol{X} - \boldsymbol{A}\delta_i\left(\boldsymbol{S}\right)\right\|_F \tag{14}$$

where $\delta_i\left(\boldsymbol{S}\right)$ is the matrix whose only non-zero entries are the same as those in $\boldsymbol{S}$ associated with class i in all color channels.

SIMULATION RESULTS

The images that will be used to test the performance of our joint sparsity model are histopathological images provided by the Animal Diagnostics Laboratory (ADL) at Pennsylvania State University. Before we present the results, we start by describing the photomicrographs used for testing.

Histopathological Image Classification Process

The image database consists of photomicrographs of four different bovine organs: liver, lung, kidney, and spleen. The different conditions corresponding to each bovine organ are summarized in Table 1. The descriptions of the visual characteristics of each condition are shown below in Sections 4.1.1 through 4.1.4.

Table 1: Bovine Organ and Corresponding Conditions

Bovine Organ	Tissue Condition
Liver	Healthy
	Inflammation
Lung	Healthy
	Inflammation
	Necrosis
Kidney	Healthy
	Inflammation
Spleen	Healthy
	Inflammation

Lung photomicrographs

Some examples of lung images of the photomicrographs are shown in Figures 1 and 2. We note the fact that healthy lung images share a common trait of having white regions in the photomicrographs, whereas inflammation conditions do not.

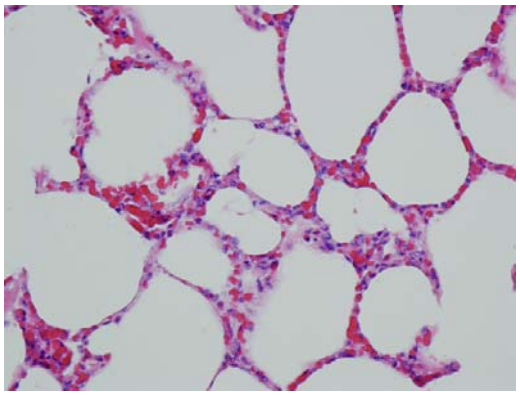

Figure 1: Healthy Lung Tissue

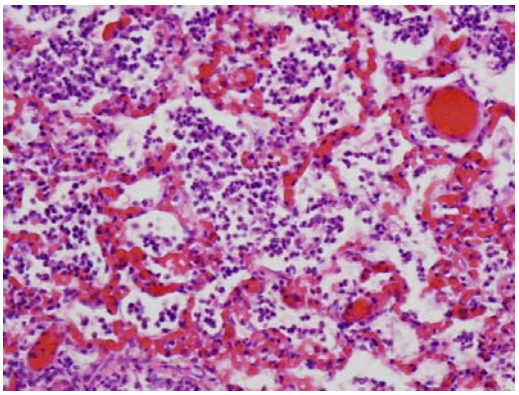

Figure 2: Inflammatory Lung Tissue

Liver Photomicrographs

Next, the photomicrographs of liver are shown in Figures 3, 4, and 5. Although the liver tissue does not experience white regions like the lung, the images reflect a certain characteristic to each condition. The healthy liver tissue has nuclei, the blue dots that are uniformly scattered in the image. On the other hand, the inflammatory tissue has a large cluster of darker nuclei that are concentrated in the center. The main characteristic for necrotic tissue is the faded color of the nuclei and pale regions throughout the image.

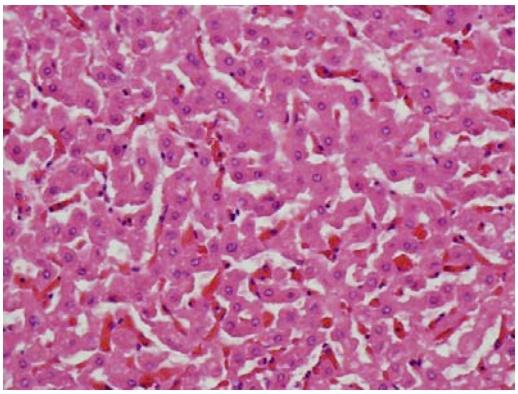

Figure 3: Healthy Liver Tissue

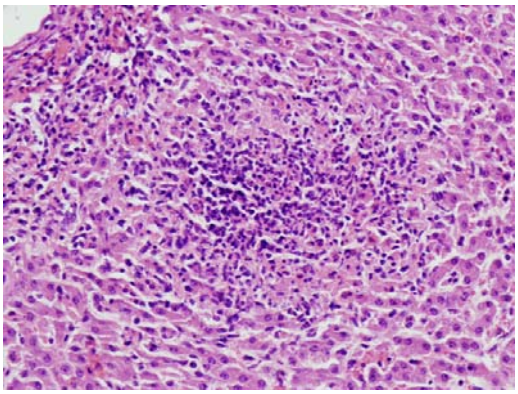

Figure 4: Inflammatory Liver Tissue

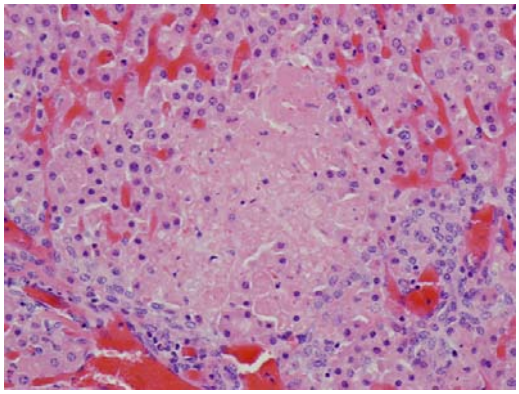

Figure 5: Necrotic Liver Tissue

Kidney Photomicrographs

Kidney photomicrographs exhibit similar conditions to the healthy and inflammatory conditions for liver tissue described in the previous subsection. The healthy kidney tissue exhibits uniform nuclei distributions throughout the image, whereas the inflammatory kidney tissues have a tendency for nuclei to be clustered in the center of the image.

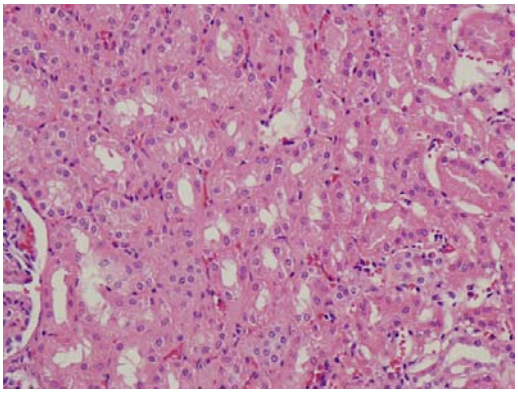

Figure 6: Healthy Kidney Tissue

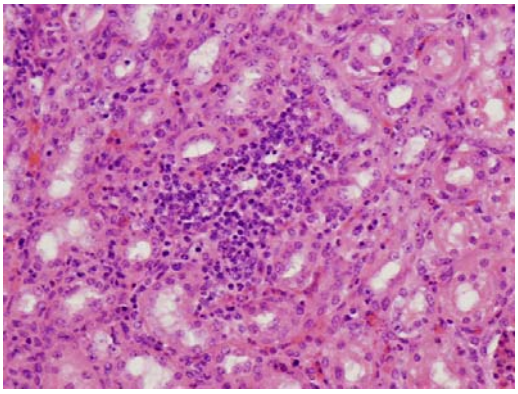

Figure 7: Inflammatory Kidney Tissue

Spleen photomicrographs

Lastly, spleen photomicrographs are shown in Figures 9 and 10. We note that spleen tissues do not exhibit a significant difference in distribution of the nuclei in the image as the other organs. However, there are certain areas in the images that reflect the tissue condition by some regions that having paler portions of pink regions. By using the multispectral channels for classification, we expect to exploit this characteristic in our simulation.

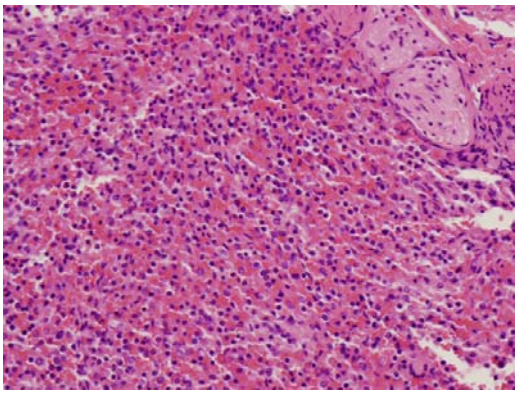

Figure 8: Healthy Spleen Tissue

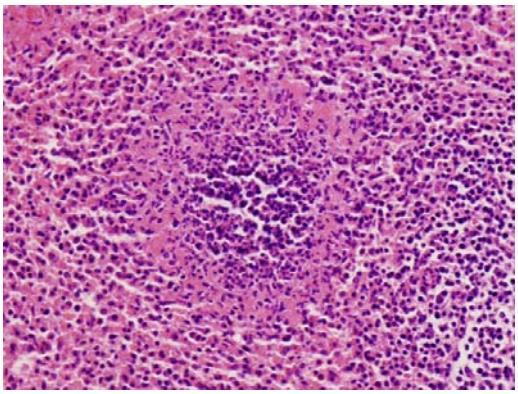

Figure 9: Inflammatory Spleen Tissue

Experimental Results

There are 50 images per class per organ with the exception of liver, for which only 25 images per class were provided. From the set of 50 images for each class of lung, kidney, and spleen, a subset of 45 training dictionary images were randomly selected. After combining the two dictionaries, we randomly chose a test image from the remaining images to test the performance of our algorithm. For liver, a subset of 20 images for each conditions, healthy, inflammatory, and necrotic, were randomly selected. Similarly, after combining the three dictionaries, we randomly chose a test image from the remaining set and performed classification. To expedite classification process, the images were downsampled to 100×75. The process was repeated for 1000 trials for each class of the test image to remove any possible bias. The sparsity level was varied to observe the effects in the process. We compute the recognition rates for four approaches explained below in Table 2.

Table 2: Explanation of Simulation Methods

Approach	Explanation
Grayscale	Grayscale S-OMP Output
Color – Uniform Weight	Color S-OMP with $w(c) = 1/3 \; \forall c$
Color – Weighted Sum	Color S-OMP with $w(c)$ based on color channel energy
Color – Auxiliary Output	Color – Weighted Sum with auxiliary problem

The classification results are shown in Figure 10 and 11. We first note that with $K = 2$, which corresponds to less than 5% of the number of atoms, we have poor results, as all of the recognition rates are near 0% or 100%. This can be interpreted as the initial bias resulting from our dictionary. Since S-OMP picks the index that best approximates all the residuals, this bias is mitigated by increasing the number of atoms in the classification process, which is evident as we increase the number of atoms K. Note that with $K = 20$, we are using 20% and 33% of dictionary elements for non-liver and liver tissues respectively, which still is considered sparse. For further analysis, we proceed with $K = 20$. The confusion matrices for the corresponding organs are shown in Tables 3 through 6.

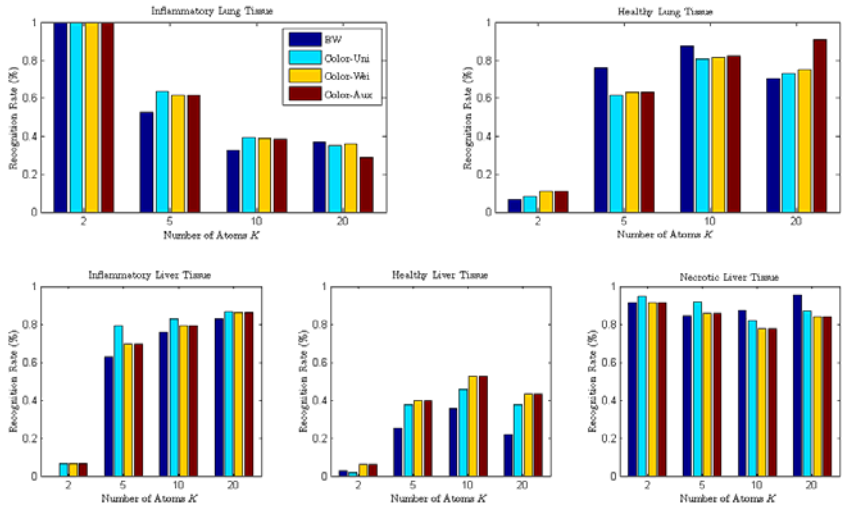

Figure 10: Classification Results for Lung and Liver Tissue

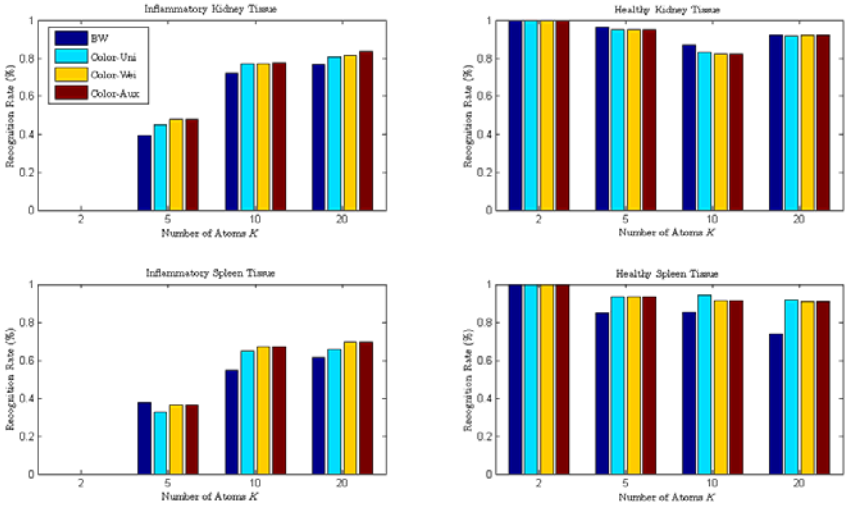

Figure 11: Classification Results for Kidney and Spleen Tissue

Table 3: Confusion Matrix: Lung

Class	Healthy	Inflam.	Method
Healthy	0.706	0.294	Grayscale
	0.910	**0.090**	**Color-Aux**
Inflam.	**0.634**	**0.366**	**Grayscale**
	0.714	0.286	Color-Aux

Table 4: Confusion Matrix: Liver

Class	Healthy	Inflam.	Necro.	Method
Healthy	0.218			Grayscale
	0.431			**Color-Aux**
Inflam.		0.828		Grayscale
		0.861		**Color-Aux**
Necro.			**0.955**	**Grayscale**
			0.841	Color-Aux

Table 5: Confusion Matrix: Kidney

Class	Healthy	Inflam.	Method
Healthy	**0.922**	**0.078**	**Grayscale**
	0.920	0.080	Color-Aux
Inflam.	0.233	0.767	Grayscale
	0.163	**0.837**	**Color-Aux**

Table 6: Confusion Matrix: Spleen

Class	Healthy	Inflam.	Method
Healthy	0.739	0.261	Grayscale
	0.908	**0.092**	**Color-Aux**
Inflam.	0.385	0.615	Grayscale
	0.306	**0.694**	**Color-Aux**

Now, let us consider only the outputs from color output from the auxiliary problem and grayscale classification. The recognition rate for these two methodologies is shown below in Figure 12 along with each classification's 95% confidence interval. Note that we use Clopper-Pearson method to generate the confidence interval [23]. Clearly, the classification method using color channel has higher recognition rate than using grayscale images. The difference is mostly reflected on classification of spleen, where the classes did not exhibit differences in nuclei distribution. Clearly, the performance difference between the two methods shows the advantages of exploiting color information. With the exception of lung, classification using color channels provide a better performance than uniform guessing (1/2 for binary classification, 1/3 for ternary classification).

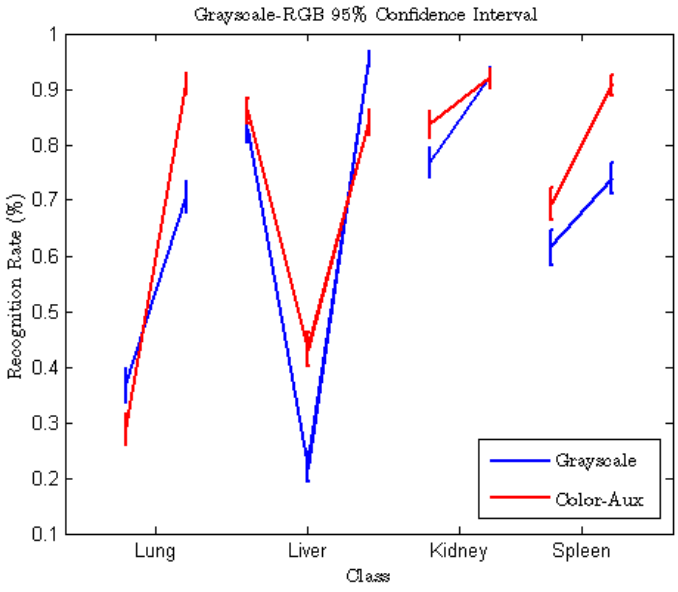

Figure 12: 95% Confidence Interval for Grayscale and Color – Aux

Lastly, we compare the recognition rates from our color output with the rate obtained by a classification method of using feature extraction and support vector machine (SVM) [24]. The recognition rate with the corresponding 95% confidence interval is shown below in Figure 13. While feature extraction method dominates our method most of the time, we observe that our method does better for kidney tissues. This may result from the fact that kidney tissues have a more uniform structure than other organ tissues. Since our methodology is a form of example-based learning, we would expect better results with better dictionary elements.

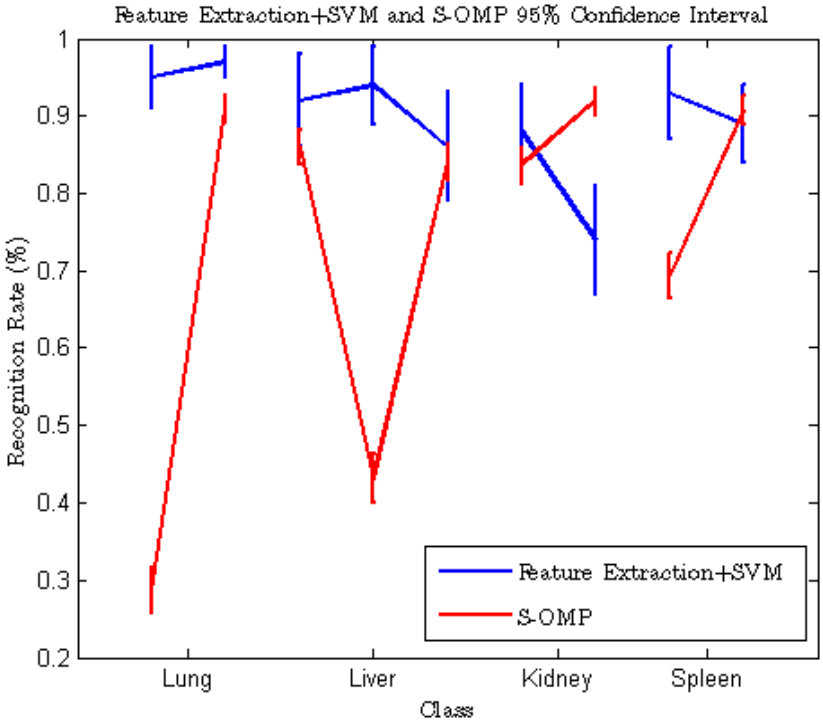

Figure 13: 95% Confidence Interval for Feature Extraction and S-OMP

CONCLUSION

The classification approach introduced in this paper utilizes multispectral channels for a sparsity model to classify images. To adopt the original grayscale sparsity model proposed in [9] to color images, we extend the joint sparsity model suggested in [10]. Then, since the original problem was non-convex, we use a matching pursuit algorithm (S-OMP) to approximate the problem. The initially obtained $\boldsymbol{S}$ from S-OMP was improved by solving an additional optimization problem that enforces positivity while guaranteeing sparsity. The reconstruction parameters were then used to calculate the residual norm for each of the different classes. Finally, the class with minimum residual was chosen.

For testing purposes, we use bovine organ database provided by the Pennsylvania State University Animal Diagnostic Laboratory. For every organ and class, subsets of the images were chosen to be training samples that would be the dictionary of our model. Then, a test image was selected and our algorithm performed classification. Our model tested for $N = 1000$ trials. The recognition rate was higher for using color channels than grayscale by exploiting additional information. The difference was mostly noticeable where the deterministic information for classification was present in the color channels, not the overall structure of the image. Lastly, our performance was compared with classification with feature extraction and support vector machine obtained from [24]. While our algorithm showed better performance for the recognition rate of kidney tissue, feature extraction/SVM method dominated for the other organ tissues. This suggests the importance of processing the images by using feature extraction or contrast agents in medical imaging. While for histopathological images our algorithm does not show a robust performance, using multispectral channel does reflect a stronger performance than single channel.

Suggestions for Future Work

Our model formulation was an approach to adapt the grayscale sparsity model to multispectral channels. Although different methods using PCA/ICA have been already developed, we concentrate on sparse model framework. Since the Hadamard operator from $\boldsymbol{S}$ to $\boldsymbol{S}'$ in Equation (9) imposes a complexity in using previous methods for solving sparse problems, further work to relax the operator is suggested. Also, instead of using S-OMP, other approximation methods could be used to show the performance in multichannel operations.

For the histopathological image classification, possibilities for future improvements are suggested. Since the performance of S-OMP is depended upon the strength of the dictionary, diverse images would be needed to ensure sufficiently high recognition rate. In the case of medical imaging, where low Type I error is essential, this may require thousands of images. Also, the analysis of performance gain of using preprocessed medical images by feature extraction or contrast agents in dictionary with sparse models is suggested.

ACKNOWLEDGMENTS

I would first like to thank Professor Vishal Monga and Umamahesh Srinivas for the helpful discussion and assistance with the project. Also, I would like to thank the EEREU program, at Pennsylvania State University for giving me the opportunity to participate in research. Furthermore, I would like to give great thanks to Professors Saleem Kassam and Santosh Venkatesh at Penn for assisting my studies. Lastly, I would like to acknowledge Mu Li and Bosung Kang for making my experience at Information Processing and Algorithms Lab (iPAL) and Pennsylvania State University memorable. This material is based upon work supported by the National Science Foundation under Grant No. EEC-1062984.

APPENDIX

Problem 1: The unique solution $\boldsymbol{s}_c^*$ for the optimization problem in Equation (12) is given as

$$\boldsymbol{s}_c^* = -\boldsymbol{H}_c^{-1}\left(\boldsymbol{c}_c - \boldsymbol{e}_c\lambda\right)$$

where $\boldsymbol{H}_c = \boldsymbol{A}_c^T\boldsymbol{A}_c$, $\boldsymbol{c}_c = -\boldsymbol{A}_c^T\boldsymbol{x}_c$, and $\lambda = \left(\boldsymbol{e}_c^T\boldsymbol{H}_c^{-1}\boldsymbol{e}_c\right)^{-1}\boldsymbol{e}_c^T\boldsymbol{H}_c^{-1}\boldsymbol{c}_c$.

Proof: The proof is based from an example in [25]. We start by examining the quadratic programming problem

$$\begin{aligned} \text{minimize} \quad & \frac{1}{2}\|x\|^2 + c^T x \\ \text{subject to} \quad & Ax = 0 \end{aligned}$$

where $c \in \mathbb{R}^n$ and A is an $m \times n$ matrix of rank m. Since adding a constant term $\frac{1}{2}\|c\|^2$ does not affect our cost function, we rewrite this problem as

$$\begin{aligned} \text{minimize} \quad & \frac{1}{2}\|c + x\|^2 \\ \text{subject to} \quad & Ax = 0 \end{aligned}$$

which is a projection of the vector $-c$ onto the subspace $X = \{x|Ax = 0\}$. It can be seen that the unique solution to the problem above is given as the orthogonal projector of the vector:

$$x^* = -\left(I - A^T\left(AA^T\right)^{-1}A\right)c \tag{15}$$

With the orthogonal projector ready, consider a more general quadratic program

$$\begin{aligned} \text{minimize} \quad & \frac{1}{2}x^T Hx + c^T x \\ \text{subject to} \quad & Ax = 0 \end{aligned} \tag{16}$$

where H is a positive definite symmetric matrix. By introducing the vector $y = H^{1/2}x$, we transform this problem to

$$\begin{aligned} \text{minimize} \quad & \frac{1}{2}\|y\|^2 + \left(H^{-1/2}c\right)^T y \\ \text{subject to} \quad & AH^{-1/2}y = 0 \end{aligned}$$

Using Equation (15) the solution of this problem is

$$y^* = -\left(I - H^{-1/2}A^T\left(AH^{-1}A^T\right)^{-1}AH^{-1/2}\right)H^{-1/2}c$$

thus by passing through the transformation $x^* = H^{-1/2}y^*$, the optimal solution of problem of Equation (16) is given as

$$x^* = -H^{-1}\left(c - A^T\lambda\right)$$

where λ is given by

$$\lambda = \left(AH^{-1}A^T\right)^{-1}AH^{-1}c$$

REFERENCES

[1] A. V. Oppenheim and R. W. Schafer, *Discrete-time signal processing*; 3rd ed. Upper Saddle River, NJ: Pearson, 2010.

[2] D. L. Donoho, "Compressed sensing," *IEEE Trans. Inf. Theory*, vol. 52, no. 4, pp. 1289–1306, 2006.

[3] E. J. Candès, J. K. Romberg, and T. Tao, "Robust uncertainty principles: exact signal reconstruction from highly incomplete frequency information," *IEEE Trans. Inf. Theory*, vol. 52, no. 2, pp. 489–509, 2006.

[4] C. Christopoulos, A. Skodras, and T. Ebrahimi, "The JPEG2000 still image coding system: an overview," *IEEE Trans. Consum. Electron.*, vol. 46, no. 4, pp. 1103 –1127, Nov. 2000.

[5] R. Basri and D. Jacobs, "Lambertian reflectance and linear subspaces," *IEEE Trans. Pattern Anal. Mach. Intell.*, vol. 25, no. 2, pp. 218 – 233, Feb. 2003.

[6] J. Mairal, M. Elad, and G. Sapiro, "Sparse representation for color image restoration," *IEEE Trans. Image Process.*, vol. 17, no. 1, pp. 53 –69, Jan. 2008.

[7] J. Yang, J. Wright, T. Huang, and Y. Ma, "Image super-resolution as sparse representation of raw image patches," in *Proc. IEEE Conf. CVPR*, Jun. 2008, pp. 1 –8.

[8] H. Zhang, N. M. Nasrabadi, T. S. Huang, and Y. Zhang, "Joint sparse representation based automatic target recognition in SAR images," vol. 8051, no. 1. *Proc. SPIE*, 2011, p. 805112.

[9] J. Wright, A. Y. Yang, A. Ganesh, S. S. Sastry, and Y. Ma, "Robust face recognition via sparse representation," *IEEE Trans. Pattern Anal. Mach. Intell.*, vol. 31, no. 2, pp. 210–227, 2009.

[10] Y. Chen, N. M. Nasrabadi, and T. D. Tran, "Hyperspectral image classification using dictionary-based sparse representation," *IEEE Trans. Geosci. Remote Sens.*, vol. 49, no. 10, pp. 3973–3985, 2011.

[11] R.-L. Hsu, M. Abdel-Mottaleb, and A. Jain, "Face detection in color images," *IEEE Trans. Pattern Anal. Mach. Intell.*, vol. 24, no. 5, pp. 696 –706, May 2002.

[12] I. El-Naqa, Y. Yang, M. N. Wernick, N. P. Galatsanos, and R. M. Nishikawa, "A support vector machine approach for detection of microcalcifications," *IEEE Trans. Med. Imag.*, vol. 21, no. 11, pp. 1552–1563, 2002.

[13] S. Bloch, P. Dayton, and K. Ferrara, "Targeted imaging using ultrasound contrast agents," *IEEE Eng. Med. Biol. Mag.*, vol. 23, no. 5, pp. 18 – 29, Sept.-Oct. 2004.

[14] A. Jain, R. Duin, and J. Mao, "Statistical pattern recognition: a review," *IEEE Trans. Pattern Anal. Mach. Intell.*, vol. 22, no. 1, pp. 4 –37, Jan. 2000.

[15] J. Tropp and S. Wright, "Computational methods for sparse solution of linear inverse problems," *Proc. IEEE*, vol. 98, no. 6, pp. 948 –958, Jun. 2010.

[16] D. L. Donoho, "For most large underdetermined systems of linear equations the minimal l1-norm solution is also the sparsest solution," *Comm. Pure Appl. Math*, vol. 59, pp. 797–829, 2004.

[17] E. J. Candès and T. Tao, "Near-optimal signal recovery from random projections: Universal encoding strategies?" *IEEE Trans. Inf. Theory*, vol. 52, no. 12, pp. 5406–5425, 2006.

[18] E. J. Candès, J. K. Romberg, and T. Tao, "Stable signal recovery from incomplete and inaccurate measurements," *Comm. Pure Appl. Math*, vol. 59, no. 8, pp. 1207–1223, 2006.

[19] J. A. Tropp, A. C. Gilbert, and M. J. Strauss, “Algorithms for simultaneous sparse approximation. Part i: Greedy pursuit,” *Signal Processing*, vol. 86, no. 3, pp. 572–588, 2006.
[20] J. A. Tropp, “Algorithms for simultaneous sparse approximation. part ii: Convex relaxation,” *Signal Processing*, vol. 86, no. 3, pp. 589–602, 2006.
[21] S. Cotter, B. Rao, K. Engan, and K. Kreutz-Delgado, “Sparse solutions to linear inverse problems with multiple measurement vectors,” *IEEE Trans. Signal Process.*, vol. 53, no. 7, pp. 2477 – 2488, Jul. 2005.
[22] E. van den Berg and M. P. Friedlander, “Joint-sparse recovery from multiple measurements,” *CoRR*, vol. abs/0904.2051, 2009.
[23] H. Blaker, “Confidence curves and improved exact confidence intervals for discrete distributions,” *The Canadian Journal of Statistics*, vol. 28, no. 4, pp. pp. 783–798, 2000.
[24] J. Gillespie, “Automated classification of histopathological images,” Bachelor Thesis, The Pennsylvania State University, Schreyer Honors College, May 2012.
[25] D. P. Bertsekas and D. P. Bertsekas, *Nonlinear Programming*, 2nd ed. Athena Scientific, 1999.

THERE AND BACK AGAIN—LUNAR ROBOTIC LAUNCH AND LANDING SYSTEM

François M. Rice* and John Mathews[#]

Department of Electrical Engineering
The Pennsylvania State University, University Park, PA 16802

*Undergraduate Student of
Department of Electrical & Computer Engineering
University of Maryland, Baltimore County
Baltimore, MD 20785

ABSTRACT

A rail-gun system on the Moon would have the capabilities needed in order to launch a spacecraft into orbit without needing a chemical rocket. A chemical rocket propelled at the speed needed to reach orbit and/or escape the Moon's gravitational field is inefficient. As solar energy is "free" on the Moon but chemical fuel is expensive, we explore electromagnetic methods for launching satellites to low lunar orbit (LLO). Robotic systems launched from the Earth to the Moon would have the ability to autonomously build rail-gun systems on the Moon for launch—and perhaps capture—of small space vehicles. This paper will go into the characteristics of lunar orbit as well as the launch and capture energetics, the amount of energy needed, for the launch. The use of rail-guns that is explained here would have many benefits such as cost effectiveness and low lunar environmental impact as compared to other traditional propulsion systems that require manufacture of chemical fuels. The necessary political and social considerations are also discussed in this paper.

INTRODUCTION

Launching an orbital vehicle (OV) into space has always been extremely challenging. Around all objects in the universe there are "gravity wells", which are the gravitational pull of the bodies. The more massive the body is, the larger and stronger the gravity well will be. Because of the Earth's larger mass, it has a huge gravity well, relative to, e.g., the Moon, that takes a tremendous amount of energy to overcome. Along with Earth's gravitational pull, there is also an atmosphere around the Earth. The atmosphere frictionally resists anything that

[#] Faculty Mentor

moves through it, including objects being launched into space, or that are in orbit around the Earth. Because of these two factors, OVs must first be launched upward. This is both to get out of the lower atmosphere, which is exponentially denser at lower altitudes, and also to rise out of Earth's gravity well. Once the atmosphere no longer interferes with the OV's movement, the OV can reach the speed needed to obtain orbit. Unfortunately, to get out of the atmosphere, the OV has already used a large amount of its fuel, which leads to the high cost of orbital missions. If one were to take the atmosphere and the depth of Earth's gravity well out of the equation, an OV could easily achieve an orbit from any height. On Earth this is impossible for obvious reasons. However, on the Moon, this is the exact case. The atmosphere that usually makes orbital launch so difficult from the Earth is non-existent on the Moon. The Earth is also almost 100 times more massive than the Moon, meaning that the Moon's gravitational pull is about six times weaker than the gravitational pull on the Earth. The Moon's radius is ~0.273 the radius of the Earth.

Because of the Moon's smaller gravity well and lack of atmosphere, it would be beneficial to have a station on the Moon that could launch OVs into Earth's orbit, for specific missions, or deeper into the solar system, for exploration. To launch an OV into a low lunar orbital path from the surface of the Moon would require a final launch speed greater than 1.6 km/s. This speed can be achieved without the use of chemical propellant by employing current magnetic levitation technology. Using a similar technology that the United States Navy uses to arm battleships with rail-guns, an OV could be launched into space solely by use of electricity. Another advantage of the Moon not having an atmosphere is that there is nothing to block the rays of the sun from shining fully on the Moon's surface. Therefore, the sun's thermal energy could be captured and used in order to power and operate the magnetic rail launcher. This magnetic rail station would be built autonomously by robots sent to the Moon. From there the station would be built using the metal oxides found in the soil on the surface of the Moon. Through this method, resources taken from Earth would be minimized. Payload weight would also be decreased without the need for materials or personnel. In order to transport these robots to the Moon and build this station, a method must first be implemented to transport them to the lunar surface. Some methods are discussed in detail later.

EXPERIMENT DESCRIPTION

Orbital Mechanics

To begin the design of the magnetic rail system, the orbital requirements of the launched OV must first be solved. To analyze this, the first equation to start with is Newton's gravitational equation:

$$\vec{F} = \frac{GMm}{r^2}, \tag{1}$$

where G is the gravitational constant (6.67×10^{-11} Nm^2/kg^2), M is mass of the Moon (7.36×10^{22} kg), r is radius of the Moon (1.7374×10^{6} m), and m is mass of the OV (kg). If the OV follows a circular path around the Moon and it is assumed that the Moon is a perfect sphere, then:

$$a_{rad} = \frac{\vec{F}}{m} = \frac{GM}{r^2}, \tag{2}$$

where a_{rad} is radial acceleration of the OV (m/s^2).

$$a_{rad} = \frac{v^2}{r}, \tag{3}$$

where v is the velocity of the OV (m/s). Because we are assuming a circular orbit, the values can be determined as scalar quantities, and not as vectors. Combining these two equations gives a third equation:

$$v = \sqrt{\frac{GM}{r}}\,. \tag{4}$$

Using Equation (4), it is possible to find the necessary speed that an OV needs to obtain a circular orbit around the Moon, at a given height. Assuming that an OV is following a circular orbit at the surface of the (circular, homogenous) Moon, the necessary speed of the OV would be 1681.5 m/s. Using the same equation to find the velocity necessary for an OV to obtain a circular orbit at 10 km above the surface of the Moon yields a value of 1676.7 m/s. In order to connect these two orbits, a Hofmann transfer orbit must be established. To obtain a Hofmann transfer orbit a change of velocity must be applied to the OV. This change in velocity will produce an elliptical orbit. A change in velocity must also be applied to the OV once it reaches the apolune (apsis of a lunar orbit) point of elliptical transfer orbit. The point of apolune is the point at which the OV would be farthest away from the Moon in its orbit. To determine the speed at apolune and perilune of the transfer orbit it is necessary to use Kepler's 2nd Law, which states that an object in orbit sweeps equal amounts of area for equal times. Therefore:

$$\dot{\theta} r^2 = \text{constant}\,. \tag{5}$$

For an elliptical orbit, if an object has velocity v_a (m/s) and radius r_a (m) at apogee and velocity v_p (m/s) and radius r_p (m) at perigee and the angle between the radius and the velocity is β (rads), then the following equation is true:

$$v \sin\beta = \dot{\theta} r\,. \tag{6}$$

Multiplying Equation (6) by a factor of r, and combining it with Equation (5) gives:

$$rv\sin\beta = \dot{\theta}r^2 = \text{constant}. \tag{7}$$

At perilune and apolune β is always equal to π radians. Because of Equation (7) and this fact, it is now proven that:

$$r_p v_p = r_a v_a. \tag{8}$$

If the conservation of energy theorem is applied to Equation (8), the result equation would be:

$$\frac{1}{2}mv_p^2 - \frac{GMm}{r_p} = \frac{1}{2}mv_a^2 - \frac{GMm}{r_a}. \tag{9}$$

This equation can now be separated algebraically, for the new equation:

$$v_p^2 - v_a^2 = 2GM\left(\frac{1}{r_p} - \frac{1}{r_a}\right). \tag{10}$$

It is now possible to solve for v_p and v_a to find the necessary velocities at apolune and perilune that an OV would need to achieve:

$$v_p = \sqrt{\frac{2GMr_a}{r_p(r_a + r_p)}}, \tag{11}$$

$$v_a = \sqrt{\frac{2GMr_p}{r_a(r_a + r_p)}}. \tag{12}$$

These two equations can also be written using the length of the semi-major axis of the ellipse. The semi-major axis is the ellipse's average radius around a central point

$$a_t = \frac{r_a + r_p}{2}, \tag{13}$$

where a_t is length of the semi-major axis [m]. This variable can now be substituted into Equation (11) and (12) to obtain:

$$v_p = \sqrt{GM(\frac{2}{r_p} - \frac{1}{a_t})}, \quad (14)$$

$$v_a = \sqrt{GM(\frac{2}{r_a} - \frac{1}{a_t})}. \quad (15)$$

Using Equation (4) along with Equations (14) and (15), it is possible to find the velocity needed to achieve a circular orbit at 10 km above the Moon's surface, and the changes in velocity that would be needed to achieve the elliptical Hofmann transfer orbit. At the perilune in the elliptical orbit the OV would need to achieve a velocity of 1683.9 m/s, and at apolune the OV would have a velocity of 1674.3 m/s. The magnetic rails would launch an OV along the elliptical transfer orbit path at 1684 m/s to achieve the elliptical transfer orbit. Once the OV reached its apolune point, another type of propellant would be used to achieve the 1676.7 m/s needed a 10 km circular orbit. To follow the elliptical orbit path, the rails would be to have a curvature and height resembling Figure 1.

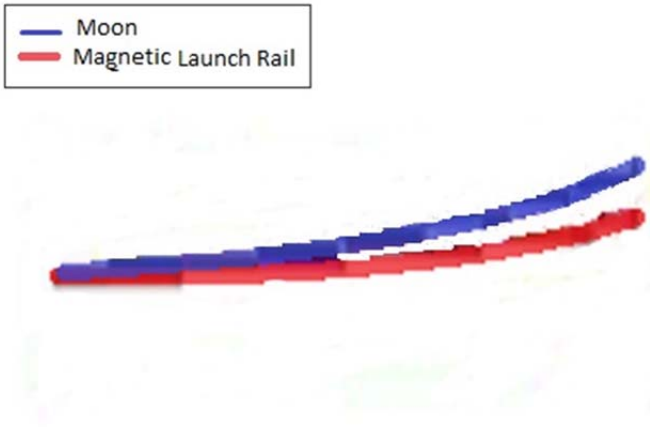

Figure 1: The curve of the magnetic rail around the Moon

System

The second factor to consider in the design of the magnetic rail station is the system that will be used by the rail and how the system will work. The magnetic rail system proposed would work almost the exact same way that a Naval Rail-gun would work. Two conductive rails would be placed with a conductive armature in between them. A current would be created up one of the rails, across the armature, and back down the other rail. This current would also generate a magnetic field around the rails and armature, which would act perpendicular to

the current according to Zahn [1]. Therefore, the resulting magnetic field would point in an upward direction. The magnitude of the magnetic field is a function of the current generated. The presence of both a magnetic field and a current creates a Lorentz force, which is perpendicular to both the current and the magnetic field. Being perpendicular to both the lateral current and an upward magnetic field forces the Lorentz force in an outward or forward direction. This Lorentz force is the force that moves the armature along the rails. The Lorentz force generated is determined by the equations:

$$\vec{F} = (\vec{I} \times \vec{B})\vec{L}, \tag{16}$$

where $\vec{F}$ is force (N), I is current (A), B is magnetic field (tesla), and L is length of the armature (m). When looking at these variables as scalar values, the vector notation can be removed. The Lorentz force acts upon each individual charge within a conductor. Because of this reason, the longer the armature, the greater the number of charges, the more the Lorentz force can act upon the armature, and the stronger the Lorentz force on the entire armature.

$$B = \frac{\mu_0 I}{2\pi r}, \tag{17}$$

where μ_0 is a constant of value $4\pi \times 10^{-7}$ (Tesla × m/A), r is the distance from the center of the magnetic field (m). Both Equations (16) and (17) are derived in Markus Zahn's textbook [1]. These equations are also found in Hambley [2]. Because the magnetic field generated in the rails is dependent on the current flowing through the rails, equation (16) can be rewritten as:

$$F = \frac{\mu_0 I^2 L}{2\pi r}. \tag{18}$$

Because μ_0 and 2π are both constants, they can be combined into a constant k with a value of 2×10^{-7}. The entire armature is acting as a conductor carrying in the current. Because the OV is going to be on or attached to the armature, the distance from the current within the armature to the OV becomes arbitrarily small, and can be neglected. This equation then can be written as:

$$F = kI^2 L, \tag{19}$$

$$a = \frac{F}{m} = \frac{kI^2 L}{m}. \tag{20}$$

This equation is used to calculate the necessary force needed to generate a constant 5 gee acceleration (49.05 m/s^2) for any OV. Because a constant acceleration is being applied to the OV, basic kinematics can be used to find the minimum distance needed for acceleration and the time required for launch. Using the kinematic equations:

$$v_f = v_0 + at, \tag{21}$$

where v_f is the final velocity at perigee (1684 m/s), v_0 is the initial velocity of the OV (0 m/s, starting from rest), and a is the acceleration set at a constant 5 g's (49.05 m/s^2). Using these values, the calculated time needed to launch the OV along the track would be 34.3 seconds. Using this value, the distance that the OV would need to travel in order to launch can also be found using the following equation:

$$x_f = x_0 + v_0 t + \frac{1}{2} a t^2, \tag{22}$$

where x_0 is the initial distance the OV has travelled (0 m), and x_f is the distance that the OV needs to travel. Using this equation and the values from Equation (21), the calculated distance that the OV would need to travel and the minimum length of the rail would need to be 28.9 km.

Energetics

The physics for the motion of the armature and the OV has been solved, but it is also necessary to solve for the amount of energy that would be required in order to operate a magnetic rail station of this magnitude. To analyze the energy consumption of this system, it is necessary to look at the equation for electric Power and the definition of power:

$$P = IV, \tag{23}$$

where P is power (W), I is current (A), and V is voltage (V). After Equation (23), the equation that needs to be used is the definition of power, which is:

$$P = \frac{E}{t}, \tag{24}$$

where E is energy (J) and t is time (seconds). Equation (23), according to Hambley [2], is the equation used to relate an electrical current to the amount of power, or energy in a given time, that that current uses. Equation (24) is the definition of power, which is the amount of energy used over a given time period. Combining these two equations, will yield:

$$E = IVt\ . \tag{25}$$

Although, this equation now relates any current to the amount of energy required for that current, the unit of voltage is can be further simplified. This is because voltage is a function of both current and resistance.

$$V = IR, \tag{26}$$

$$E = I^2 Rt\ . \tag{27}$$

Combining Ohm's Law, Equation (26), and Equation (25) a new equation can be created that relates energy, current, resistance, and time. This is significant because of the nature of the Moon's surface. Because the surface has no atmosphere, it is not able to hold any heat from the sun. This lack of heat makes the surface of the Moon a perfect environment for superconductive materials. A superconductive material, or superconductor, is a material that as its temperature decreases; the resistance of that material also decreases until the resistance becomes zero [3]. At this point a current would be able to flow through this material for an indeterminate amount of time. Because the use of zero as the resistance would make energy calculations impossible, the energy used cannot be determined using this method. As an alternative, the energy need for launch can be calculated using the law of conservation of energy. Because the OV is gaining kinetic energy as it is being launched, the energy needed for launch can be calculated as:

$$\mathrm{KE} = \frac{1}{2} mv^2\ . \tag{28}$$

Using this equation and the values for the OV to achieve the speed needed for perilune of the transfer orbit, the calculated energy that would be needed would be 1,417,928 J/kg. This is approximately one-half of a kilowatt-hour. This is a surprisingly low value in comparison to the necessary velocities that would need to be achieved. The average cost of a kilowatt-hour is approximately $0.10 [5].

Achieving a Circular Orbit

Once the magnetic rail system launches the OV into an elliptical Hofmann orbit, the OV will continue to orbit in the shape of an ellipse unless it gains enough velocity at the orbits apolune to achieve a circular orbit. For the OV to achieve a circular orbit at 10 km above the lunar surface after being launched from the magnetic rail, the OV would need to increase its velocity by 2.4 m/s. This could easily be obtained by ejecting a mass off the OV using a spring. Using the law of conservation of momentum:

$$(m_1 + m_2)v = m_1 v_1 + m_2 v_2, \tag{29}$$

where m_1 is the mass of the OV, m_2 is mass being ejected, v is speed of OV at apolune, v_1 is the speed of the OV after ejecting the lunar dust, and v_2 is the speed of the lunar dust after being ejected. Assuming that the equation is relative to the speed at apolune, v is equal to zero. v_1 also becomes 2.4 m/s. If the mass projected is always $1/10^{th}$ of the overall OV, the equation then becomes:

$$2.4m_1 = -\left(\frac{m_1}{10}\right)v_2 . \tag{30}$$

Using this equation, v_2 is found to be 24 m/s less that the speed at apolune. The energy required for this can be calculated using Equation (28). The energy required using this calculation is 28.8 J. This value is minuscule in comparison to the energy needed by the magnetic rails. The lunar dust would also fall back to the surface and resettle.

RESULTS

As discussed previously in this paper there are several major benefits to having a lunar launch/landing base on the Moon, some if these benefits being cheaper launch costs, lack of atmosphere, weaker gravitational pull, free energy, and a launch without the use of chemicals.

Cheaper Launch

The biggest reason to establish a base on the Moon for launching OVs is to cut down on the cost of launches and, thus, to mitigate the environmental downside of launches from Earth. Currently, the cost of a launch into LEO is approximately $30,000 per kilogram, according to Parkinson [4]. Most of this cost is due to the chemical propellant that is needed to launch an OV fast enough to obtain orbit. This speed can be obtained more effectively and more inexpensively with the use of electrical rails. The system previously explained for the Moon would be able to launch an OV for approximately $0.10/kg according to average costs of energy [5]. This is assuming that processes on the Moon used to generate energy would be similar to those currently employed to generate energy on Earth. If solar power is used as the primary source of acquiring energy, then cost per kilogram of material launched would decrease even further.

Free Energy and Commercial Profit

The Moon has many resources that could be utilized by the Earth and those who seek to make a profit through commercial space transport. According to Wingo [6], the soil of the Moon is rich with metallic oxides. Iron has the highest concentration compared to any other metal found on the Moon. This iron would serve as a vital building material in establishing lunar bases, or for export back to Earth. Another resource that is said to cover the Moon's surface is Helium-3. This

resource is blown onto the surface of the Moon by solar winds, from the sun, and because the Moon has no atmosphere, the element is able to settle on the Moon's surface. Helium-3 is a key element in nuclear fusion and could be used on Earth as a potent energy source. This gives greater importance to the resources of the Moon, as the Earth is nearing an energy crisis. With the depletion of oil and estimates that reserves will be emptied in two to three decades, society needs other viable sources of fuel. One such source is fuel cells. Fuels cells are similar to batteries in that they create energy potential and produce current. One of the key components in a fuel cell is platinum. Unfortunately, platinum is one of the rarest metals on Earth, making it very expensive and very limited. According to Wingo [6] there are likely many deposits of platinum on the Moon. In addition, launching from the Moon to near Earth asteroids (NEA) could harvest additional sources of platinum. Missions to the Moon would be able to establish autonomous mining facilities in order to harvest these resources. The resources would then be sent back to Earth through the use of the magnetic rail system. The Moon's mining potential makes it a viable subject for commercial operations. These commercial operations could also be done more inexpensively through the use of a magnetic rail system instead of solely by chemical propellant.

A magnetic rail system on the Moon would also utilize the natural sunlight that the Moon receives. If solar cell arrays (and mirror-based solar concentrators) are placed on the poles of the Moon they would be able to capture the Sun's light at all times and constantly power the magnetic rail system and robotics "base". There would also need to be batteries, and other alternatives such as fly-wheels, along with the solar cells to capture excess energy when the rails are not being used. The solar cells would be placed on a higher elevation to capture more of the sunlight from the sun. From the raised elevation the solar cells would need to be connected to the main station with the magnetic rail. The magnetic rail system would ideally be within a crater where sunlight is less likely to reach it. According to planetfacts.org [14], the surface temperature of the Moon, when the surface is not receiving direct sunlight, is 120 K. There are several materials that have superconductive properties at this temperature. There are also craters that never receive sunlight, which would keep the rails at this ideal temperature. If the magnetic rail system were stationed in the crater, the rails would be easier to keep at critical temperatures and would retain superconductivity. According to NASA photos [7], there are a large number of craters both in the northern and southern pole of the Moon, with the North Pole having the greatest concentration of craters. An example of these craters is shown in Figure 2. This image was taken from NASA's lunar prospector mission website.

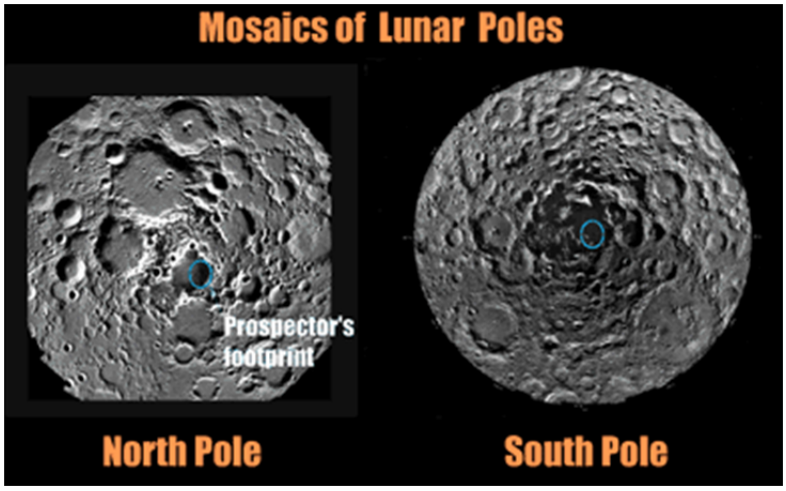

Figure 2: Photos of the Moon's poles [7]

Reduced Use of Propellant Fuel

With the use of the magnetic rails, the need for chemical propellant would be greatly reduced. As stated previously, this would cut down on costs. A secondary benefit of reduced propellant use is the prevention of pollutants being produced around the Moon. Though, the Moon lacks an atmosphere, these gases may give rise to serious problems in the future, if space travel to and from the Moon becomes more commonplace.

Removal of Space Debris and Near Earth Asteroids (NEA)

Orbital debris (OD) in the Earth's atmosphere is a growing problem. NASA reports [17] that there are currently 21,000 objects in orbit larger than 10 cm. There are also 500,000 particles between 1cm and 10 cm, and over 100 million particles smaller than a cm. These objects are all classified as OD, meaning that they are man-made objects that no longer serve any purpose. Though most particles of OD are small, the particles travel with speed ranging from 7 to 10 km/s. The particles are able to release a high amount of energy because of this speed. The International Space Station, the most heavily shielded spacecraft ever flown [17], can with stand collision against OD smaller than 1 cm. For all larger particles, the Space Station must change its trajectory to avoid collision with the particle. The amount of OD increases with continued launch of OV. Depending of the height of OD in the atmosphere, it can take decades or centuries for OD to burn in the atmosphere or land back on Earth's surface. Internationally, there is no policy to address the issue of OD, except to limit the creation of it in the atmosphere. With the lunar magnetic rail stations low cost of launch, missions would be sent into the Earth's atmosphere to collect OD and return it to the lunar station or to Earth's surface. The OD could then be recycled or scrapped for other projects. Though similar missions could theoretically be sent from Earth, the lunar magnetic rail station would achieve the same result with less cost.

A problem that also plagues Earth's atmosphere is the threat of near Earth asteroids (NEA). There are many asteroids in space that pass by Earth on a regular basis. A number of these asteroids are harmless, flying by Earth or burning up in Earth's atmosphere. Within this group of NEAs there is another group known as potentially hazardous asteroids (PHA). These asteroids are asteroids classified by NASA [18] as asteroids that fly with 5 million miles of Earth's atmosphere, can survive coming through the atmosphere, and would cause damage on a regional level or greater. NASA's recent NEOWISE program took a survey of some of the asteroids orbiting near Earth. This survey revealed that there are approximately 4,700 ±1,500 PHA. Each PHA's is estimated to have a diameter of at least 330 feet. NASA estimates that only 20–30% of these asteroids have been found. One such object was 2011 AG5. This Asteroid was discovered in 2011 and in early 2012 was believed to possibly be on a collision course with the Earth [19]. The collision was estimated for a date in 2040. Studies later determined that the asteroid was not on a collision course and would continue to move passed Earth [20]. Though 2011 AG5 will likely not result in a disaster, it is one of many asteroids that continually fly around Earth, threatening the safety of humanity. If a PHA was on a collision course with the Earth, there is, at present, no planned course of action. With the establishment of a lunar magnetic rail station, missions would be sent from the station to intercept PHA collisions, either diverting or destroying them. Tracking and mining of PHA would also be conducted through the use of the magnetic rail station, to prevent future catastrophes and to use PHA's resources on the Earth as discussed earlier.

Use of the Moon as a Gateway into Deep Space

With the use of the magnetic rail system on the Moon as a refuel point or a junction, achieving space travel farther into the solar system would be easier. Long-term exploration as well as short-term commercial operations would benefit from a lunar rail station. According to Mendell [8], space exploration will increase in the future. As space travel becomes more cost effective and more lucrative, the establishment of a lunar magnetic rail station will become more beneficial. As well the magnetic rail station would be able to land OVs onto the Moon. The rails of the station need to achieve a length of 28.9 km. If the direction of the current were reversed, by switching the positive and negative leads, then it would be possible to accelerate the armature to reach a landing OV, match the armatures speed with the OV's in order to land, and reduce current so that the OV and armature slow to a stop. If the OV were to have a lower landing speed than take off speed than the length of the rails would not need to be increased in order to land the OV safely. However, safety regulations and error calculations would need to be factored into the landing system to minimize potential risk.

DISCUSSION

The many benefits of building a station on the surface of the Moon have already been discussed. In order to start a station on the Moon many challenges

need to be overcome before the station can be established. These challenges include launching to the Moon, using materials from the Earth or found on the Moon as building material, and designing a station that would serve as an outpost for both missions launched back to Earth or launched further into the solar system. Along with the physical requirements that are needed to build the station, there are also political considerations that would need to be addressed.

Launching Builders and Material from Earth

In order to build a magnetic launch station on the Moon, a launch system must be first used on Earth. Many different systems have been investigated to be used to launch OVs from Earth to the Moon. One system that would be able to launch OVs to the Moon, or out of the Earth's orbit would be space tethers, which is being researched by Hoyt [9] and others. Tethers Unlimited's space tether design concept uses spinning satellites to transfer the rotational momentum of the satellite into a tangential change in velocity of an OV. Space tethers placed in Low Earth Orbit (LEO) would use the magnetic field generated by from the Earth to maintain orbit and to regain any energy lost in propelling an OV. Designs for these space tethers have been proposed for transfer of OVs from LEO to Geosynchronous Orbit (GEO), or directly to the Moon. A rendition of this system is shown in Figures 3 and 4.

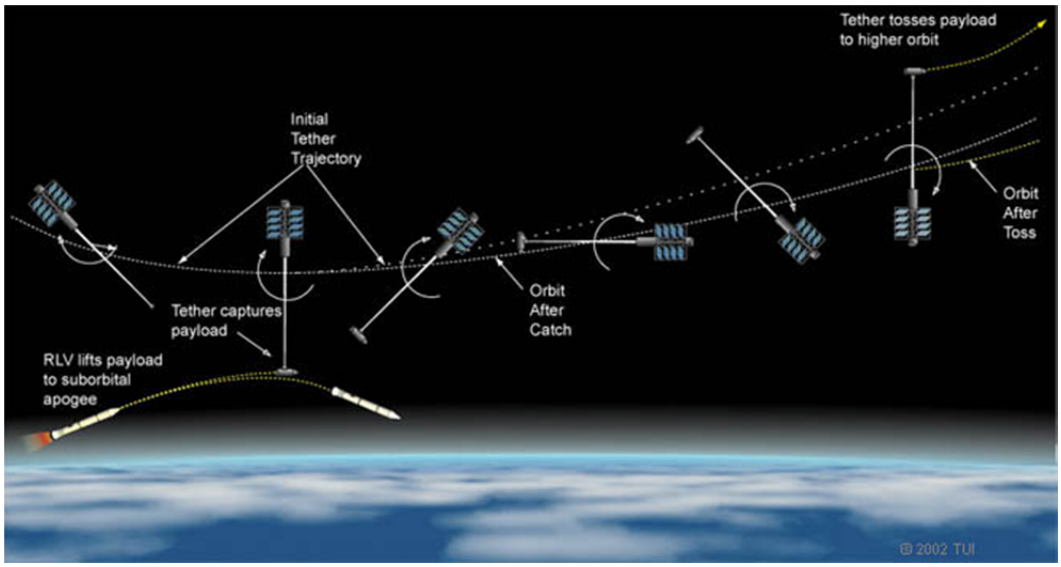

Figure 3: Diagram of how tether system works [9]

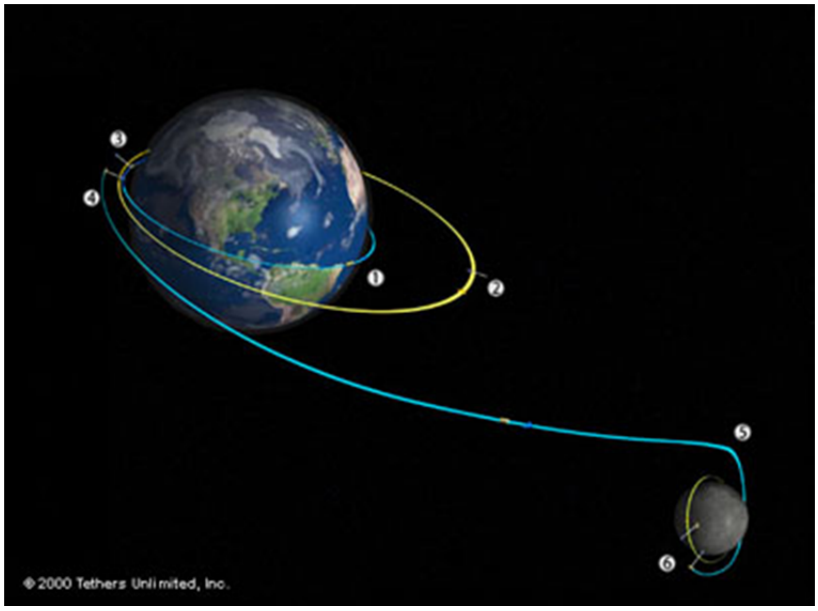

Figure 4: Visual diagram of transfer from the Earth to the Moon. (*Images taken from Tethers Unlimited, Inc.* [9])

Another launch design that has been proposed for less expensive extraterrestrial travel has been a magnetic launch ring, similar to what has been proposed for the Moon. This idea has been researched by Fiske [10]. Fiske research has led to the design of a magnetic launch "ring". This ring is proposed to be between 1 and 8 km. using electromagnetic forces, to propel OVs. The OV would be placed on a conductive sled and the sled would accelerate through the ring. The ring would accelerate an OV to speeds near 10 km/s. This system is estimated to be able to launch OVs at a price of $750/lb ($1650/kg). A photo of the proposed launch ring is shown in Figure 5.

This alone would drastically cut down on the price of space travel. If this technology were to also be applied along with the orbital space tethers, the chemical propellant that would need to be used in launch would be reduced to virtually nothing. This would further increase reduction of the price of a launch. The third and final design that would provide a less expensive means of space transport is a magnetic levitation OV known as the Startram. This system was designed by scientists Maise and Powell [11]. The system is designed to use superconducting cables that repel each other in order to lift a vacuum magnetic levitation tube. This tube would use electromagnetic forces to launch an OV into LEO. The launch would use low acceleration forces around 3 g's. This low acceleration requires a track approximate 1600 kilometers in length. This track would also need to be lifted to at least 20 km above the Earth's surface. The superconducting rails make the design of this system possible. Because of a superconductive rails lack of electrical resistance, several million amperes of current can be generated through the rails. The magnitude of the current needed in

order to lift the rails 20 km off the Earth's surface would be near 200 million amperes through the first conducting rail, which is running through or along the ground. 20 million amperes of current would also need to be sent through the rail that is connected to the tube. This would apply enough magnetic repulsion in order to lift the tube and the rail the necessary height. This project is still in its primary stages and would require at least $60B and an international effort to build.

Figure 5: Launch Ring. (Image from Launchpoint Technologies, Inc. [13])

Materials and Builders Needed to Build the Station

The station would need to be largely made of metal, with solar panels and concentrators placed at a high elevation near the North Pole to capture continuous sun-light. These solar panels would be connected to the main facility, which would be within a crater to avoid direct solar heating. Avoiding this heat would make maintaining the rails at superconductive critical temperatures at all times much more achievable. Because the Moon's surface is rich in metal oxides, surface and deep mining would provide adequate material to manufacture the magnetic launch station. The rails would need to be made out of superconductive material. The rails and solar panels would ideally be manufactured on the lunar surface. This would avoid the expense and time delay of shipping these materials to the Moon. The magnetic rail station would most effectively be established by autonomous robots. With the use of robots, vital supplies, needed to support a human crew, would be spared. Also the robots, while building the station would produce other robots to further assist with construction. According to Mathews [16], the technical capabilities of autonomous robots are quickly advancing. Mathews references studies in artificial intelligence where robotic conversational abilities are improving to the extent that humans are not able to distinguish between talking to a robot or to another human being. Artificial intelligence will have the ability to reproduce copies of itself without human assistance. Once this ability is achieved, robots will be able to travel into space and build stations for other OV. Mathews also states that the level of artificial intelligence needed to perform these tasks may take several decades to develop. Nevertheless, these abilities will be developed in the near future.

Political Concerns

With the possibility of constructing future establishments on the Moon, certain terms and treaties may need to be put into place. According to Abbey and Lane [15], space exploration has been for the most part internationally collaborative. With the development of the International Space Station, many countries have a grown closer together. However, if the Moon were to be seen as a commercial asset, countries may begin to view it differently. Abbey and Lane [15] recount of the confusion in the 1990s of nations attempting to regulate commerce of orbital satellites. The United States for example had more stringent regulations on what satellites could and could not do, in comparison to other nations. These regulations were also carried with satellites that would be exported to other nations. Many other nations quickly declined such satellites, because of the restrictions on technical data that could be acquired. Because of this, The United States fell behind in satellite commerce. With the commercialization of the Moon, similar instances may arise if regulations are not adjusted to changing circumstance. Similar to the discovery of the New World, country would need to make claim of the lunar territory and distribute the satellite in accordance with those involved. The establishment of lunar bases and stations, for both mining and transportation, would need to be within the specifications of established treaties.

In addition the construction of a magnetic launcher on the surface of the Moon that would be capable of sending OVs of several thousand kilograms of mass into the Earth's atmosphere at any location may make different countries uncomfortable. An international agreement may be needed if any establishment is to take root without causing great tension between nations.

CONCLUSION

The idea of an elevator to space has been thought of for at least the past decade. The atmosphere on Earth would put too much stress on an elevator bridge to make one with existing materials. Although this possibility is currently impossible for Earth, a space elevator on the Moon would be much simpler to manufacture. Because the Moon has no atmosphere, existing materials would be strong enough to lift OVs into orbit. Along with this idea is the space tether. A tether in orbit around the Moon, and long enough to reach to the Moon's surface, would be able to lift OVs to a necessary height and velocity for orbit.

The technology that would be needed to launch from the Earth into space already exists. The technology, instead of being used on Earth, could be implemented on the Moon to further reduce the cost of launches between the Earth and the Moon. The use of a magnetic rail station on the Moon would be both inexpensive as well as low maintenance. Superconductive rails would reduce the energy usage that the rail launcher would need per launch. Once on the Moon, valuable minerals and rare elements could be harvested and sent back to Earth without a large fee for transport. These resources could also be utilized by autonomous robots in the construction of the magnetic rail launcher. There are many technologies that also are in existence or swiftly being developed that are able to launch OVs from the Earth to the Moon for a more inexpensive price than traditional chemical propellant. With the employment of one of these technologies the station would be able to be constructed. Although, before a massive project undertaking is started on the Moon, many policies and territorial treaties need to first be established.

ACKNOWLEDGMENTS

This material is based upon work supported by the National Science Foundation under Grant No. EEC-1062984. Furthermore, I would first like to thank these people: Dr. John Mathews, Dr. Sven Bilén, and Mr. Tom Tyson.

REFERENCES

[1] Zahn, Markus. "The Magnetic Field." *Electromagnetic Field Theory*. Malabar: Robert E. Krieger, 1979. 314+. Print.

[2] Hambley, Allan R. "Introduction." *Electrical Engineering: Principles and Applications*. 5th ed. Upper Saddle River: Prentice Hall, 2011. 1-16. Print.
"Magnetic Circuits and Transformers." *Electrical Engineering: Principles and Applications*. 5th ed. Upper Saddle River: Prentice Hall, 2011. 716-31. Print.

[3] "Type 2 Superconductors," *Superconductors.org*. N.p., n.d. Web. <http://www.superconductors.org/Type2.htm>.

[4] Parkinson, R. C. "Why Space Is Expensive–operational/economic Aspects of Space Transport," *ARCHIVE: Proceedings of the Institution of Mechanical Engineers, Part G: Journal of Aerospace Engineering 1989-1996 (vols 203-210)* 205.17 (1991): 45-52. Print.

[5] "Baltimore Gas & Electric Standard Offer Service Rates/Miscellaneous Charges," *BGE.com*. N.p., n.d. Web. <http://www.bge.com/myaccount/billsrates/ratestariffs/electricservice/Electric%20Rates%20Information%20Documents/POLR_Rates_PTC_MiscCharges.pdf>.

[6] Wingo, Dennis. *Moonrush: Improving Life on Earth with the Moon's Resources*. Burlington, Ont.: Apogee, 2004. Print.

[7] "EUREKA! ICE FOUND AT LUNAR POLES." *Lunar.arc.nasa.gov*. NASA, n.d. Web. <http://lunar.arc.nasa.gov/results/ice/eureka.htm>.

[8] Mendell, Wendell W., and Steven Hoffman. "Strategic Considerations for Cislunar Space Infrastructure." (n.d.): n. pag. Web. 2 July 2012. <http://ares.jsc.nasa.gov/HumanExplore/Exploration/EXLibrary/DOCS/EIC042.HTML>.

[9] Hoyt, Robert P. *Responsive Launch of Small Spacecraft Using Reusable In-Space Tether and Air-Launch Technologies*. *Tethers.com*. Tethers Unlimited, n.d. Web. <http://www.tethers.com/papers/MXERSpace2006Paper.pdf>.

[10] Fiske, Jim, *The Launch Ring*. *www.launchpnt.com*. Launchpoint Technologies. Inc, n.d. Web. <http://www.launchpnt.com/Portals/53140/docs/2006-isdc-launch-ring-low-cost-launch-for-space-exploitation.pdf>.

[11] Powell, James, George Maise, and John Rather. *Maglev Launch: Ultra Low Cost Ultra/High Volume Access to Space for Cargo and Humans*. *Startram.com*. The Startram Project, n.d. Web. <www.startram.com/resources-Startram2010.pdf>.

[12] "Momentum-Exchange Tethers." *Momentum-Exchange Tethers*. Tethers Unlimited, n.d. Web. <http://www.tethers.com/MXTethers2.html>.

[13] "The Launch Ring: A Magnetic Satellite Launch System." *Satellite Launch Ring: LaunchPoint Technologies*. Launchpoint Technologies. Inc, n.d. Web. <http://www.launchpnt.com/portfolio/aerospace/satellite-launch-ring/>.

[14] "Temperature on the Moon." *Planetfacts.org*. Planet Facts, n.d. Web. 18 July 2012. <http://planetfacts.org/temperature-on-the-moon/>.

[15] United States. *United States Space Policy: Challenges and Opportunities*. By George Abbey and Neal Lane. Cambridge: American Academy of Arts and Sciences, 2005. Print.

[16] Matthews, John D. "From Here to ET." *Journal of the British Interplanetary Society* 64 (2011): 234-41. Web.

[17] "NASA Orbital Debris FAQs." *NASA Orbital Debris FAQs*. N.p., n.d. Web. 20 July 2012. <http://orbitaldebris.jsc.nasa.gov/faqs.html>.

[18] "NASA Survey Counts Potentially Hazardous Asteroids." - *NASA Jet Propulsion Laboratory*. NASA Jet Propulsion Laboratory, 16 May 2012. Web. 20 July 2012. <http://www.jpl.nasa.gov/news/news.cfm?release=2012-138>.

[19] "Asteroid 2011 AG5 - A Reality Check." - *NASA Jet Propulsion Laboratory*. NASA Jet Propulsion Laboratory, 28 Feb. 2012. Web. 20 July 2012. <http://www.jpl.nasa.gov/news/news.cfm?release=2012-051>.

[20] Brown, Dwayne. "NASA Releases Workshop Data and Findings on Asteroid 2011 AG5." - *NASA Jet Propulsion Laboratory*. N.p., 15 June 2012. Web. 20 July 2012. <http://neo.jpl.nasa.gov/news/news175.html>.

DESIGN OF THE GEOPEBBLE ACCESS POINT WIRELESS CONTROL SYSTEM AND SENSOR NETWORK

Amanda Sweat,* Michael Conway,[+] Robert M. Capuro,[x] and Sven G. Bilén[#]

Department of Electrical Engineering
The Pennsylvania State University, University Park, PA 16802

*Undergraduate Student of Electrical Engineering
Department of Electrical & Computer Engineering
University of Connecticut
Storrs, CT 06269

ABSTRACT

The design, implementation, and demonstration of a multipurpose control and monitoring system (CMS) for use in the geoPebble wireless sensor network is presented herein. The primary role of the CMS is to extend the operating time of network access points (AP) and collect relevant state-of-health (SOH) information via sensor modules. During normal operating modes, the AP has high power consumption, and left to operate continuously will drain its battery power source in a matter of days. The CMS will extend the lifespan of the battery source by responding to wireless commands to turn AP power on or off as required for the geoPebble system's operating modes. The secondary role of the CMS is to provide SOH data through sensors and monitors that provide information concerning axis tilt with respect to the local vertical, orientation with respect to magnetic north, power supply voltage and current monitoring, and internal temperature monitoring. Detection of over-voltage, over-current, or over-temperature readings will be reported via the wireless radio link.

This project resulted in the following deliverables: an Altium schematic and PCB modeling of the proposed control circuit element and data confirming the specifications of the SOH sensor modules.

[#] Faculty Mentor
[x] Secondary Mentor
[+] Graduate Mentor

INTRODUCTION

The geoPebble Project

Glaciology is a critical research field in the twenty-first century. With climate change affecting numerous factors around the globe, knowledge pertaining to ice-sheet density and porosity is of extreme importance. The geoPebble system will provide researchers with a durable system that surpasses present data retrieving technology at a reasonable cost.

The geoPebble system is a large-scale, wireless network of seismic activity monitors. Systems currently used by geoscientists are based on wired technologies that generally need to be deployed in along linear trajectories. That is, seismic sensors, known as geophones, are deployed at regular intervals and are connected by long lengths of multi-conductive cabling. This wiring scheme makes deploying in arctic environments unwieldy at best, and an extremely time-intensive endeavor. Removing the system is likewise intensive, and its sheer bulk makes storage and transportation difficult. The nature of their linear arrangement limits geoscientists to collecting linear data.

The geoPebble system exploits the advantages that wireless systems have to offer. Wireless communication allows geophones to be dispersed in a two-dimensional grid providing geoscientists more comprehensive and useful data. Its lack of wiring makes for easier storage, transport, and deployment.

Most "large" wireless networks communicate with a maximum of 20 nodes; The geoPebble system is specifically designed to work with up to 200 nodes in extremely harsh environmental conditions. While primarily designed for users pursuing glaciological research, the network may be utilized in other harsh environments such as volcanology.

There are several key features of the project that emphasize how the system surpasses current geophysical monitoring technology: the network is easily transportable, 3D imaging of the ice sheets are possible, and ice-flow may be measured over both space and time.

geoPebble Modules

Each geoPebble is "a small, rugged, inexpensive glacio-geophysical sensor node" within a wireless mesh network, and is equipped with wireless communication capability, seismic monitors (geophones), GPS modules, data parsing and storage capacities, and an auxiliary companion board that is the focus of this design project.

Access Points (AP)

Within the geoPebble network, there are four AP units located approximately 500 meters away from the base station. Between 40–50 geoPebbles communicate with each AP, which then relays the collected data directly to the base station. Typical APs are extremely power hungry devices, and can easily deplete a 12-V battery source within a matter of days. The AP module used in geoPebble is the AiroNet 1524SB produced by Cisco Systems, Inc.

Control System Implications

The control system circuit is primarily designed for collecting and responding to SOH measurements and managing the power consumption of the APs. The greatest benefit to the CMS system is its capacity to extend AP battery life, as it is impractical to replace batteries in an arctic environment. The control system was also designed to have functionality such that it fulfills the requirements for the geoPebble's auxiliary companion board. With minor modifications during geoPebble assembly, this control system circuit may be implemented as a supplementary sensor monitor.

CONTROL BOARD DESIGN

System Requirements

The control system design needed to fulfill the following requirements:

- An operating temperature of −40 °C to +85 °C
- Communicate with an XBee Pro (S2B) ZigBee wireless radio
- Capture five measures of state of health
    - Supply voltage level
    - Supply current
    - Internal temperature
    - Axis tilt
    - Magnetic orientation
- Low power consumption
- Deliver power in accordance with Power Over Ethernet (POE) standards
    - 12 V and power delivery to access point (25.5 W max)
- Compatible with access points and pebble modules

Figure 1 provides a system block diagram for the CMS.

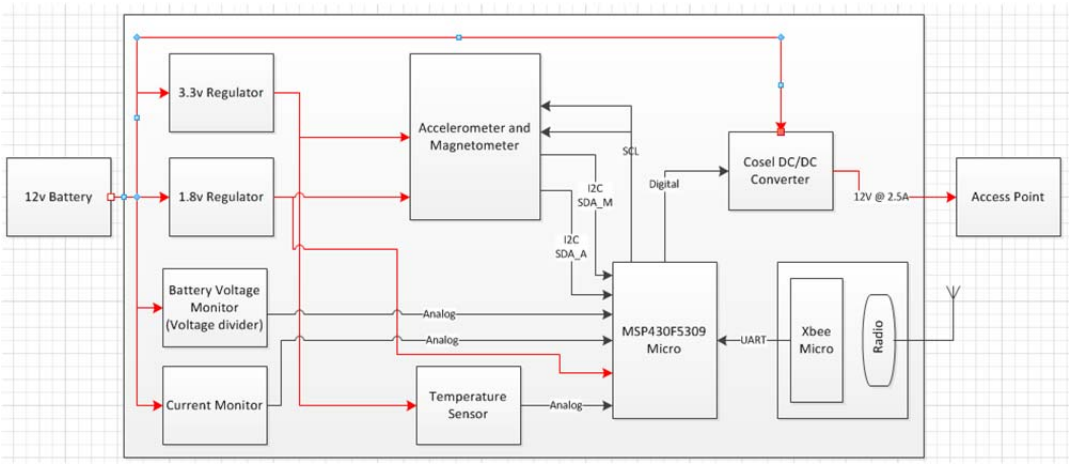

Figure 1: System Block Diagram

The control board follows a standard Printed Circuit Board (PCB) layout with surface mounted components powered by a 12-V DC source. Because some components output data using the I^2C data protocol, a secondary microcontroller was chosen to communicate with the radio's built in microcontroller.

Microcontroller

The control circuit components communicate with an MSP430F5509 microcontroller produced by Texas Instruments. This particular microcontroller is a 48-pin RGZ model with UART, I^2C buses, 4 ADCs and 31 digital IO pins. It runs on a 3.3-V supply voltage, and has low internal power dissipation. Microcontrollers with a smaller number of pins were researched; however, due to the need for UART and I^2C communications, MSP430 models with fewer pins lacked the necessary analog pins.

TMP20 Temperature Sensor

The TMP20 is an analog temperature sensor produced by Texas Instruments that comes in a 6-pin SOT package. It has ±2.5 °C accuracy from −55 °C to +130 °C, which easily meets the system's requirements. It has minimum power draw and can run on a 3.3-V supply. It has a linear transfer function with a slope of −11.77 mV/°C. The device dissipates up to 19.8 μW of power. The output of the TMP connects to pin 3 on the MSP430.

Battery Voltage Monitor

To monitor the 12-V supply voltage, a voltage divider was designed using 10-kΩ and 1.3-kΩ resistors to provide an analog voltage output signal between the values of 0 V and 1.38 V. This output is connected to pin 2 on the MSP430.

LT6106 Current Monitor

To monitor current draw from the supply voltage, a 6-pin LT6106 current sensor from Linear Technology was used. The LT6106 has an input voltage range from 2.7 V to 44 V and an operating temperature range of −40 °C to +125 °C. This sensor observes current passing through an external sense resistor, and has an analog voltage output with a voltage swing of 1.4 V. The sensor's output voltage signal and sense voltage share a positive linear relationship. This output is connected to pin 1 on the MSP430.

LSM303DLM Dual Accelerometer/Magnetometer Sensor

The LSM303DLM module is a dual accelerometer and magnetometer sensor that has the ability to measure device axis tilt[1] and orientation with respect to magnetic north. This device transmits serial data for both acceleration and magnetic orientation using the I^2C data protocol. Both clock signals required for the LSM303DLM are taken from the same clock signal produced by the MSP430.

[1] Using acceleration vectors and trigonometry the axis tilt of the device can be determined.

MCP1702 1.8-V and 3.3-V Regulators

The MCP1702 regulator comes in a 3-pin SOT-23A package with standard output voltage values. The 1.8-V model is marked with the letters "HCNN"; the 3.3-V model is marked with the letters "HGNN". Each model can output up to 250 mA of current. With a supply voltage of 12 V, this leads to a maximum power dissipation of 2.6 W and 2.2 W, respectively. The HCNN model powers reference voltage pins 23 and 22 on the LSM303DLM, as well as reference pins 5, 11, and 28 on the MSP430. The model's operating temperature range of −40 °C to +125 °C and low dropout voltage of 625 mV make this an affordable and reliable regulator choice.

MGFS302412 DC/DC Converter

The MGFS302412 converter takes the irregular output voltage of the 12-V source and outputs a steady 12 V at currents up to 2.5 A, delivering up to 30 W of power and meeting Power over Ethernet (POE) standards. The converter takes two inputs. Input one is the 12-V supply and input two is a logic-level signal generated by pin 36 on the MSP430. When it receives a logical high signal, the converter is turned on and outputs power to the access point. Conversely, when sent a logical low signal the converter is turned off. Note that the converter's TRM pin is left open as there is no need for output voltage adjustment. This converter eliminates the need for standalone FET and gate driver devices, simplifying the system component-wise and reducing potential component failure. Its small size (with dimensions in mm: 20×51×14) makes it compact and a sensible choice for the control board.

Sensor Power Budget

One of the primary goals of this design was to have the sensor board consume minimal power during the access point's lifespan. Table 1 summarizes the power dissipation for the SOH sensor network. Total current draw was calculated to be 2.5 mA, and total power dissipation was calculated to be 27 mW.

Table 1: Sensor Network Power Budget for geoPebble Control Board

Device	# per board	I_S per Device (mA)	V_S (V)	Power Subtotal (mW)
Voltage Divider	1	1.061	12	12.73
LT6106	1	1	12	13.08
LSM303DLM	1	0.36	3.3	1.188
TMP20	1	0.006	3.3	0.0198
	Total Current:	2.427	Power Total:	27.0178

The following three equations come from the LT6106 datasheet [1] and were used to calculate the total power dissipated by the current sensor:

$$P_{\text{out}} = (V_{\text{in}} - V_{\text{out}})(I_{\text{out}}) \quad (1)$$

$$P_q = (V^+ - V^-)(I_s) \quad (2)$$

$$P_{\text{total}} = P_{\text{out}} + P_q \quad (3)$$

More work needs to be done to determine the overall power budget. The duty cycles of the MSP430 microcontroller will need to be taken into consideration, and was outside the scope of this project.

Control Board Cost Budget

Table 2 details the component budget for the CMS. With four access points in the network, the total component cost (not including PCB) for the wireless network will be $296, easily meeting the requirement for a low-cost system.

Table 2: Component Budget for geoPebble Control Board

Manufacturer Part #	Distributor	Quantity	Total Cost	
LSM303DLMTR	DigiKey	1	$8.61	
TMP20AIDRLT	DigiKey	1	$1.32	
LT6106HS5#TRMPB	DigiKey	1	$2.25	
MCP1702T-1802E/CE	DigiKey	1	$0.59	
MCP1702T-3302E/CE	DigiKey	1	$0.59	
ERJ-3GEYJ132V	DigiKey	1	$0.10	
ERJ-3GEYJ103V	DigiKey	1	$0.10	
MSP430F5509IRGZR	DigiKey	1	$4.80	
MGFS302412	TRCelectronics	1	$53.57	
---	DigiKey	11	$1.10	
---	DigiKey	3	$0.98	
		Total:	$74.01	

DATA PROTOCOLS

UART Protocol

The Universal Asynchronous Receiver/Transmitter (UART) protocol translates data between parallel and serial form. In this design, the XBee-Pro S2 ZigBee module communicates with the MSP430 MC via UART protocol.

I^2C Protocol

I^2C is a two-line, serial protocol over which signals of clock (SCL or SCK) and data (SDA) are sent. The master device may have multiple slaves (multiple masters are possible but uncommon). To establish communication, the master sends an inquiry to a slave and awaits a response. If the slave responds with an acknowledgement bit, the master understands the device is prepared to

transmit/retrieve. The master in this design is the MSP430 MC, and its slave is the LSM303DLM module.

RESULTS AND SENSOR CHARACTERIZATION

Design Schematic

The Altium Designer ’09 software package was used to create and design the access point CMS schematic. Each sensor component was modeled using schematic drawing tools and three-dimensional, PCB modeling tools. Power regulating devices and the wireless radio were not modeled in the PCB layout. Figure 5 presents the entire circuit diagram layout.

Sensor Characterization

To characterize the TMP20 sensor, standard soldering techniques were used with through-hole components. The circuit was placed in a TestEquity 1000 Series Temperature Chamber. Filtering capacitors of 112 nF and 1 nF were attached to the power supply and analog output, respectively. A Keithley 2304A High Speed Power Supply was used to supply 3.3-V DC to the circuit, and the output was measured using an Agilent 34970A Data Acquisition/Switch Unit. As the data sheet claimed, there is a linear, negative relationship between temperature and output voltage. This negative correlation is easily observed below in Figure 2. The slope of the transfer function using acquired data is −11.36 mV/°C, resulting in a percent error of 3.48% from the expected −11.77mV/°C.

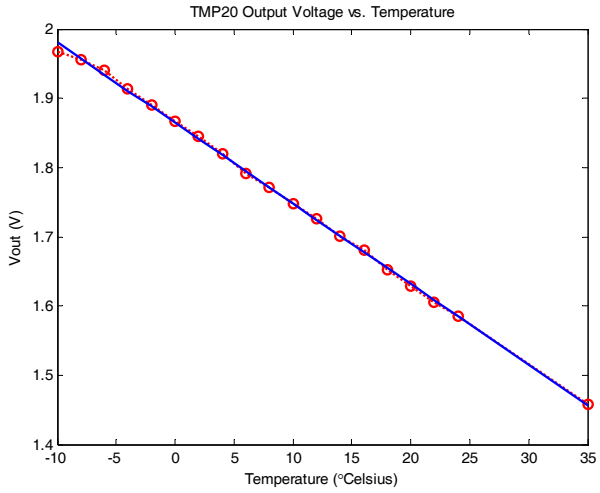

Figure 2: TMP20 Temperature Sensor Characterization Curve

In a similar fashion, the LT6106 current monitor was soldered using through-hole components. The circuit wiring is presented in Figure 3. Exact resistance values for each resistor are as follows: R_{SENSE} = 20.0 mΩ, R_{LOAD} = 79.0 Ω, R_{IN} = 100.5 Ω, R_{OUT} = 996.0 Ω. The shunt resistor of 20 mΩ was a surface mount component, and was modified using thin wires to work as a through-hole device.

The load resistance of 79.0 Ω was a 3-W power resistor. An Agilent E3631A Triple Output DC Power Supply was used to perform a DC sweep from 9 V to 14 V, mimicking the fluctuations of the 12-V car battery source. Output voltages were measured using a Fluke 87 True RMS Multimeter. The expected conversion factor was 200 mV/A, and the actual conversion factor was 256.1 mV/A; a percent error of 28.05%.

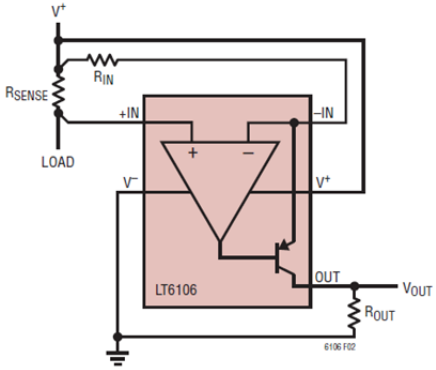

Figure 3: LT6106 Circuit Diagram [1]

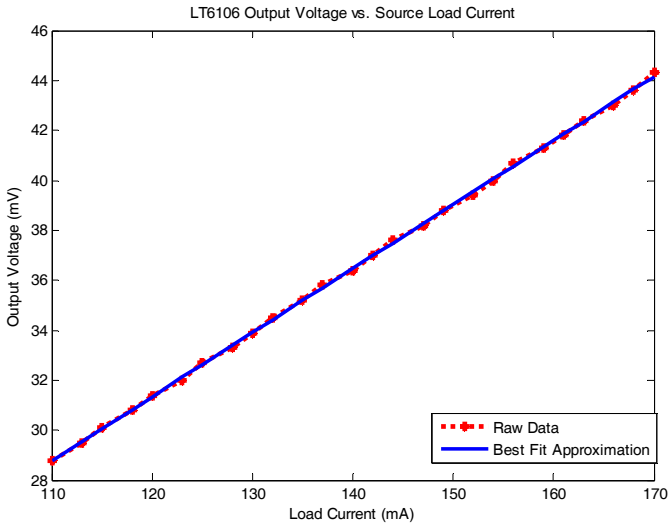

Figure 4: LT6106 Current Sensor Characterization Curves.

DISCUSSION

The LT6106 does not have the expected conversion factor claimed in the data sheet. Since only one chip was tested a single time, multiple units should be tested several times each in the future for chip-to-chip consistency. If the sensors provide inconsistent readings, other current sensors should be pursued.

Both 1.8-V and 3.3-V regulators are linear regulators. To increase efficiency, it is recommended to implement switching regulators. In this case, linear regulators are inefficient and will be dropping 8.7-V and 10.2-V in an ideal scenario.

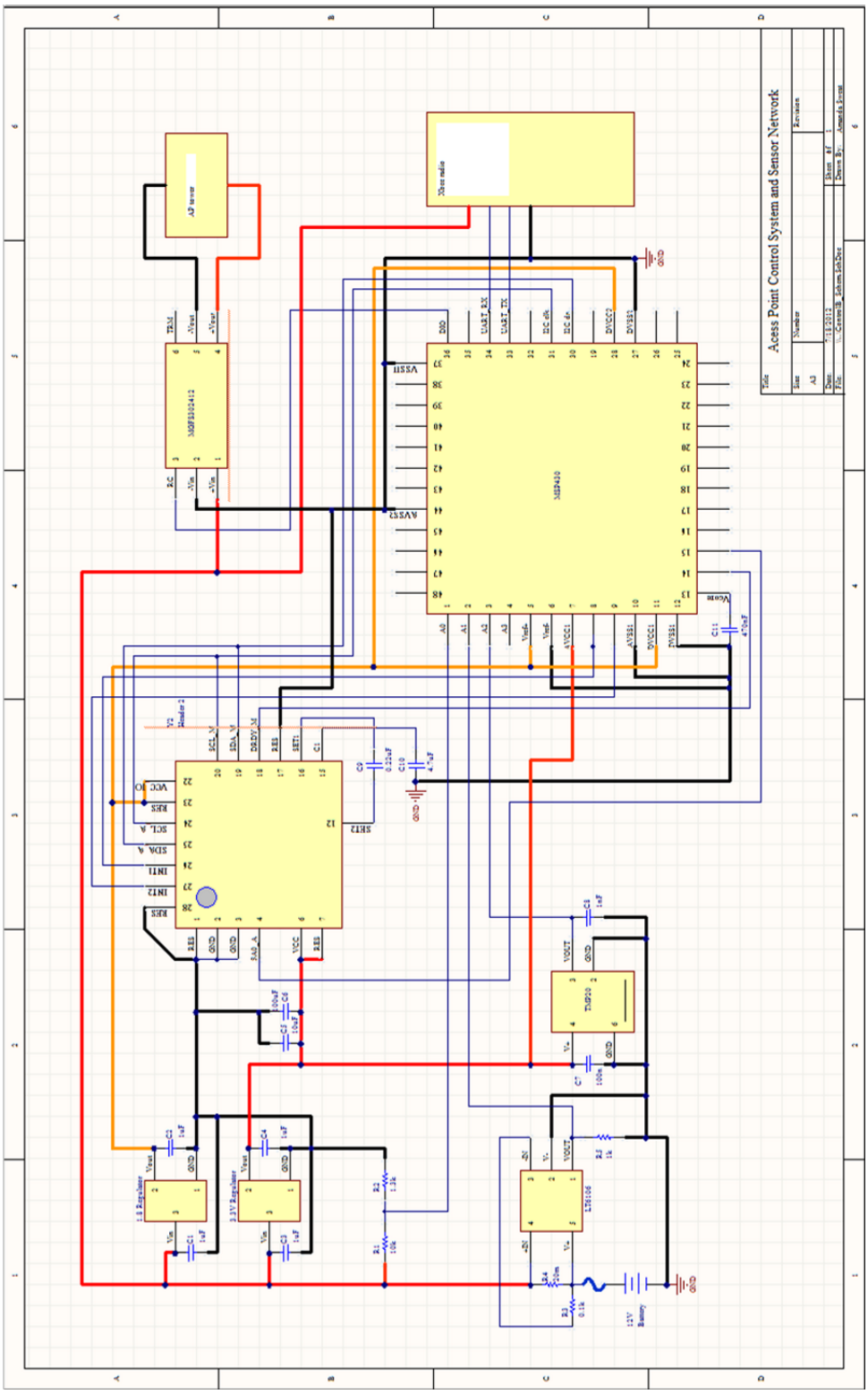

Figure 5: Control System Schematic

The MSP430 model used in this design has a large number of unused pins represented unused resources. A microcontroller with fewer unconnected pins is preferable. However, microcontrollers with a smaller number of pins do not provide enough analog inputs. Due to the required I^2C bus, UART interfaces, and reference pins, the seemingly abundant number of ADC pins available is not enough. Further research into microcontrollers that provide enough ADC interfaces while supporting all other necessary interfaces with a lower pin count is recommended.

The Honeywell LSM303DLM was not characterized in this project due to complications with the software meant to read I^2C data streams. Characterization of this compass sensor using bus pirates or Arduino open-source technology is recommended for future work.

CONCLUSION

This control system design lays the groundwork for the geoPebble dual access point control system and auxiliary companion board. The system was successfully decomposed into its critical parts and characteristic curves were created for sensor network components. Further, rigorous testing of these components is highly recommended. As this system will be in harsh, arctic conditions with sub-zero temperatures and high wind speeds, it is critical this system be tested for durability.

ACKNOWLEDGMENTS

This material is based upon work supported by the National Science Foundation under Grant No. EEC-1062984. Furthermore, I would like to thank a number of people for their continued support throughout this endeavor. My secondary faculty mentor, Robert Capuro, provided me with invaluable insight that served to enlighten me on numerous occasions. Graduate student and program liaison Thomas Tyson provided remarkable support throughout the program for my colleagues and me. Graduate students Michael Conway and Tyler Boehmer were also imperative to my success. I appreciate the time and effort they've taken to answer my many questions, and guide me when I felt completely baffled. Finally, thank you Sven Bilén for organizing this program. Without your initiative and drive, this program would not have been possible.

REFERENCES

[1] Linear Technology TDS for LT6106 36V Low Cost High Side Current Sense in a SOT-23. 2007. Linear Technology. 18 July 2012 < http://cds.linear.com/docs/Datasheet/6106fa.pdf>

ADAPTIVE SIGNAL PROCESSING METHODS FOR REMOVING MATERNAL INTERFERENCE NOISE FROM FETAL ELECTRO-CARDIOGRAMS

Jamilya Sultanova,* W. Kenneth Jenkins,[#] and A. David Salvia[#]

Department of Electrical Engineering
The Pennsylvania State University, University Park, PA 16802

*Undergraduate Student of
Department of Electrical Engineering
The Pennsylvania State University
University Park, PA 16802

ABSTRACT

In the medical profession fetal electrocardiograms (Fetal ECGs) are often used to examine fetal cardiac development for the early diagnosis of heart abnormalities and diseases. A strong maternal heartbeat often interferes with the fetal heartbeat signal and needs to be removed via signal processing techniques. However, it appears that signal processing techniques currently used in the area of Fetal ECG are still underdeveloped. Thus, more research needs to be conducted for the improvement of signal processing techniques that can more effectively remove maternal heartbeat interference from Fetal ECC recordings. In this project, the objective is to increase the signal-to-noise ratio of the Fetal ECG via using two types of adaptive filtering methods: 1) a Basic Time Domain Adaptive Filter and 2) a more advanced Transform Domain Adaptive Filter. The first phase of this research will concentrate on Fetal ECG signals filtered by a Basic Time Domain Adaptive Filter. Then, while the input of the system remains the same, the second phase of the project will replace the Basic Time Domain Adaptive Filter with a more advanced Transform Domain Adaptive Filter. The results of using these two adaptive filtering methods will be compared and an analysis of the effectiveness of Adaptive methods will be presented.

INTRODUCTION

Fetal ECGs contain information that can detect the risk of heart defects of the fetus [1]. There are two methods of recording Fetal ECGs: i) Invasive method and ii) Non-invasive method.

[#] Faculty Mentor

The Invasive method is performed by placing a scalp electrode on the fetus after the water has broken, which is possible only during labor [1, 2]. The Non-invasive method requires placing several electrodes on the abdominal area of the pregnant patient. Abdominal ECGs can be performed during the whole period of pregnancy and delivery, providing the possibility for long-term monitoring of the fetal cardiac development. However, the main difficulty in using non-invasive Fetal ECG is extracting the small amplitude fetal signal contaminated by a large number of interferences and noises. Baseline drift (patient's breathing and movements), power-line interferences, myographic (muscle) signals from both mother (including mother's heart) and the fetus, and the distortion from passing through different layers of tissues are among the most significant interference signals that may corrupt Fetal ECG recordings [3]. In this project the source of noise is generalized to be known as maternal interference, not just maternal heartbeat. The main source for the reference of noise is the Mother's ECG signal taken from the thorax area, which while passing through the body becomes contaminated and adds to the abdominal signal. This abdominal signal is analyzed and processed to detect uncorrupted Fetal ECGs.

Signal processing of adult ECGs has been advancing over last century. However due to a low signal-to-noise ratio (SNR) value of the Fetal ECG compared to that of Maternal ECG and no availability of a database of signals in this area, the methods of extraction of the Fetal ECG have not been fully researched. In [3] the author discusses the existing methods of signal processing: the Direct Fetal Analysis, Adaptive Filtering, and Linear and Nonlinear Decomposition. The direct method is based on analyzing the contaminated Fetal ECG without any processing. This method is not very applicable since it is dependent on the period of gestation and the fetal presentation. The adaptive filtering method is based upon using a reference maternal heartbeat signal to train an adaptive filter to remove the unwanted maternal interference from the fetal heartbeat signal. The main difficulty in applying this method is the need to have a good reference signal that could match the noise part of the signal of interest. One more method is decomposing the signal into different components by suitable basis functions. The linear decomposition is feasible for predictable linear parts of the system. However, most of the noise is nonlinear and thus it adds computational complexity.

The two methods used in the project are based on two types of adaptive filtering: i) a Basic Time Domain Adaptive Filter and ii) a more advanced Transform Domain Adaptive Filter. The adaptive filters are capable of removing the interference signal from the signal of interest if the contaminating signal is correlated with the reference signal [4]. In this project the signal of interest is the Fetal ECG and the reference signal is the Maternal ECG. The results of this project may give more information on whether the Maternal ECG is well correlated with the noise present in the Fetal ECG and whether the basic adaptive noise cancelling techniques can give sustainable results in removing noise from the Fetal ECG.

PRINCIPLES OF ADAPTIVE NOISE CANCELLATION

Time Domain Adaptive Filter

Figure 1 below shows the basic principles of the work of the Adaptive Noise Canceller. The Primary input is the signal s and the noise n_0, which is uncorrelated with the signal s. The Reference input is a noise n_1 that is uncorrelated with the Primary signal but correlated in some way with the noise in the Primary input, n_0. The noise signal n_1 is filtered through an Adaptive Filter (AF) to produce the output $y[n]$ that is as close to n_0 as possible. This output is then subtracted from the Primary input ($s+n_0$) to produce the output $z = s+n_0-y$. The Adaptive Filter (AF) is adjusted by feeding back the output signal to minimize the error. Thus, the AF can operate under changing conditions [5].

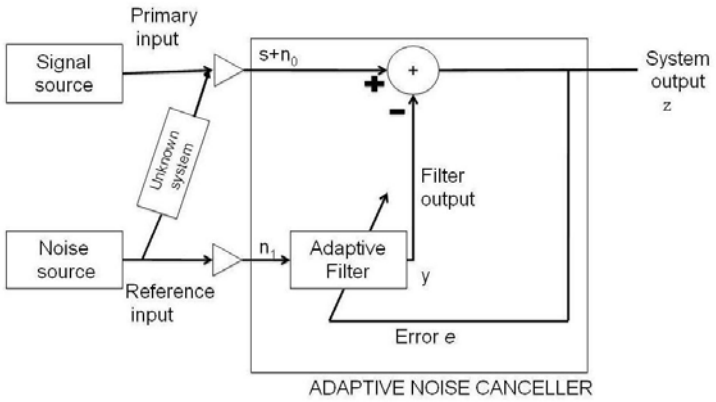

Figure 1: The adaptive noise cancelling concept in the time domain

Figure 2 illustrates the AF algorithm, which in this case is the well-known Least Mean Square (LMS) algorithm. In Figure 2 $x(n) = n_1$ (the reference noise signal) and the tap weight function is $h(n,k) = w_k$, where k denotes the k-th element of the tap weight vector $\boldsymbol{h}(n)$. The LMS algorithm minimizes the error $e(n)$ given by the difference between $(s(n)+n_0(n))$ and $y(n)$ by an approximation to the steepest descent method, as shown below. The error to be minimized is defined as

$$e(n) = (s(n)+n_0(n))-y(n), \tag{1}$$

where the output of the adaptive filter is the input convolved with adaptive filter coefficients[6]

$$y(n) = \boldsymbol{h}(n)*(\boldsymbol{s}(n)+\boldsymbol{n}_0(n)). \tag{2}$$

The coefficients of the adaptive filter $\boldsymbol{h}(n)$ are updated using the following equation, where μ is the step size of the LMS algorithm:

$$\boldsymbol{h}(n+1) = \boldsymbol{h}(n)+\mu e(n)(\boldsymbol{s}(n)+\boldsymbol{n}_0(n)). \tag{3}$$

An additional power normalization factor might be added in order to optimize the convergence rate. The power normalized update equation is as follows:

$$\boldsymbol{h}(n+1) = \boldsymbol{h}(n)+(1/N)\mu e(n)(\boldsymbol{x}(n))/(\alpha+\boldsymbol{x}(n)\boldsymbol{x}^{\mathrm{T}}(n)), \tag{4}$$

where α is a small factor relative to the magnitude of the variance of $x(n)$ that prevents the denominator from possibly becoming too close to zero, $x(n) = s(n)+n_0(n)$, $x^{\mathrm{T}}(n)$ is the transpose of $x(n)$, and N is the size of the filter.

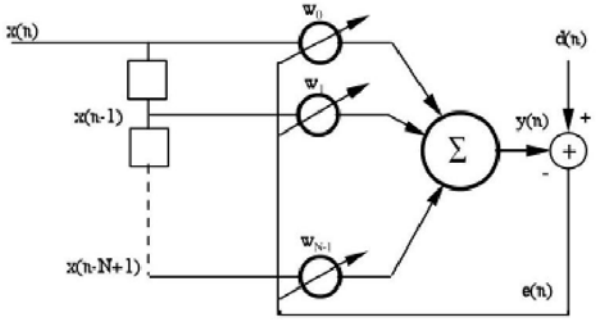

Figure 2: The AF diagram in the time domain

Transform Domain Adaptive Filter

Adaptive Filters can also be implemented in the Transform Domain. Figure 3 demonstrates the concept. In Figure 3 the * indicates the LMS adaptive filter, where $d[n]$ is the desired signal, $\boldsymbol{x}(n)$ is a row vector of N samples of a reference signal, which then passed through an N-point FFT to create a frequency-domain samples $\mathbf{X}[n]=[z_0, z_1, \ldots, z_{N-1}]$. The signal $\mathbf{X}[n]$ is then filtered by an LMS adaptive filter using the following definitions [7]:

$$y(n) = \mathbf{H}[n]\mathbf{X}[n] \tag{5}$$

where $y(n)$ is output of the filter in the time domain and $\mathbf{H}[n]$ is the transform domain tap weight vector defined as:

$$\begin{gathered}\mathbf{H}[n+1]=\mathbf{H}[n]+\mu e(n)(\alpha \boldsymbol{I} +\boldsymbol{\Lambda}^2)^{-1}\mathbf{X}^*[n] \\ \boldsymbol{\Lambda}^2 = \mathrm{diag}\,[\sigma^2_1, \sigma^2_2, \ldots, \sigma^2_N],\end{gathered} \tag{6}$$

where $\sigma^2_i = E[|X_i[n]|^2]$. The factor of $(\alpha\mathbf{I} +\boldsymbol{\Lambda}^2)^{-1}$ implements power normalization that accounts for the optimization of the convergence rate [7], and $\mathbf{X}^*[n]$ is the conjugate of $\mathbf{X}[n]$. Similarly, as in the Time Domain update equation (4), $\alpha\mathbf{I}$ is a small factor that prevents dividing by a near-zero term when σ^2_i becomes very small.

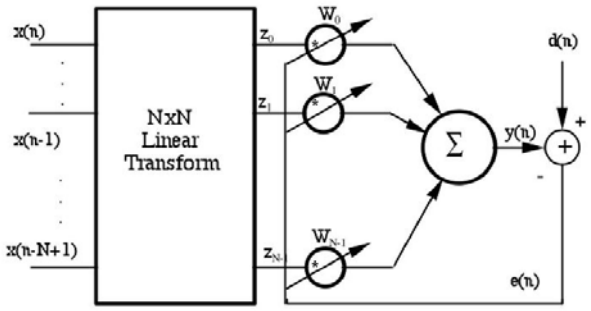

Figure 3: The adaptive noise cancelling concept in transform domain.

EXPERIMENT DESCRIPTION

The experiment is separated into three parts: i) a set of preliminary experiments, ii) the Time Domain Adaptive Filter and iii) the Transform Domain Adaptive Filter. The first part is the set of preliminary experiments that were conducted in order to prepare the MATLAB codes for implementing the data of interest. The two latter parts involve filtering out the Mother's Interference from the abdominal ECG signal using the two adaptive filter approaches discussed earlier.

The ECG signals used in parts ii and iii were taken from the Non-Invasive Fetal Electrocardiogram Database [8]. It is a series of 55 multichannel abdominal Fetal ECG recordings taken from a single subject over a period of 20 weeks. The recordings include two thoracic (maternal ECG) signals and three or four abdominal (maternal + fetal ECG) signals. The signals were digitized with a sampling frequency of 1 kHz and a 16 bit resolution. Figures 4a and 4b show the time-domain plot and the spectral plot of the unfiltered abdomen for 'sample 102'.

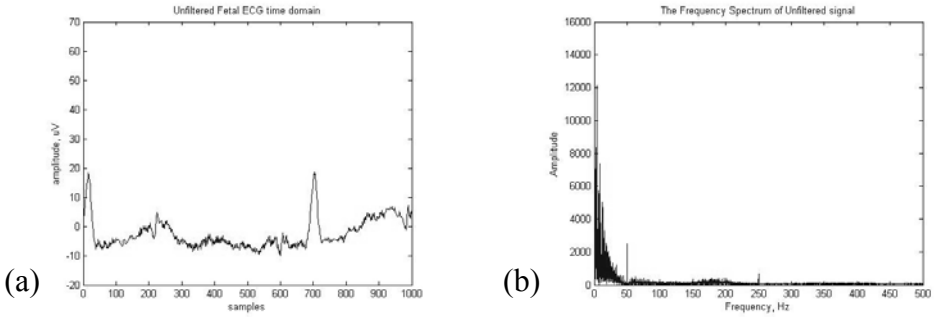

(a) (b)

Figure 4: (a) Unfiltered Fetal ECG time domain; (b) Frequency spectrum

Part 1: Preliminary Experiments

a) Adaptive System Identification

The first step in setting up the experiments is creating a program to perform adaptive system identification. The task is to identify an 'unknown' system using

an 8-tap adaptive filter. The 'unknown' system in this experiment is described by the following impulse response $\boldsymbol{h}_m$ and corresponding frequency response shown in Figure 5:

$$\boldsymbol{h}_m = [-0.033, -0.089, 0.099, 0.478, 0.478, 0.099, -0.089, -0.033]$$

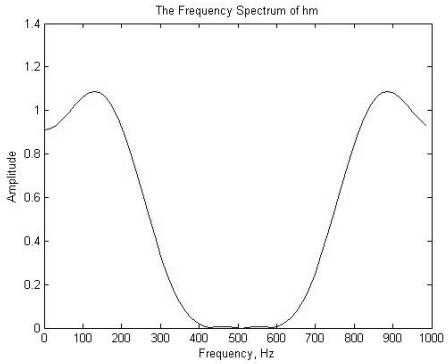

Figure 5: Frequency response of the unknown system

The input to the system is Gaussian white noise, which is an input to both the 'unknown' system $\boldsymbol{h}_m$ and to the adaptive system. The diagram for the problem is shown below in Figure 6. In Figure, 6 $d(n)$ is the output of the $\boldsymbol{h}_m$ system, $y(n)$ is the output of the filter, $e(n)$ is the difference between $d(n)$ and $y(n)$ which is then fed back into the filter in order to minimize the error and to identify the 'unknown' system. This experiment helps to get acquainted with the concept of adaptive filtering.

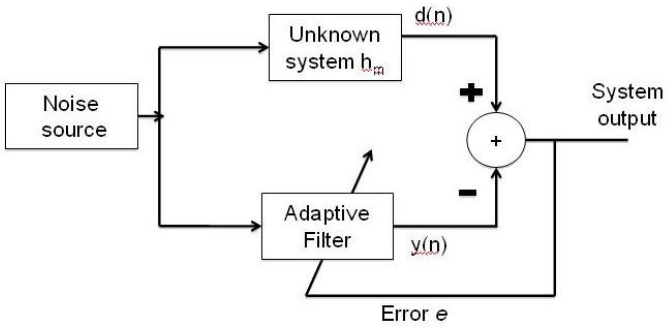

Figure 6: System Identification configuration

b) Illustration of using Time Domain Adaptive Noise Canceller (ANC):

The task is to remove additive colored noise from a maternal ECG using the Time Domain ANC. The maternal ECG is artificially contaminated with colored noise, created by passing Gaussian white noise through the known system h_m. The main principle is illustrated in Figure 1, where the primary input is the sum of the maternal ECG and the colored noise, and the reference is the Gaussian white noise.

c) Illustration of using Transform Domain ANC to remove additive Gaussian colored noise from maternal ECG:

This part is the modified version of part b). The filter in part b) is changed to the Transform Domain.

d) Illustration of Time Domain ANC to remove sinusoidal signal of one frequency from a sinusoidal signal of another frequency:

This experiment is stimulating the behavior of the ECG signals that will be used in the main experiment part. The parallel is that the Maternal ECG signal is supposed to have lower frequency compared to the Fetal ECG signal [3]. Also the amplitudes of the sinusoids are correspondingly high for the lower frequency signal (maternal equivalency) and low for the higher frequency signal (fetal equivalency).

Part 2: Time Domain Adaptive Filter

Part two of the project demonstrates the ability of the Time Domain Adaptive Filter to predict and remove the Mother's interference signal from the Fetal ECG. The Time Domain Adaptive Filter is an *N*-tap filter, with *M* number of iterations, and an adjustable step size μ. The signal to be cleaned is the abdominal ECG signal (consisting of the desired fetal heartbeat signal corrupted by a strong maternal heartbeat signal), the reference signal is the thorax ECG signal (consisting of just the maternal heartbeat signal). The reference signal is fed to the Adaptive filter to predict the contamination noise in the abdominal signal and remove the noise from abdominal signal. In this part the samples from different dates are tested to see if the signals vary and how this variance influences the ability of the adaptive filter to filter the noise out. The first sample is 'sample_102' taken on November 16th 2003 at 9:49 pm. The next one, sample_154, is from the same date but taken 10 minutes later. The last signal, sample_444, is from 4 months later March 15th 2004 at 10:53 pm.

Part 3: Transfer Domain Adaptive Filter

Part three of the experiment tests the Transform Domain Adaptive Filter on the same input data as in part two. The adjustable parameters are changed to give better result. For each set of data the filter size, number of iterations and the step size are not changing.

EXPERIMENTAL RESULTS

Part 1: Preliminary Experiments

a) Adaptive System Identification

In the first part of the Preliminary Experiments, the Adaptive System Identification was tested. Using an 8-tap LMS Adaptive Filter the 'unknown' system is identified. Figure 7 shows the learning curve, which represents the rate

of improvement of the squared error in dB. The floor of the learning curve reaches −350 dB, which is the lower limit of the computer word length. Looking at the actual values of the 'unknown' system and the 'identified' system, the vectors are identical to 5 decimal digits.

b) Illustration of using time domain Adaptive Noise Canceller (ANC)

The code was implemented with the freedom of adjusting the size of the filter, the number of iterations, and the value of the step size (μ). In this part the 8-tap Adaptive filter, running through 10000 iterations with the step size of 0.01 was used to cancel the colored noise from the thorax signal. Figure 8 shows the unfiltered signal ('colored' thorax). Figure 9 shows what the clean thorax signal should look like. Figure 10 shows the result of the ANC system—the noisy thorax signal after passing it through the adaptive filter. Note that it takes about 500 iterations for the filter to converge. Figure 11 shows the last 2000 samples of the thorax only, which makes it easier to compare to Figure 9.

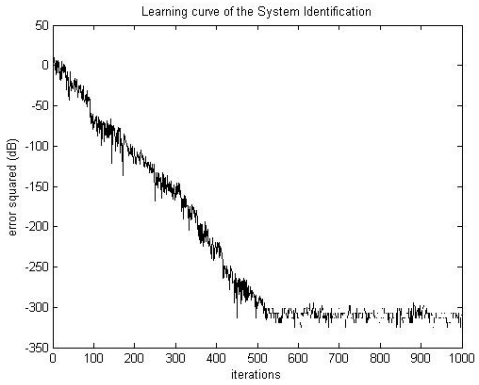

Figure 7: Learning Curve of the System Identification

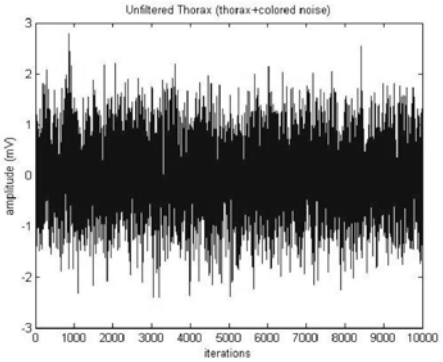

Figure 8: Unfiltered Thorax signal

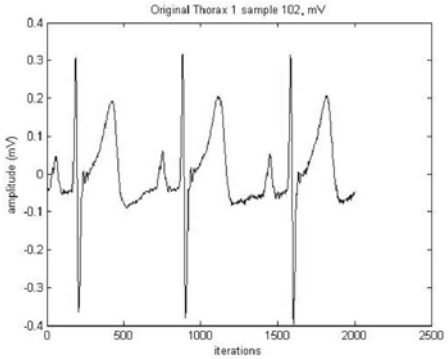

Figure 9: Same signal last 2000 samples

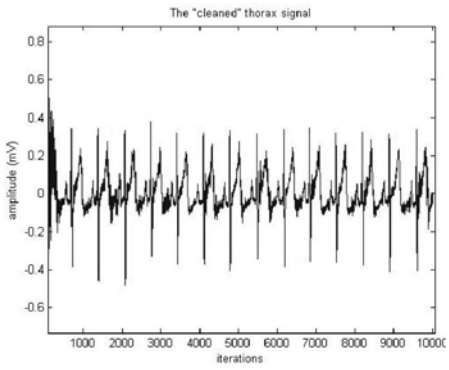

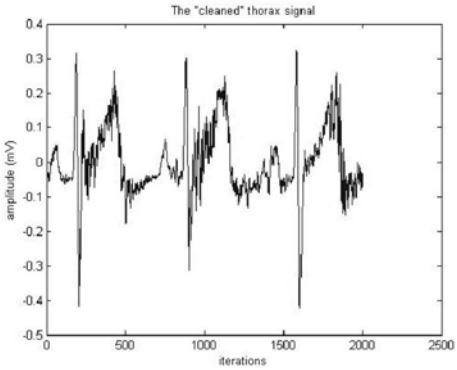

Figure 10: Cleaned Thorax signal **Figure 11:** Same signal last 2000 samples

c) Illustration of using the Transform Domain ANC to remove additive Gaussian colored noise from maternal ECG

The same input and adjusted parameters are used as in the Time Domain filter in part b), but now the filter is in the Transform Domain. Figure 12 shows the filtered thorax signal. As in the Time Domain filter, the filter converged in about 500 iterations. Figure 13 correspondingly demonstrates the last 2000 samples of the signal. Comparing the results for the Time Domain (Figure 11) and Transform Domain (Figure 13) the latter filter presents a cleaner signal.

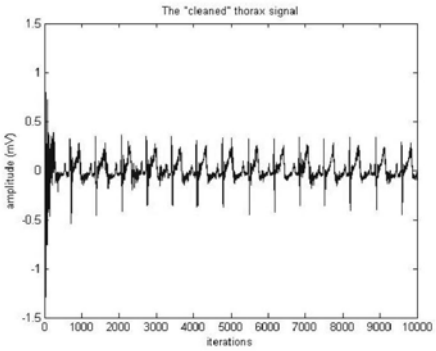

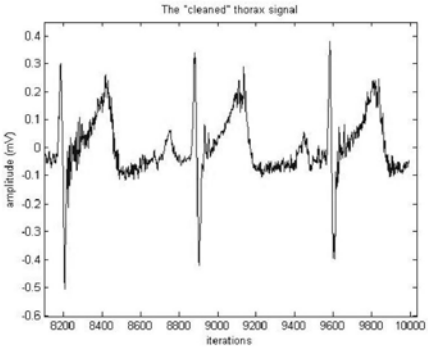

Figure 12: Cleaned Thorax signal **Figure 13**: Same signal last 2000 samples

d) Illustration of Time Domain ANC to remove sinusoidal signal of one frequency from a sinusoidal signal of another frequency

The signal of interest is a sum of sinusoids of frequencies 3 Hz and 6 Hz, and amplitudes of 0.1 and 0.2 correspondingly. This signal is then contaminated by a sum of sinusoids of frequencies of 1 Hz, 3 Hz and 5 Hz, each with amplitudes of 1 (the noise signal). The reference signal in the training is identical to the noise. It is important to note that the amplitude of the signal of interest is much smaller than the amplitude of the contamination signal, mimicking the low amplitude fetal signal and a stronger maternal signal in a real ECG signal. In addition, one of the frequencies (3 Hz) is duplicated in both the noise and the signal of interest, which

is expected to have similar behavior as fetal and maternal signals being somehow correlated. Figure 14 and 15 show the unfiltered and the reference signals correspondingly. The plots appear to be almost identical because the signal of interest is hidden in the corrupting noise, due to the fact that the signal of interest is of very low amplitude and the frequencies are in a narrow range. Figure 16 is a plot of both the result of the filtered signal and the clean desired signal of interest. This adaptive filter does a great job at removing the large corrupting noise signal from the desired signal.

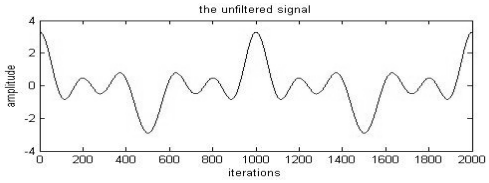

Figure 14: Unfiltered signal

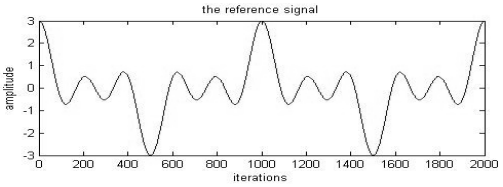

Figure 15: The reference signal

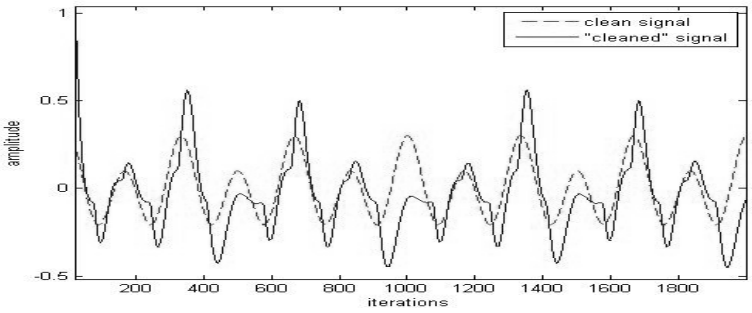

Figure 16: The cleaned and the clean signals

The filter converges in about 100 iterations, which is concluded from the fact that the amplitude of the "cleaned" signal, decreases to a level of the signal of interest after 100 iterations. The result of filtering is not perfect, but it is close to the desired signal. The difference might be due to the fact that the noise/reference signal is not completely uncorrelated with the signal of interest. The 3-Hz frequency component is present in the signal of interest, the reference and the noise, so it complicates the task of the adaptive filtering. Figure 17 demonstrates the frequency spectra of the unfiltered signal, the clean (desired) signal and the reference signal. Figure 18 is the spectral plot of the cleaned signal. It is evident from Figure 18 that the noise at frequencies 1 Hz and 5 Hz were significantly reduced, making it much easier to detect the desired signal frequency at 6 Hz, but the 3-Hz component, which is present in both the desired signal and the noise, wasn't retrieved very well. In addition, 2- and 4-Hz components were added after the signal was passed through the filter, which also might be caused by the narrowness of the frequency range.

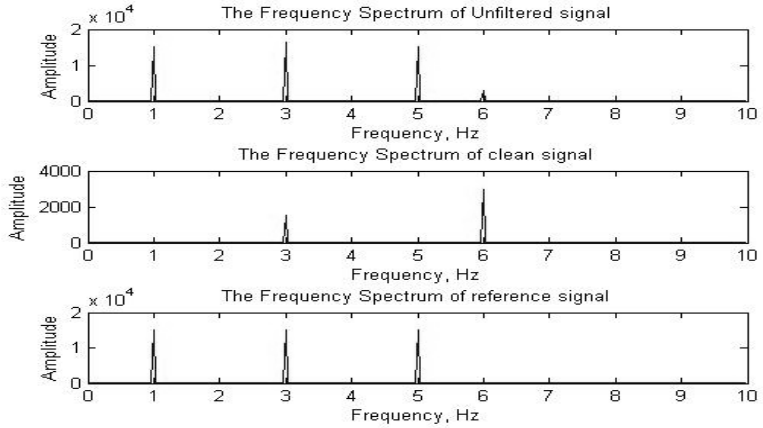

Figure 17: Frequency Spectra of the sinusoidal signals

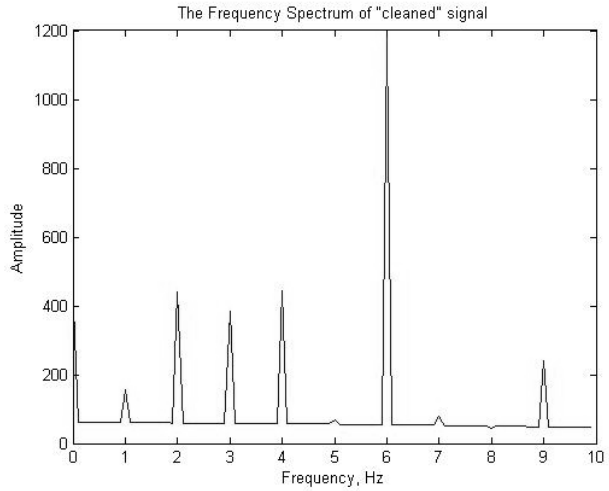

Figure 18: Frequency Spectrum of the "cleaned" signal

Part 2: Time Domain Adaptive Filter

The adjustable parameters for the filter were chosen to be $N = 64$ taps, $M = 10000$ iteration and step size $\mu = 0.007$. Figure 19 is the comparison of the thorax and the thorax signal predicted by the adaptive filter. The amplitude of the predicted thorax was adjusted by the filer to match the scaling of the abdomen signal. The data for thorax was initially in mV and abdomen in μV. Figure 20 is the plots of the unfiltered abdomen and the filtered abdomen. Since 10000 samples were taken it is hard to see if the abdomen was actually filtered well. Figure 21 illustrates the last 2500 samples of the unfiltered and the filtered abdomen signals on one plot.

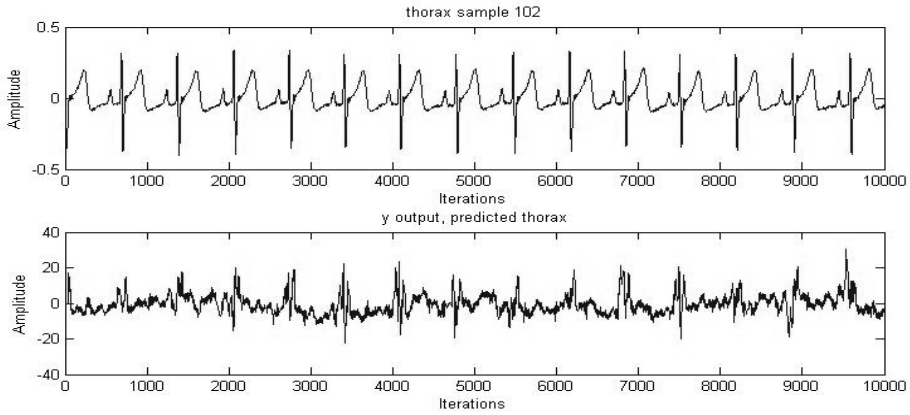

Figure 19: Thorax signals ‘sample_102’

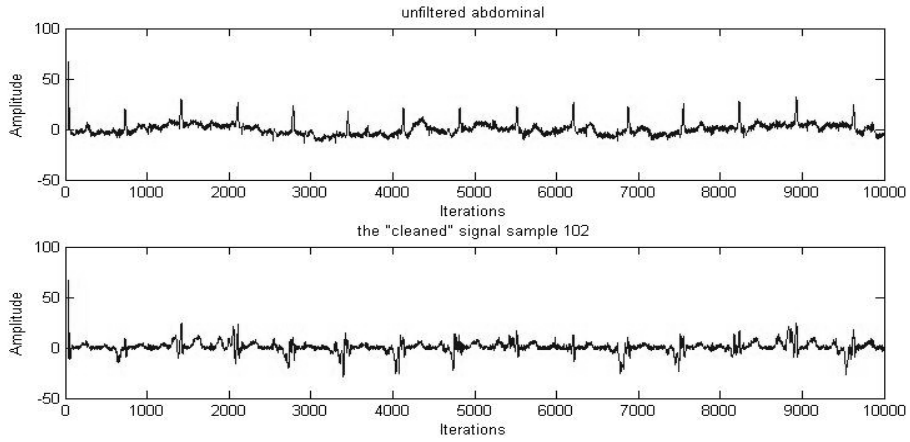

Figure 20: The abdomen signals ‘sample_102’

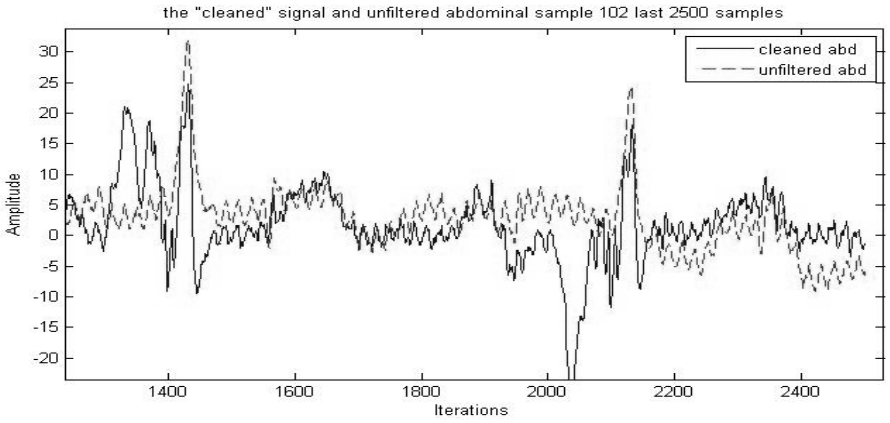

Figure 21: Unfiltered and filtered abdomen signals ‘sample_102’

It is apparent from Figure 21 that contamination is still present in the filtered abdomen signal and it is still hard to extract the possible Fetal ECG signal from it,

but the most recognizable thorax beat is decreased in amplitude, meaning that the time domain adaptive filter is able to detect the thorax component in the abdomen. The next set of figures demonstrated the results for other two samples. Figures 22–24 are for the 'sample_154' for November 16th, the same day as 'sample_102'.

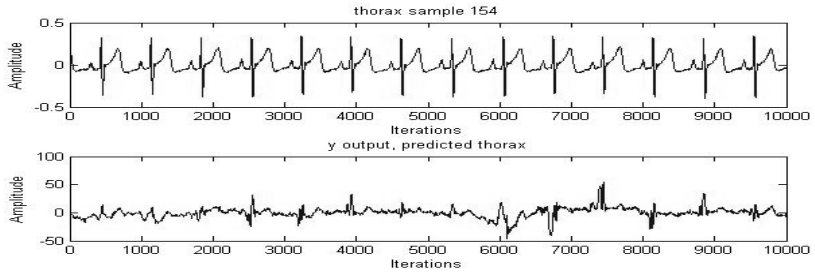

Figure 22: Thorax signal 'sample_154'

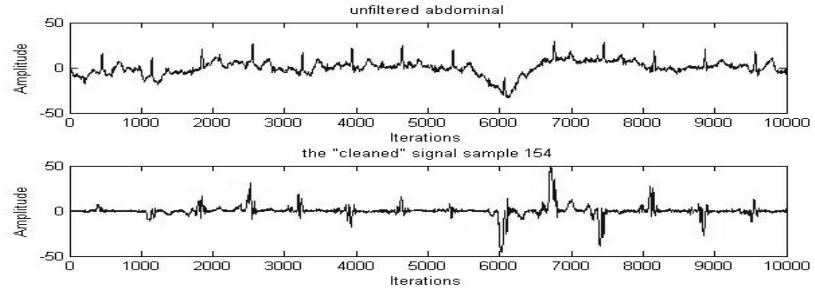

Figure 23: Abdomen signal 'sample_154'

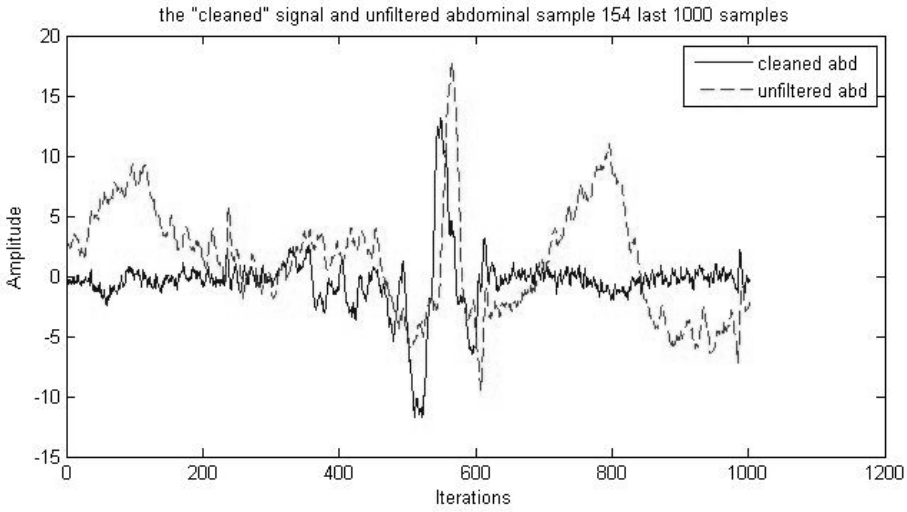

Figure 24: Unfiltered and filtered abdomen signals 'sample_154'

Comparing the results from 'sample_102' and 'sample_154' it is clear that even though the data is only 10 minutes apart, the unfiltered abdomen signals are not identical, thus the filtering results are also different. In both cases the filter

was able to decrease the strong corrupting beats of the thorax signal from the abdomen. However, in both cases the abdomen signal has negative amplitudes added, trying to remove components that were not present in the signal initially. The next set of figures, Figures 25–27, is for 'sample_444' for March 15th.

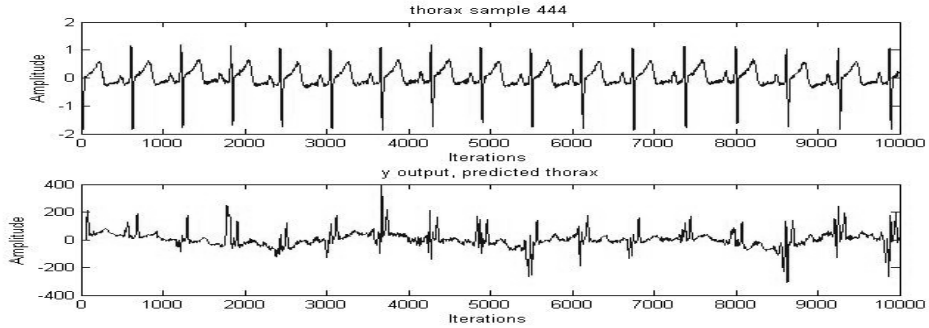

Figure 25: Thorax signal 'sample 444'

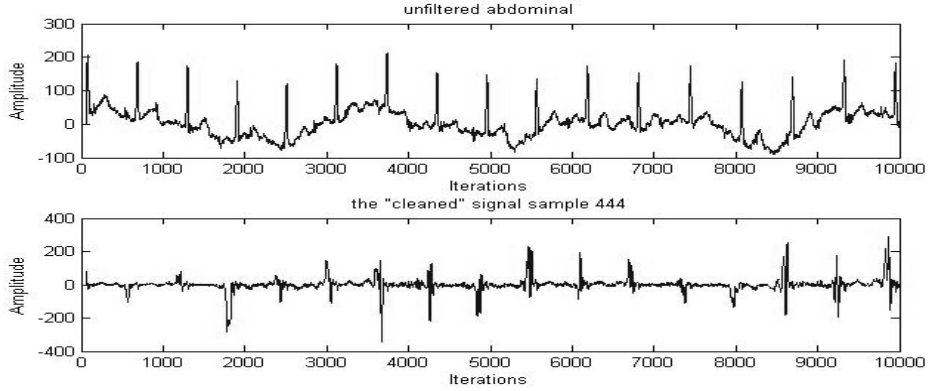

Figure 26: Abdomen signal 'sample_444'

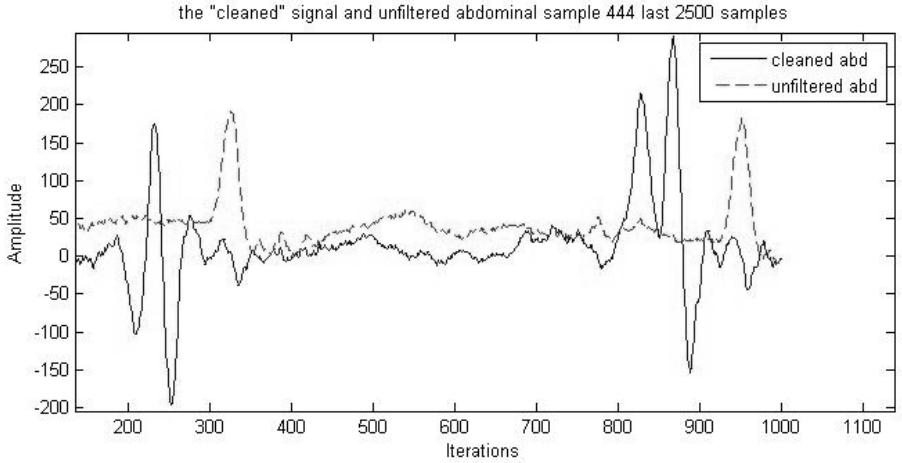

Figure 27: Unfiltered and filtered abdomen signals 'sample_444'

Comparing the results from earlier gestation period to the later gestation period results it is evident that the later abdomen signal contains a stronger thorax-type signal. However, the maternal thorax signal physically is not likely to get stronger, thus as it is discussed in [3] the fetal ECG gains its complexity as the pregnancy progresses, and the fetal ECG becomes more similar to the maternal ECG. As a result, it can be argued that as the fetal ECG becomes more similar to the maternal ECG it is harder for the Time Domain Adaptive Filter to separate a fetal heartbeat from a maternal heartbeat.

Part 3: Transfer Domain Adaptive Filter

The third part of the experiments uses the same input signals as in the second part, and the most productive adjustable parameters for the filter are $N = 8$ taps, $M = 10000$ iterations and step size $\mu = 0.007$. Figures 28 and 29 are the sets of the plots generated during the experiments for a 'sample_102'. Figure 28 shows the last 2000 samples of the reference signal and the output of the filter, it is evident that the output of the filter has the major peaks reversed in sign from the reference signal, but the amplitude was adapted to match the magnitude in the abdomen signal. Figure 29 demonstrates the major peaks being reduced in magnitude compared to the unfiltered signal peaks. The thorax peaks were reduced, but if comparing to the Time Domain (Figure 21) the extra negative peaks were not added after the filtering. Figure 30 shows the results for the 'sample_154', acquired10 minutes later than 'sample_102'.

The results for 'sample_102' and 'sample_154' are different—the filter converged better in the first sample. Even though the samples were taken on the same day, even the same time of the day, the results vary dramatically, which might be caused by the sensitivity of a very weak and low amplitude abdomen signal. Any external variation may distort the signal.

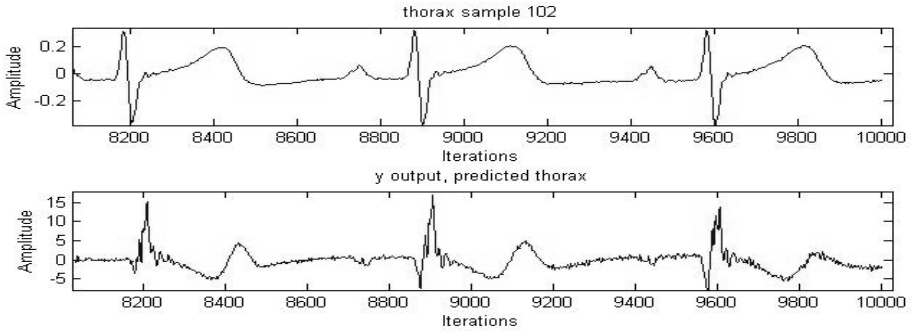

Figure 28: Transform Domain Thorax 'sample_102'

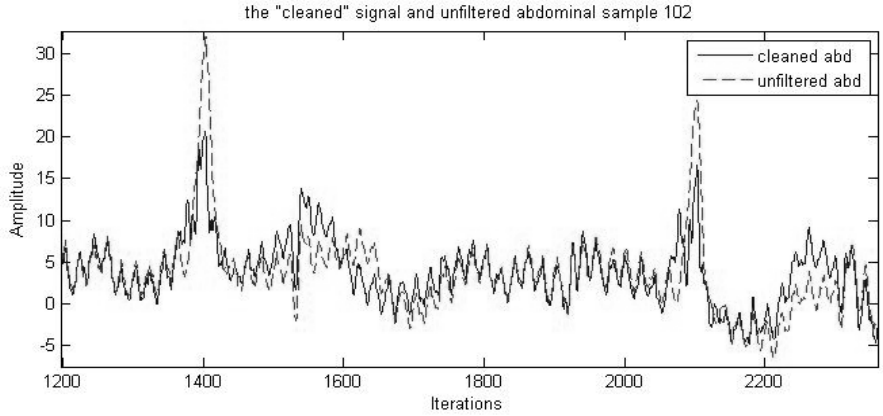

Figure 29: Transform Domain Unfiltered and Filtered abdomen signals 'sample_102'

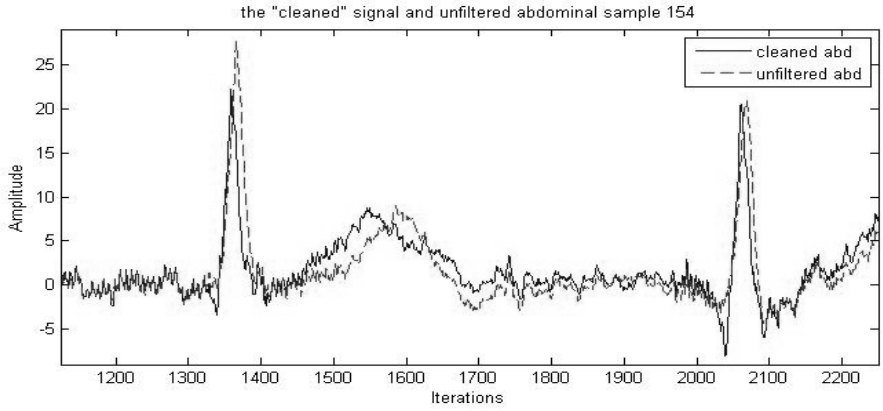

Figure 30: Transform Domain Unfiltered and Filtered abdomen signals 'sample_154'

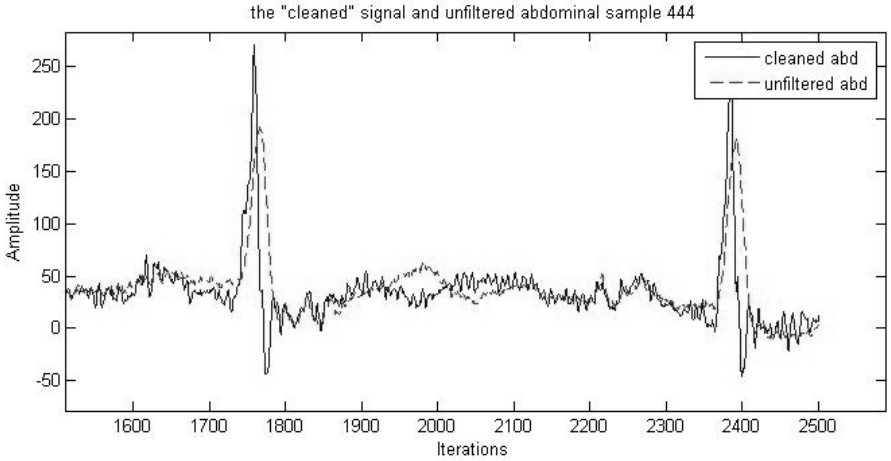

Figure 31: Transform Domain Unfiltered and Filtered abdomen signals 'sample_444'

Figure 31 demonstrates similar data to Figures 29 and 30, but now for a sample recorded 4 months later, 'sample_444'. The filtering results are also different from the results obtained from 'sample_102'. The major peaks are not being decreased in amplitude, but even increased, meaning more contamination is being added to the signal. As it was earlier discussed in the Time Domain Adaptive Filtering, the Fetal ECG gains more complexity, thus complicating the filtering procedure.

DISCUSSION

The results from the preliminary set of experiments helped to get started on implementing the theoretical concept of Adaptive Filtering in practice and see what to expect from the real data. Both Time Domain and Transform Domain filters performed well on removing colored noise from the thorax signal. However, the Transform Domain filter converged faster than the Time Domain filter due to the power normalization of the channels in the frequency domain. After applying the algorithms to real ECG data, the results were different from the expected. The filter didn't remove a significant amount of noise, even though it was able to decrease the amplitude of major peaks. The correlativeness of signals in Adaptive Filtering is one of the main properties that have to be met in order for the filter to successfully extract maximum energy of the signal of interest from the contaminated signal. However, in the case of the thorax and abdomen signals, the exact relationship between the signals is not known, which might be one of the root causes of adaptive filters not being able to detect the noise present in the abdomen signal and subtract it to get the fetal signal. The thorax signal, being used as the reference signal for the adaptive filter is assumed to be caused by the maternal heartbeat, but it might be actually correlated in some way to the signal of interest, the fetal signal. In addition, as it was discussed in [1, 3] there are various sources of interference that are not correlated with the fetal heartbeat, but they might be not present in the thorax reference signal.

Nevertheless, the Adaptive Filter was able to detect and take down the maternal heartbeat amplitude. The Adaptive Filter can be then used as one of the steps in filtering, or several Adaptive filters with different references for every possible source of noise can be used. However, as it was seen from results in the figures for both unfiltered and the filtered signals the filter may distort the original signal, which will lead to more contamination. Having a reference that is well-correlated to the noise contained in the signal, but at the same time not correlated to the signal of interest, is very critical in improving the performance of Adaptive Filtering Techniques.

CONCLUSION

Adaptive Filtering for removing noise from Fetal ECGs with the current data available is not sufficient enough. Time and Transform Domain filters were able to detect maternal heartbeat and reduce its magnitude from Fetal ECG signal. However, additional signal processing is required to attain the desired result.

The variations in data from different times of gestation point out the fact that different techniques for filtering have to be used during various periods of pregnancy. From the experiment results it is evident that the AF was more effective on earlier stages due to the physiological difference of the fetal signal from the maternal signal. As a result, more advanced AF methods can be used for early-stage signal processing, as opposed to some other methods.

The possibility of knowing the nature of the noise gives more chances to successfully train the reference signal to match the noise. Thus, more advanced modeling techniques for predicting the behavior of the ECG signal inside mother's body would enable the fetal signal to be extracted better.

ACKNOWLEDGMENTS

This material is based upon work supported by the National Science Foundation under Grant No. EEC-1062984. Furthermore, I would first like to thank my mentors Professor Kenneth Jenkins and Professor David Salvia for their support and dedication to the project. I would like to thank my grandmother Apen Skabayeva for being my life mentor, parent, and friend.

REFERENCES

[1] Martens, Suzanna M M., Chiara Rabotti, Massimo Mischi, and Rob J. Sluijter. "A Robust Fetal ECG Detection Method for Abdominal Recordings." *Physiological Measurement* 28.4 (2007): 373-88. Print.

[2] Outram, N.J. "Techniques for Optimal Enhancement and Feature Extraction of Fetal Electrocardiogram." *IEE Proceedings - Science, Measurement and Technology* 142.6 (1995): 482. Print.

[3] R. Sameni and G. D. Clifford, "A Review of Fetal ECG Signal Processing; Issues and Promising Directions," *The Open Pacing, Electrophysiology & Therapy Journal (TOPETJ)*, vol. 3, pp. 4-20, November 2010.

[4] Sharma, Yogesh, and Anourag Shrivastava. "Periodic Noise Suppression from ECG Signal Using Novel Adaptive Filtering Techniques." *International Journal of Electronics and Computer Science Engineering* 1.2 (n.d.): 681-85. Print.

[5] B. Widrow, J. Glover, J. McCool, J. Kaunitz, C. Williams, H. Hearn, J. Zeidler, E. Dong, and R. Goodlin, Adaptive noise cancelling: principles and applications, *Proc. IEEE*, vol. 63, no. 12, pp. 1692, 1716, 1975.

[6] Jenkins, William Kenneth. *Advanced Concepts in Adaptive Signal Processing*. Boston: Kluwer Academic, 1996. Print.

[7] Jenkins, Kenneth W., and Daniel F. Marshall. "Transform Domain Adaptive Filtering." *The DSP Handbook*. Ed. C. Radhakrishan. 2nd ed. Boca Raton: CRS, 2010. N. pag.

[8] Goldberger AL, Amaral LAN, Glass L, Hausdorff JM, Ivanov PCh, Mark RG, Mietus JE, Moody GB, Peng C-K, Stanley HE. PhysioBank, PhysioToolkit, and PhysioNet: Components of a New Research Resource for Complex Physiologic Signals. *Circulation* **101**(23):e215-e220 [Circulation Electronic Pages; http://circ.ahajournals.org/cgi/content/full/101/23/e215]; 2000 (June 13).

OBSERVATION OF QUADRUPOLE RESONANCE TRANSITIONS USING A CONTINUOUS-WAVE SPECTROMETER

Jazmyne Claggett,* Jeffrey Schiano,[#] and Xinxing Meng[+]

Department of Electrical Engineering
The Pennsylvania State University, University Park, PA 16802

*Undergraduate Student of
Department of Physics & Engineering
West Virginia Wesleyan College
Buckhannon, WV 26201

ABSTRACT

This study verifies the operation of a continuous-wave (CW) quadrupole resonance (QR) spectrometer by observing known nitrogen-14 transitions in several compounds including hexamethylenetetramine, piperazine, sodium nitrite, and urea. The CW spectrometer measures QR transitions in nitrogen-14 compounds ranging from 500 kHz to 5 MHz, and consists of a marginal oscillator, lock-in amplifier, and a computer-controlled data acquisition system. This study compares spectra acquired with the CW spectrometer against that obtained with a pulsed spectrometer. The basis for comparison is the transition frequency and spectral shape.

INTRODUCTION

Quadrupole Resonance

Quadrupole resonance (QR) spectroscopy is a tool for determining chemical structure and detecting contraband material such as explosives and narcotics [1, 2]. The physical basis for QR spectroscopy is the electrostatic interaction between the electric quadrupole moment tensor of the nucleus and the electric field gradient tensor of the surrounding electronic charges is [3,4]. Quantization of the electrostatic interaction energy, between the quadrupole moment and the electric field gradient tensors, leads to preferred orientations of the nuclei that correspond to specific energy levels. The energy difference, and associated transition frequency, between any two levels is not sharp. Impurities, mechanical strains,

[#] Faculty Mentor
[+] Graduate Mentor

and temperature gradients in a material all lead to a distribution of resonant frequencies characterized by a lineshape.

In nitrogen-14 compounds there are three energy levels that are determined by three parameters. The electric quadrupole moment parameter, *eQ*, characterizes the quadrupole moment tensor by revealing the deviation of the nuclear charge density from spherical symmetry. Two parameters describe the electric field gradient tensor. The largest gradient, *eq*, and the asymmetry parameter, $\eta\ \varepsilon\ [0, 1]$, provide information on the chemical structure. The transition frequencies between energy levels are

$$\nu_{+} = \frac{e^2 qQ}{4h}(3+\eta),\quad \nu_{-} = \frac{e^2 qQ}{4h}(3-\eta),\quad \nu_{d} = \frac{e^2 qQ}{4h}\eta, \tag{1}$$

and range from about 500 kHz to 5 MHz.

The Lorentzian function

$$L(f) = \frac{1}{1+[T_2^*(f-\nu_*)]^2} \tag{2}$$

approximates the lineshape, where ν_* is the transition frequency, and the full-width half-maximum (FWHM) of the transition is

$$FWHM = \frac{2}{T_2^*}. \tag{3}$$

For powdered nitogen-14 samples, the FWHM is typically on the order of 1 kHz.

QR Spectroscopy Techniques

This study uses pulsed and continuous-wave spectroscopy techniques to observe QR transitions. For either technique, a solenoidal radio-frequency (RF) probe contains the sample. Pulsed spectroscopy perturbs the orientation of the quadrupolar nuclei by applying a rotating magnetic field whose frequency corresponds to the energy difference between any two preferred orientations. After switching off the external magnetic field, the nuclei precess about the principal axis of the electric field gradient tensor. The precession of the nuclear magnetic moment induces an exponentially decaying voltage across the RF coil terminals, revealing the presence of the quadrupolar nuclei.

In response to a RF pulse applied at the transition frequency ν_*, a QR transition characterized by a Lorentzian distribution induces an exponentially decaying voltage across the probe coil terminals. The QR receiver demodulates the probe signal to a much lower frequency f_r, resulting in the received signal

$$s(t) = S_o e^{-t/T_2^*} \cos\left(2\pi f_r t\right), \tag{4}$$

which is known as the free-induction decay (FID). The magnitude-squared Fourier transform of the FID has a Lorentzian lineshape centered at f_r.

In a CW experiment, the probe coil is part of a tuned circuit that determines the frequency of an oscillator. As the frequency of the oscillator sweeps across the QR transition lineshape, the amplitude of oscillation decreases as nuclei absorb energy. A lock-in amplifier reveals the change in amplitude. As a function of spectrometer frequency, the lock-in amplifier output represents the derivative of the Lorentzian lineshape [5].

The maximum adsorption of energy occurs when the frequency of oscillation matches the transition frequency and the magnetic field H_1 seen by the nuclei satisfies the constraint

$$\gamma^2 H_1^2 T_1 T_2^* = 1, \tag{5}$$

where γ is the gyromagnetic ratio, which is 1933 rad/sec/gauss for nitrogen-14 [1]. The spin-lattice time constant T_1 characterizes the relaxation of the population levels towards their thermal equilibrium values.

The relationship between the Fourier transform of the pulsed response and CW absorption spectra is analogous to that of the impulse response and the frequency response of a linear system [6]. The primary advantage of CW spectroscopy over pulsed spectroscopy is that it is less expensive to implement. The cost of pulsed spectroscopy is more than ten times greater than the cost of CW spectroscopy, in part because pulsed spectroscopy requires a substantially larger RF magnetic field, which in turn requires high power instrumentation. In contrast, CW spectroscopy experiments require a magnetic field that is small enough not to significantly change the number of nuclei in the different energy levels. Consequently, CW spectrometers are less expensive to construct and maintain. The disadvantage of CW spectroscopy is that takes longer to acquire a signal than a pulse spectrometer owing to a substantially smaller signal-to-noise ratio. Pulse spectrometers generate a larger response as the finite duration of the pulse produces an excitation bandwidth that excites the entire transition lineshape. In contrast, CW spectroscopy uses a monochromatic source that excites only a small fraction of the quadruple nuclei at a given oscillator frequency.

Continuous-Wave Spectrometer

The CW spectrometer in this study uses a marginal oscillator, which is an instrument for revealing small changes in the losses of a harmonic oscillator. Roberts and Rollin credit Pound with developing the first marginal oscillator in the 1940s to observe nuclear magnetic resonance (NMR) transitions within solids [7, 8]. Figure 1(A) shows a conceptual representation of a marginal oscillator that detects QR transitions in solids. The inductance L and capacitance C of the

network determine the frequency of oscillation, while the resistance *R* represents the losses within the network. To maintain a steady-state sinusoidal oscillation, the dependent current source supplies just enough energy to counter these losses. In other words, the dependent current source must appear as a negative resistance with value -*R*, so that the parallel LC network sees an open circuit. Therefore, the dependent current source represents a negative resistance converter (NRC). The overall circuit is a marginal oscillator because the dependent source provides just enough energy to sustain oscillation.

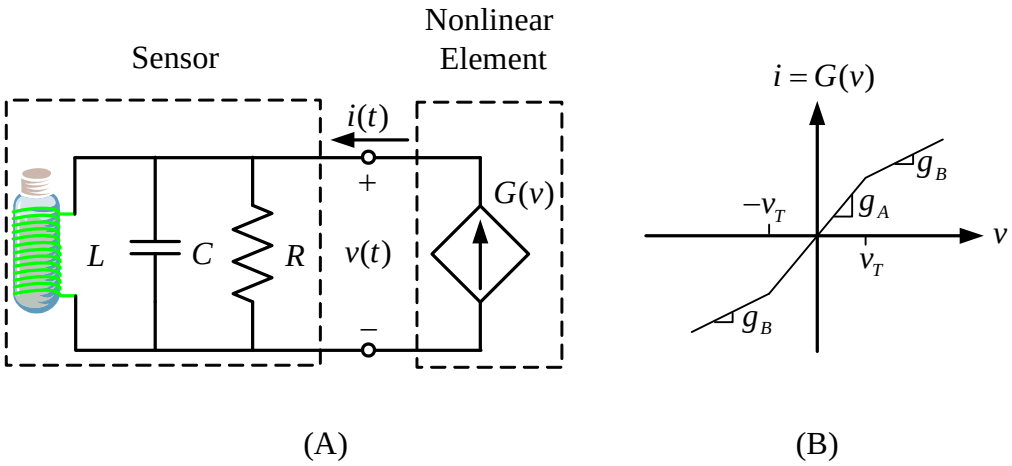

(A) (B)

Figure 1: (A) Marginal oscillator (B) dependent current source *iv* characteristics

When used as a CW spectrometer, the inductor of the tuned circuit surrounds the sample and generates a magnetic field that interacts with nuclei within the sample. When the frequency of the magnetic field approaches a QR transition frequency, the nuclei adsorb energy and as a result, the losses within the tuned RLC network increase. The increase in losses represents an effective decrease in the value of R, and reduces the amplitude of the sinusoidal output voltage *v*(*t*).

The key figure of merit for a marginal oscillator is the conversion gain

$$G_c = \frac{\%\,change\,in\,A}{\%\,change\,in\,R} = \frac{\Delta A/A \times 100}{\Delta R/R \times 100} = \frac{\Delta A}{\Delta R}\frac{R}{A}, \tag{5}$$

which represents the sensitivity of the oscillation amplitude with respect to changes in the losses R. The shape of the nonlinear function *G*(*v*) determines the conversion gain [9,10]. The CW spectrometer in this study uses the function *G*(*v*) shown in Figure 1(B). The slopes g_A and g_B, and the threshold voltage v_T are set to obtain a desired oscillation amplitude and conversion gain [10].

Even for conversions larger than ten, the change in amplitude of oscillation is small compared to the level of thermal noise associated with the bandwidth of the tuned RLC circuit. In order to improve the signal-to-noise ratio when measuring

the change in oscillation amplitude, lock-in detection is used. The output of the lock-in amplifier represents the derivative of the Lorentzian lineshape in Equation (2) [5].

This study is part of a larger research project of which one goal is to develop a low-cost CW spectrometer for cataloging QR transitions in nitrogen-14 compounds. Earlier experimental work shows that the CW spectrometer in this study achieves desired values of conversion gain and oscillation amplitude [10]. So far, however, only one study, using a single compound hexamethylenetetramine, demonstrates that this spectrometer can detect a QR transition [11]. The purpose of this study is to determine if the CW spectrometer can detect transitions in other compounds.

Comparing the CW spectrometer output against the derivative of the lineshape obtained using a pulse spectrometer provides a means for verifying the operation of the CW spectrometer. Two metrics characterize the derivative of the Lorentzian lineshape. The first parameter is the centroid that represents the transition frequency ν_*. The second parameter is the separation

$$\beta = \frac{FWHM}{\sqrt{3}} \tag{6}$$

between the peaks of the derivative of the Lorentzian lineshape [5].

EXPERIMENT DESCRIPTION

The QR nitrogen-14 transitions in hexamethylenetetramine [12], piperazine [13], sodium nitrite [14], and urea [15] form the basis for verifying the operation of the CW spectrometer. For pulsed and CW experiments, separate glass vials contain several grams of each material. While hexamethylenetetramine (HMT), piperazine, and sodium nitrite admit room temperature QR transitions, it is necessary to cool the urea sample in order to observe a transition. For convenience, a liquid nitrogen reservoir maintains the temperature of the urea sample near 77 K. Table 1 shows the expected transition frequencies as well as the sample mass.

Table 1: Sample Properties

Compound	Transition Frequency ν_+ [MHz]	Sample Temp [K]	Sample Mass [g]
HMT	3.308	298	9.0
piperazine	3.016	298	7.8
sodium nitrite	3.600	298	17.4
urea	2.914	77	10.4

A pulsed spectrometer provides measurements of the free induction decay for each compound [16]. A solenoidal coil contains the sample vial. The amplitude of

each magnetic field pulse is 65 gauss, and the pulse duration selection maximizes the amplitude of the FID. Averaging one hundred responses further improves the measurement signal-to-noise ratio. The time between pulses is sufficiently large so that all FID signals have the same amplitude. The squared-magnitude of the Fourier transform of the average FID signal yields the Lorentzian lineshape. Numerical differentiation of the measured Lorentzian lineshape provides an estimate of the expected output of the CW spectrometer. For convenience, we normalize the peak amplitude of the expected CW response to unity as only the centroid and peak separation is of interest in this study.

The analysis, design, and operation of the CW spectrometer appear in earlier reports [10, 11]. Prior to each experiment, the user sets several parameters for the marginal oscillator and lock-in amplifier as shown in Table 2. Using relays to manually select capacitors to place in parallel with the sample probe, the user sets the center frequency of the sweep range. An electrically controlled varactor diode sweeps the frequency of the marginal oscillator across the transition lineshape. To achieve a desired frequency span, the user determines the range of voltages to apply to the varactor.

For lock-in detection, a second varactor diode modulates the oscillator frequency using a square-wave waveform. Let $f(t)$ denote the instantaneous frequency of the spectrometer, f_o the frequency at a particular point within the sweep range, f_{lock} the frequency of lock-in detection, and f_d the frequency dither in the oscillation frequency so that

$$f(t) = f_o + f_d \sin(2\pi f_{lock} t). \tag{7}$$

The user chooses the lock-in frequency as well as the dither frequency. The user sets the dither frequency by specifying the amplitude of the square-wave modulation signal.

The user sets the oscillation amplitude and conversion using two multi- turn potentiometers that adjust the parameters $g_{A,}$ and v_T of the NRC. Using nominal values of T_1 and T_2^*, we set the amplitude to approximately satisfy Equation (1). We use Equation (5) to estimate the conversion gain by modulating the losses of the tuned RLC network using a calibration circuit, and measuring the resulting change in oscillation amplitude.

The slope and time constant of the lock-in amplifier determine the signal-to-noise ratio of the CW spectrometer measurement. The time-constant determines how long the spectrometer must dwell at each frequency within the sweep range. The lock-in amplifier uses a finite-impulse response (FIR) low pass filter whose output reaches steady-state in two time constants for each factor of 6 dB per octave in the filter slope. For example, using a time constant of 50 s and a slope of 12 dB per octave requires a dwell time of 200 s. Correspondingly, a sweep containing 100 points requires 20,000 s, or approximately six hours to complete.

Table 2: Experiment Parameters

Marginal Oscillator	
Center frequency	ν_*
Sweep span	10 kHz
Number of points per sweep	100
Dwell time per point	200 s
Dither frequency	180 Hz
Conversion gain	12

Lock-In Amplifier	
Slope	12 dB
AC gain	40 dB
Sensitivity	1 mV
Time constant	50 s
Lock-in frequency	100 Hz

EXPERIMENT RESULTS

Figures 2 through 5 show the results for hexamethylenetetramine, piperazine, sodium nitrite, and urea, respectively. Each figure shows three plots. The left plot shows the average free-induction signal generated using the pulsed spectrometer. The middle plot shows the magnitude-squared Fourier spectra of the free induction decay, or equivalently, the Lorentzian line shape. The right plot shows the expected and measured response of the CW spectrometer. The solid curve shows the expected response which represents the derivative of the measured Lorentzian lineshape, while the dashed curve shows the output of the lock-in amplifier as a function of spectrometer frequency. We normalize the expected and measured responses so that the peak amplitude is unity. To compare the spectral shapes, we shift the curves along the frequency axis to center the transitions.

Table 3 shows a summary of the results. The second and third columns show the measured transition frequency using pulsed and CW spectroscopy, respectively. The fourth column indicates the full-width half-maximum (FWHM) obtained from the free-induction signal spectra. Columns five and six show the peak separation β defined in Equation (7), obtained from the expected and measured CW output, respectively.

Table 3: Measured Transition Parameters

Compound	**Transition Frequency [MHz]**		**Linewidth FWHM [Hz]**	**Peak Separation β [Hz]**	
	Pulsed	**CW**		**Estimated**	**Measured**
HMT	3.3092	3.3075	1002	793	544
piperazine	3.0157	3.0155	570	525	734
sodium nitrite	3.5983	3.6021	470	394	625
urea	2.9146	2.9167	715	433	1013

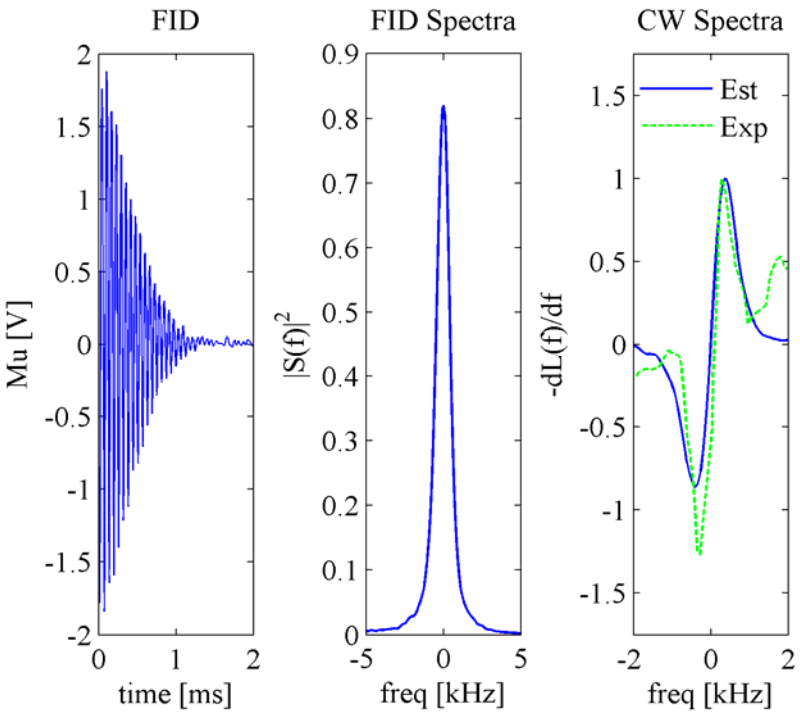

Figure 2: Hexamethylenetetramine data

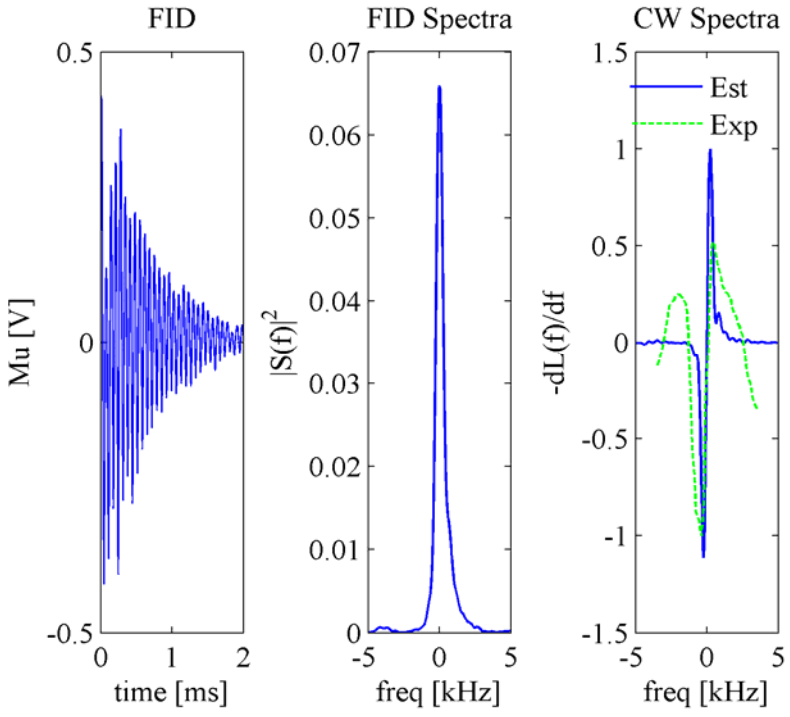

Figure 3: Piperazine data

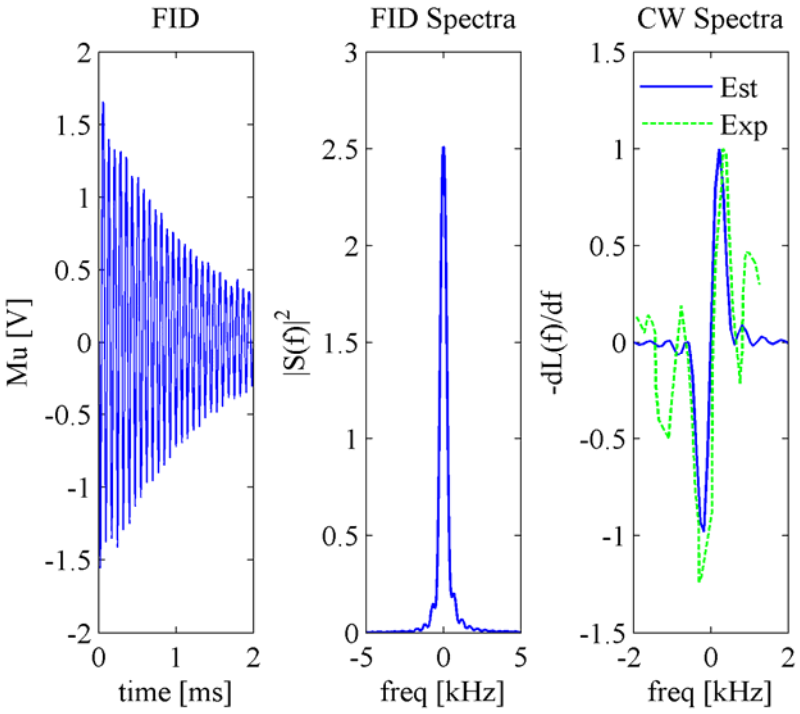

Figure 4: Sodium nitrite data

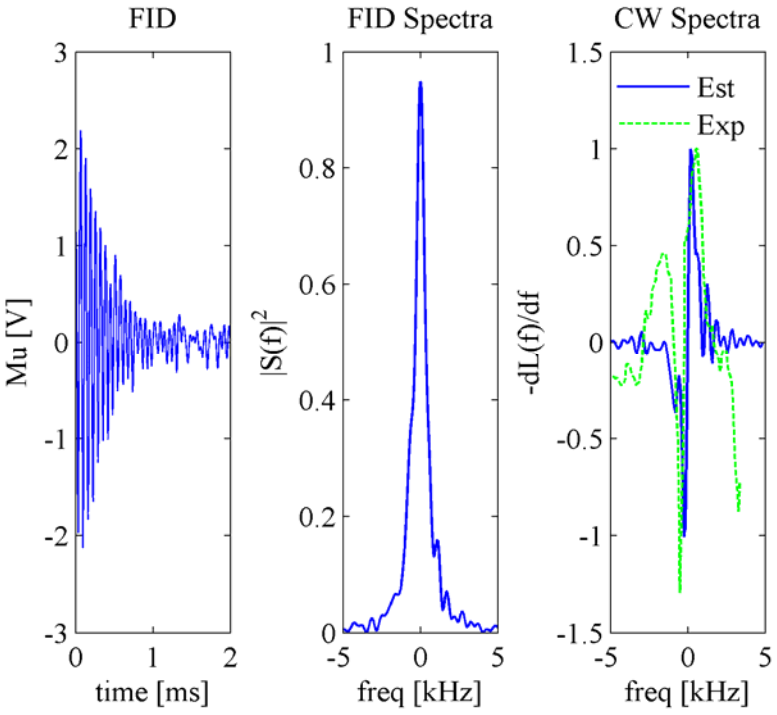

Figure 5: Urea data

DISCUSSION

The transition frequency and peak separation in the CW spectra are the two metrics for verifying the performance of the CW spectrometer. As reference, a pulse spectrometer provides an independent measure of both these parameters. The results in Table 3 show that transition frequency revealed by the CW spectrometer is typically within 2.8% of that observed using the pulsed spectrometer. In contrast, the predicted and measured peak separations are not in good agreement, with percent errors ranging from 32% up to 133%. Further work is necessary to determine the cause of these discrepancies. Despite the error in peak separation, the right-most plots in Figures 2 through 5 show that the shape of the CW spectrometer output is similar to that predicted using pulsed spectroscopy data.

Experiment implementation reveals several aspects of the system that can be improved. First, we observe that changes in threshold voltage affect the conversion gain. From theory, the threshold voltage v_T, should only effect the oscillation amplitude [10]. The effect of threshold voltage on conversion gain is an artifact of the existing NRC circuit design [17]. In particular, varying the threshold voltage on the diodes that implement the knee in the dependent current source *iv* characteristics in Figure 1(B) also varies the dynamic resistance of the diodes, which in turn affects conversion gain. Replacing the diodes in the NRC circuit with precision rectifiers employing high-speed operational amplifiers may reduce the undesirable coupling between oscillation amplitude and conversion gain when adjusting the threshold voltage.

Another aspect of the experiment warranting improvement is the time-intensive protocol for setting varactor voltages and measuring conversion gain. It would be simpler for the user to enter a start and stop frequency for the scan, and have the software controlling the experiment determine the necessary range of control voltage for the varactor diodes. Additionally, conversion gain measurement requires setting a function generator to modulate the calibration circuit and measuring the resulting change in oscillation amplitude using an oscilloscope. Automation of conversion gain measurement will simplify and shorten the setup procedure.

CONCLUSION

The results of this study verify that the CW spectrometer is capable of detecting QR transitions in several different nitrogen-14 compounds. While the CW spectrometer provides a reasonable good measure of transition frequency, the peak separation in the CW spectrometer output is not consistent with that predicted from pulsed spectrometer data. The reason for this discrepancy is unknown and should be determined. An implicit advantage in this study is knowledge of the QR transitions. For each of the four compounds, we center the sweep range on the transition frequency. Following improvements to automate the setup of the CW spectrometer, a follow-up study should test the ability of the CW spectrometer to detect an unknown transition by sweeping over a much larger

range. As it is possible to predict QR transitions to within about 50 kHz using the Townes and Dailey approach [18], the CW spectrometer needs to detect an unknown transition located within a 100-kHz span.

ACKNOWLEDGMENTS

This material is based upon work supported by the National Science Foundation under Grant No. EEC-1062984, Furthermore, I would first like to thank my mentor Dr. Schiano for his time and patience with myself and the project. I would also like to thank Penn State for selecting me for the research program. Finally, I would like to thank my family and friends for all of their support.

REFERENCES

[1] Das, T.P. and E.L. Hahn, Nuclear Quadrupole Resonance Spectroscopy, Academic Press Inc., New York, 1958.

[2] Garroway, A.N., M.L. Buess, J.B. Miller, B.H. Suits, A.D. Hibbs, G.A. Barrall, R. Matthews, and L.J. Burnett, "Remote Sensing by Nuclear Quadrupole Resonance," IEEE Transactions on Geoscience and Remote Sensing, 39 (6) 1108-1118 (2001).

[3] Dehmelt, H.G., "Nuclear Quadrupole Resonance," American Journal of Physics, 22(3)110-120(1954).

[4] Smith, J.A., "Nuclear Quadrupole Resonance Spectroscopy," Journal of Chemical Education, 48 (1) 39-49 (1971).

[5] Schmitt, C.E., "*Comparison of Blind and Data-Dependent Search Algorithm Performance in Continuous-Wave Quadrupole Resonance Spectroscopy*," Schreyer Honors Thesis, Pennsylvania State University, 2007.

[6] Lowe, I.J. and R.E. Norberg, "Free-induction decays in solids," Physical Review, 107(1) 46-61,(1957).

[7] Roberts, A., "Two New Methods for Detecting Nuclear Radio Frequency Absorption," The Review of Scientific Instruments, 18 (11) 845-848 (1947).

[8] Rollin, B.V., "Nuclear Paramagnetism," Reports on Progress in Physics, 12 (1) 22-33 (1949).

[9] Viswanathan, T.L., T.R. Viswanathan, K.V Sane, "Study of Marginal Oscillator Behavior," IEEE Transactions on Instrumentation and Measurement, IM24 (1) 55-61 (1975).

[10] Tyson, T. J., *Marginal Oscillator Conversion Gain: Prediction, Simulation, and Experimental Measurements*," M.S. Thesis, Department of Electrical Engineering, Pennsylvania State University, State College, PA, 2011.

[11] Wilson, L., J.L. Schiano, and T. Tyson, "Verification of a Marginal Oscillator for Continuous- Wave Quadrupole Resonance Spectroscopy," NSF EE REU PENN STATE Annual Research Journal, 9, Edited by S. Bilén (2011).

[12] Alexander, S., A. Tzalmona, "Relaxation by Slow Motional Processes. Effect of Molecular Rotations in Pure Quadrupole Resonance," *Physical Review*, 138(3A)A845-A855(1965).

[13] Tzalmona, A., "Measurements of ^{14}N Quadrupole Interaction and Motional Processes in Piperazine," Physics Letters, 20(5)478-479(1966).

[14] Oja, T., R.A. Marino, P.J. Bray, "^{14}N Nuclear Quadrupole Resonance in the Ferroelectric Phase of Sodium Nitrite, Physics Letters, 26A(1)11-12(1967).

[15] Chiba, T., M. Toyama, Y. Morino, "Nuclear Quadrupole Resonance Spectra of ^{14}N in Urea Crystals," Journal of the Physical Society of Japan, 14(3)379-380(1959).

[16] Schiano, J.L. and M.D. Ginsberg. "A Pulsed Spectrometer Designed for Feedback NQR." Zeitschrift fur Naturforschung, 55a(1)61-66(2000).

[17] Tricou, B., "*Analysis, Design, and Synthesis of a Negative Resistance Converter for a Marginal Oscillator*," Schreyer Honors Thesis, Pennsylvania State University, 2011.
[18] Townes, C.H. and B.P, Dailey, "Determination of Electronic Structure of Molecules from Nuclear Quadrupole Effects," The Journal of Chemical Physics, 17(9)782-796(1949).

CHARACTERIZATION OF POROUS SILICON FOR MICROPYROTECHNIC APPLICATIONS

Alfredo Bermúdez Lozada,[*] Srinivas A. Tadigadapa,[#] and Venkata Sharat Parimi[+]

Department of Electrical Engineering
The Pennsylvania State University, University Park, PA 16802

[*]Undergraduate Student of
Electrical and Computer Engineering Department
Universidad Del Turabo
Gurabo, PR 00778-3030

ABSTRACT

The high reactivity of nanoscale composites can be exploited to form a new class of energetic materials known as nanoenergetic materials. Porous silicon (PS) is a nanoenergetic material that can store more energy than conventional energetic materials and can be used in innovative ways to tailor the release of this energy. This material attracts the attention of many researchers due to the possibility of developing PS based devices. Due to its high energy density, PS can be integrated into microscale devices as an on-board energy source and such integration is known as micropyrotechnics. Porous silicon is formed by electrochemical dissolution of selective atoms in hydrofluoric acid based electrolytes, which results in high surface areas ~1000 m^2/g. The pore morphology is strongly affected by the etch parameters such as electrolyte composition, current density, etch duration and also the substrate properties such as dopant type and concentration. The changes in the porous structure strongly affect the reactive properties of energetic composites formed. Flame propagation speeds were found to be up to three orders of magnitude due to the variation in the porous structure. The goal of this project is to etch and characterize the porous layers formed on substrates with different dopant types and concentrations. This information will be used to adjust the etch parameters to yield samples with specific porous layer structure which will enable a parametric study of the flame propagation to understand the important physical effects and help formulate models to explain how the propagation rates can be tuned.

[#] Faculty Mentor
[+] Graduate Mentor

INTRODUCTION

Energetic materials (EMs) are a class of materials which have desirable characteristics such as high energy density and rapid energy release properties. These materials such as explosives, propellants and pyrotechnics are widely used for civilian and military applications. The current drive toward miniaturization of devices, aimed at improving their performance and efficiency brings forth several new problems, due to the length scales involved. Most of the conventional actuation methods are either inefficient or impractical to integrate at such length scale [1], requiring new actuation methods and energy sources. This problem can be overcome by the integration of energetic materials as on-board energy sources for microscale devices and this integration is known as micropyrotechnics [2]. Micropyrotechnics can be defined as the integration of an energetic material into a multi-functional microsystem, and the exploitation of the thermal, mechanical and chemical energy released by decomposition.

The urgency and interest of such systems will continue to increase with the development of portable microsystems. The most suitable method for micropyrotechnic applications is to use materials with nanoscale features to form energetic composites, and these new materials are known as nanoenergetic materials (nEMs). One such nEM of interest is porous silicon (PS), which has the ability to store more energy than conventional energetic materials. PS is essentially bulk silicon with missing crystal atoms, which result in the formation of nanoscale pores in the silicon substrate. These nanoscale pores result in very high specific surface areas (up to 1,000 m^2/g), which result in highly reactive unsaturated surfaces which can be exploited to form energetic composites. Due to its high energy density, porous silicon can be integrated into microscale devices as an on-board energy source. Another important advantage of PS is that their base material is silicon (Si). Silicon has been the most widely used material with miniaturization purpose, not only due to their appropriate physical and chemical properties, but also to the degree of development of their associated technologies.

Porous silicon is not a new material. In 1956, Arthur Uhlir accidentally discovered the porous silicon, while searching for an electrochemical method for machining silicon [3]. This discovery received very little attention until 1990, when it was discovered that both micron and nano PS could emit visible light with the possibility to improve light emitting diode and chemical sensor technology. The first report about the enhanced chemical reactivity of PS was by McCord et al. [4] who observed that. PS created an audible pop upon contact with nitric acid and dissolved rapidly in aqueous sodium hydroxide solutions. The highly energetic nature of PS was discovered in 2001, when a team of scientists at the Technical University of Munich inadvertently discovered that hydrogenated porous silicon reacts explosively with oxygen at cryogenic temperatures, releasing much energy as an equivalent amount of TNT [5]. In addition, numerous groups have found that various oxidizing agents are capable of producing strong explosive reactions [6–7]. These agents typically include sodium perchlorate, sulfur or potassium nitrate.

Nano-porous silicon has been fabricated by a variety of different methods. The most common fabrication technique of porous silicon is electrochemical dissolution of a crystalline silicon wafer in hydrofluoric acid-based solutions [8]. PS has extremely rich morphological features and the formation process of PS is a very complex function of numerous factors. The silicon wafer serves as the anode during the electrochemical dissolution and the cathode is made of platinum or any HF-resistant metal. The formation condition for PS can be best illustrated by *J-V* curves. Figure 1 shows the region in which electrochemical dissolution of silicon in HF electrolytes occurs.

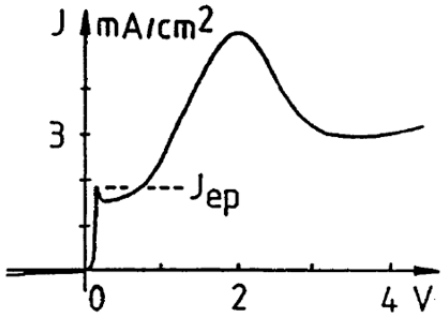

Figure 1: *J–V* curve of porous silicon in dilute aqueous HF solution [8].

The formation of pores begins during the initial rising part of the curve, for a potential value below the potential of the first sharp peak known as electropolishing peak. Porous silicon morphology has been divided into three categories based on the size of its pores; microporous (pore size ≤ 2 nm), mesoporous (pore size 2–50 nm) and macroporous (pore size > 50 nm). For n-type large amount of pores are generated by illumination or when relatively high anodic potentials are applied [8]. Making porous silicon demands specific sets of parameters and some control of the etching process. The condition under which PS is fabricated has a large effect on the structure of porous layers. These conditions include:

1. Effect of illumination
2. Electrolyte composition
3. Duration of etch process
4. Current density
5. Substrate dopant type and concentration

The formation of porous silicon is accompanied by the evolution of hydrogen at the anode. The efficient removal of the hydrogen bubbles formed is important to ensure stability and uniformity of the porous structure. When purely aqueous HF is used as the electrolyte, the bubbles stick to the surface and create non

uniformity and may lead to cracking of the porous layer. This can be avoided by using surfactants to reduce the surface tension of the solution which allows the bubbles to leave the surface sooner. Several solvents can be used to accomplish this, such as ethanol, acetic acid, and commercial surfactants. The preferred electrolytes according to the extensive literature on PS are typically aqueous HF and ethanol mixtures. For a given current density, the pore diameters and porosity reduce with increasing HF concentrations in the electrolyte. The thickness of the porous layers increase with the etch duration. The porosity increase with increasing current density and decreases with an increase in the concentration of HF in the electrolyte.

The reactive properties of the energetic composites formed from PS depend on the pore diameters, thickness and structure of the porous layers and the deposition of the oxidizer within the pores, which again is controlled by the porosity and the pore diameters. To achieve the highest energy density on the smallest area the layer has to be as thick as possible and the porosity has to be adjusted to achieve a stoichiometric mixture with oxidizing molecules. A stoichiometric mixture is the mixture of fuel and oxidizer that can react to give products with no excess reactants. For example, an ideal fuel/air mixture in which both the fuel and the oxygen in the air are completely consumed is called stoichiometric mixture. These porous layers were impregnated with various oxidizers to observe the interaction between the filling efficiency, the increased surface areas and the reactivity from reduction of pore diameter.

EXPERIMENTAL METHODS

The electrochemical anodization is the most common method for preparation of nanoporous silicon. Etching of silicon wafer was done inside a cell composed of two parts, and fabricated from Teflon, a HF resistant material. The cell consists of a Teflon O-ring to prevent leakage of the electrolyte, and is designed to expose only one side of the silicon wafer to the electrolyte. The silicon wafer is positioned between the two plates, which are held together using long screws. The upper plate contains an open cavity in the center which exposes only the top side of the silicon wafer to the electrolyte as shown in Figure 2.

Figure 2: Single-cell set up for etching porous silicon.

The silicon wafer acts as the anode during the etch process, and a uniform electrical contact was established on the back side of the wafer using an aluminum foil. A silver mesh was used as the cathode, and this mesh rest on the groove provided in the etch cell, to ensure that the mesh always stays at a fixed distance from the wafer to avoid non uniformities. The etching was carried out at a constant current using an Agilent DC power supply, capable of providing current up to 6 amperes in a constant current mode. The common electrolyte used in the etch process consist of a 1:1 mixture of 49% hydrofluoric acid and ethanol. After the formation of highly porous or thick PS sample, when the solution is allowed to evaporate out the pores, a cracking of the layer is systematically observed. To avoid the cracking, the wafer should be cleaned with ethanol and dried under a gentle stream of nitrogen. The etched porous layers were also rinsed with Pentane to further stabilize the porous layers.

Then, the porous layers etched were characterized by measuring their porosity, thickness and surface area. The porosity and thickness of the etched PS was estimated using gravimetric methods [8]. The silicon wafer is weighed before anodization (M_1), and then is weighed after anodization (M_2). After anodization the sample is scribed on the backside using a diamond tip scribe and cleaved into smaller pieces. Selected samples from the scribed wafer are weighed again (m_2) and then the porous layers were dissolved in a 1-M aqueous NaOH solution. The surface of the sample was wetted with methanol to ensure rapid dissolution of the porous layers. The porous layers were found to completely dissolve in the NaOH solution in 1–4 minutes. The end point for the dissolution was marked by cessation of the hydrogen bubbles evolving from the surface. The dissolution of PS in NaOH is described by the chemical equation shown below:

$$Si + 2NaOH + 4H_2O \rightarrow Na_2Si(OH)_6 + 2H_2$$

After dissolving the porous silicon layer the samples are weighed again (m_3). The mass of these pieces before etching (m_1) was estimated based on their mass, M_1, M_2 and the total area of the wafer and the area exposed to the electrolyte. The porosity is given simply by the following equation.

$$P = \frac{m_1 - m_2}{m_1 - m_3}$$

Using the previous masses it is also possible to obtain the thickness of the layer. The thickness is measured gravimetrically using the following equation

$$W = \frac{m_1 - m_3}{S \times d}$$

where d is the density of massive silicon and S the area of the etched region.

The pore diameter and the specific surface area were determined by scanning electron microscope (SEM) images and the Brunauer–Emmet–Tellet (BET) method respectively. The SEM images indicate the pore diameter and the porous layer thickness. On the other hand, BET measurements provide the specific surface area of the PS sample. The wafer was scribed into several sample strips, each approximately 5 mm wide. These sample strips were impregnated by the oxidizer by soaking them in solutions of the oxidizer in methanol for several hours. Since the oxidizers used in this study (sodium/magnesium/calcium perchlorate) are extremely hygroscopic, the oxidizer impregnation was carried out by storing in a box continuously purged with dry nitrogen to maintain a very low humidity. The energetic composites prepared were mounted on a sample holder inside a test chamber. The test chamber was the evacuated to −90 kPa (g) and the samples were heated to drive off the methanol and create energetic composites. The chamber was then back-filled with argon, and the samples were ignited using a 200-W continuous wave CO_2 laser (10,400 nm). The flame propagation speeds were determined by recording the propagation using a high speed camera (Phantom V 7.3) at 60,000–100,000 fps. A single time integrated (50-ms) spectrum was collected (using an Ocean optics HR-2000 spectrometer), which was processed using a multiwavelength pyrometry algorithm [9] to estimate the temperature of the flame.

One of the most important attributes of the energetic composited formed using PS is the amount of fuel (PS) and the oxidizer, which is deposited within the pores. Sufficient amount of oxidizer must be deposited within the pores to obtain the maximum amount of energy from the composited. However, studying the oxidizer deposition within the pores is a difficult task, as the PS samples become extremely sensitive to friction upon the deposition of the oxidizer. Any attempts to manipulate the samples after oxidizer impregnation can result in unintentional ignition of the samples resulting in an explosive reaction. Thus, the salt deposition within the pores was characterized by depositing a non-reactive surrogate salt with which has solubility in methanol comparable to that of perchlorates. A literature survey of various inorganic compounds revealed that cobalt chloride ($CoCl_2$) can be used for this purpose, which was used to quantify the fill efficiency of the salt deposition in the pores.

These strips were weighed (W_1), and then soaked in $CoCl_2$ solutions with known concentrations of the salt. Assuming that the void space within the sample is completely filled with the methanol-$CoCl_2$ solution, the maximum amount of the salt that can be deposited after the solvent is evaporated is $\delta \times V$, where δ is the amount of salt in solution and V is the void space in the PS sample. Thus, the fill efficiency (η) is given by,

$$\eta = \frac{W_2 - W_1}{\delta \times V}$$

where W_2 is the weight of the samples after heating on a hot plate to evaporate the solvent. The surfaces of the samples were carefully cleaned with a soft wipe to remove salt residues on the surface which can introduce errors before weighing.

RESULTS AND DISCUSSION

The silicon wafers were etched at several different etch parameters to form thick and stable porous layers. As the etch duration increases, the porosity and the thickness of the etched PS increase, which causes the PS to peel off the surface, rendering the samples unsuitable for further experiments. This, a parametric study was carried out to yield etch recipes for forming thick and stable porous layers demanded by the flame propagation studies. Four different kinds of substrates were etched, to study the effect of substrate doping on the structure of PS formed and its effect on the flame propagation speeds, which directly correspond to energy release rates.

The four different kinds of substrates used to etch PS were heavily doped p- (boron) and n- (arsenic) doped substrates with resistivity between 0.001–0.005 Ω-cm, low doped p (boron) substrates with resistivity between 10–20 Ω-cm and low doped n-type substrates (phosphorous) with resistivity between 2–5 Ω-cm. The heavily doped substrates were found to always yield smooth surfaces. The low doped n-type substrates were etched under illumination, and they were found to always result in samples with a random micro-crack pattern as shown in Figure 4. A 20-nm-thick layer of titanium was deposited in the backside of the low doped p-type wafers followed by a thermal anneal in an inert atmosphere using a rapid thermal anneal (RTA) furnace to establish backside electrical contact with the wafers. These low doped p-type substrates resulted in non-uniform porous layers, with a part of the wafer showing a micro-crack pattern. The porosities of the low doped substrates were not determined gravimetrically, since the micro-crack pattern makes the gravimetric porosities unusable. The porosities and thicknesses calculated for heavily doped p and n type wafers and the corresponding etch parameters are shown in Table 1. The SEM images representative of heavily doped p-type substrates are shown in Figure 3. High magnification images of the pore surface indicate pore mouth diameter ~30 nm and side view shows porous layers 140 μm thick. The SEM images of low doped p- and n-type samples showing the random micro-crack pattern during the electrochemical dissolution are shown in Figure 4.

These prepared PS samples were impregnated with an oxidizer and the flame propagation speeds were estimated as described in the previous section. A series of images showing the flame propagation are shown in Figure 5. The flame propagation speed was estimated to be 4.09 m/s for this sample by means of an *x-t* trace from the high speed video, as shown in Figure 6.

Table 1: Electrochemical etch parameters, porosity and thicknesses calculated for heavily doped p and n type substrates etched with an electrolyte composition of 1:1 49% HF - Ethyl alcohol.

Type	Resistivity (Ω cm)	Current Density (mA cm^{-2})	Time (min)	Porosity (%)	Thickness (μm)
p	0.001 - 0.005	40	90	59.36	132.08
p	0.001 - 0.005	40	95	59.67	164.74
p	0.001 - 0.005	60	90	63.94	210.81
p	0.001 - 0.005	60	90	71.38	170.78
n	0.001 - 0.005	40	60	51.95	139.15

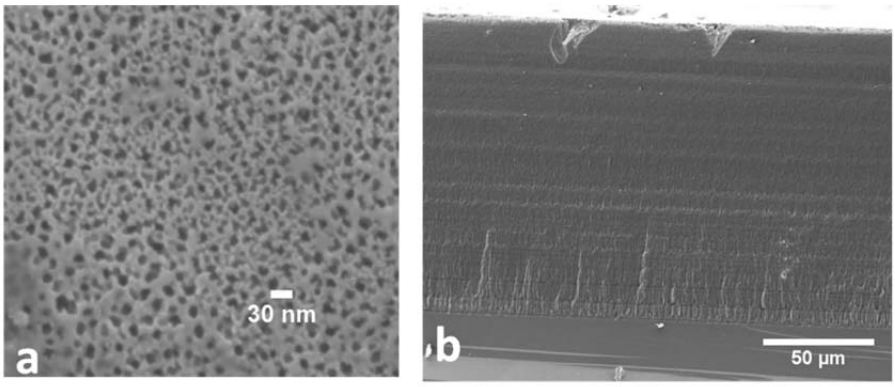

Figure 3: (a) Top view of the porous layer showing pores with diameters ~30 nm. (b) Low magnification side view showing bulk silicon with porous layer on the top. The thickness of the porous layer is 140 μm.

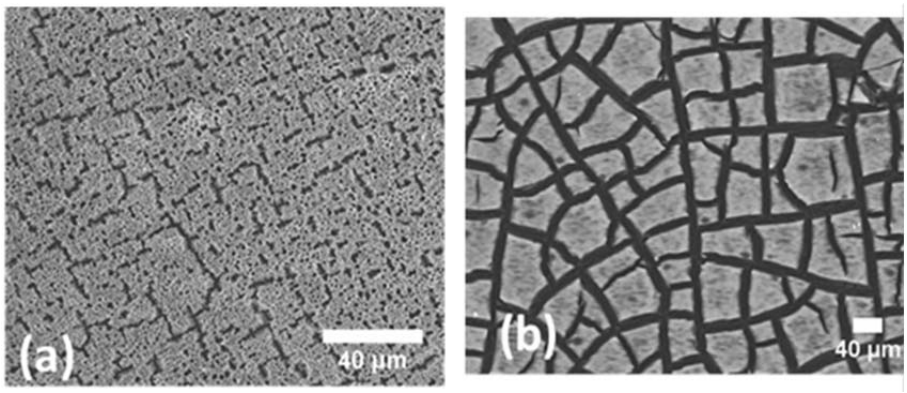

Figure 4: Top view of porous layers etched on low doped n-type substrates (a) and low doped p-type substrates (b) showing the random micro-crack pattern formed during the electrochemical dissolution process. The low doped p-type substrates resulted in non-uniform porous layers with micro-crack structure shown in (b) at some regions and uniform layers elsewhere.

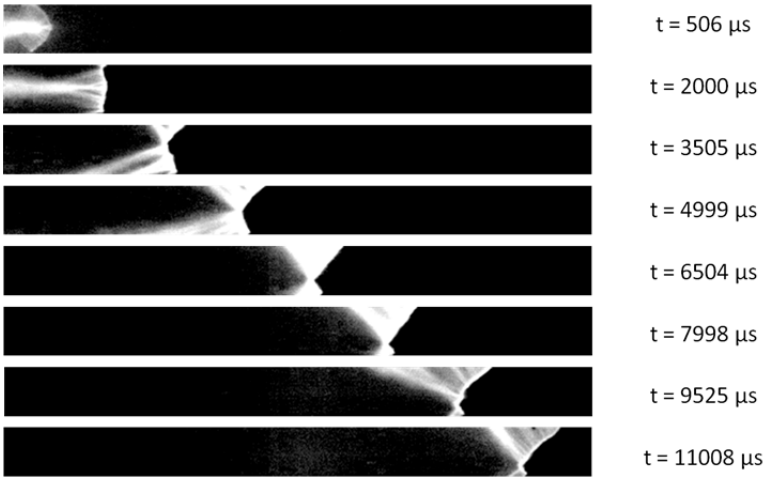

Figure 5: Images from a high speed video showing the flame propagation. The time stamps indicate time elapsed from the first frame, captured at 93023 fps with an exposure of 8 µs.

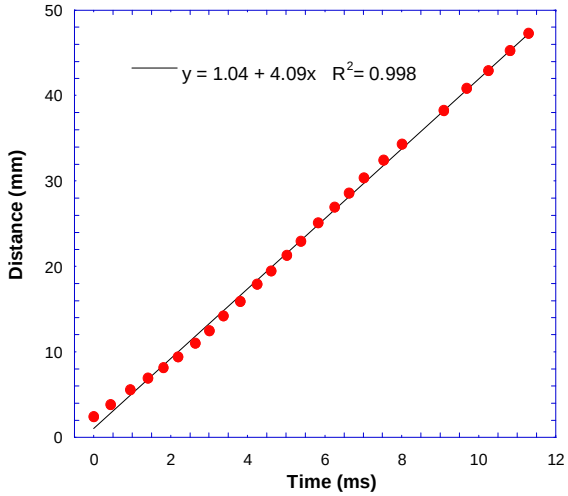

Figure 6: *x-t* plot for the flame propagation shown in Figure 4. The slope indicates a flame propagation speed of 4.09 m/s.

The flame propagation speeds on various substrates were studied to examine the effect of structure and substrate properties on the properties of PS-oxidizer composites. The samples without a micro-crack pattern always resulted in low propagation speeds, between 1 to 12 m/s. The low doped n-type substrates with a random micro-crack pattern always yielded high propagation speeds, ~300 m/s. The flame propagation speeds and the spectroscopically measured temperatures observed on the various etched samples are summarized in Table 2. The flame

temperature could not be estimated for the 10–20 Ω-cm p-type substrates due to the low intensity of the propagating wave.

The fill efficiency for the salt deposition within the pores was carried out using $CoCl_2$, as described in the previous section. The gravimetrically calculated fill efficiencies are shown in Table-3. The amount of salt deposited consistently exceeded the predicted maximum deposition.

Table 2: The flame propagation speeds observed on the four different kinds of substrates used to prepare PS. The porous layers were impregnated with $NaClO_4$ using saturated solutions of the oxidizer in methanol. The SSA for the samples was measured using a multi-point BET measurement, and the temperatures were estimated spectroscopically.

Dopant atom	Resistivity (Ω-cm)	Porosity (%)	SSA (m^2/g)	Flame speed (m/s)	Temperature (K)
Boron	0.001 - 0.005	60	312	3 - 3.3	1770 - 1950
Arsenic	0.001 - 0.005	62	423	5.4 - 11.0	2313
Phosphorus	2 - 5	-	145	314 - 372	3208
Boron	10 - 20	-	-	4.9	-

Table 3: Gravimetric fill efficiency measurement for heavily doped p-type PS using cobalt chloride.

# samples	Porosity (%)	Void space (cm^3)	Fill Efficiency	$CoCl_2$ deposition (g/ml)
1	59.36	0.019	2.04	0.167
2	63.94	0.016	1.39	0.385
3	63.94	0.024	1.50	0.167
4	71.38	0.018	2.45	0.385
5	71.38	0.032	1.89	0.333
6	59.36	0.021	2.24	0.167

CONCLUSIONS

Etch recipes were developed to prepare thick and mechanically stable porous layers, which are required to study the energetic properties of PS-oxidizer composites. The porous layers were etched on both n- and p- doped substrates with widely varying dopant atom concentrations. The etched PS samples were characterized by means of gravimetric porosity and thickness measurements, SEM images, and multi-point BET surface area measurements. The heavily doped substrates were always found to yield stable porous layers without any micro-crack patterns, while the low doped n-type substrates etched under illumination always exhibited a micro-crack pattern. Energetic composites were prepared by soaking the PS samples in oxidizer-methanol solutions, and the flame propagation was characterized by high speed videography and spectroscopic temperature

measurements. Porous layers without any micro-crack pattern were found to result in low speed flame propagations. The fast flame propagations observed on the low doped n-type substrates are attributed to the micro-crack pattern. The deposition of the oxidizer within the nanoscale pores was studied by using an alternative non-reactive salt which permits cleaning of the surfaces for accurate measurements. The gravimetric deposition measurements indicate that the amount of salt deposited in the pores was consistently higher than the maximum predicted deposition. This might be due to an interaction between the high surface area porous material and the salt, causing excessive deposition. One of the main concerns with preparation of PS-oxidizer energetic composites is the oxidizer deposition, and this study shows that typically more oxidizer than expected is deposited in the pores.

ACKNOWLEDGMENTS

First and foremost, I would like thank the EE Department at Pennsylvania State University for giving me the opportunity to participate in their EE REU program and the National Science Foundation (Grant No. EEC-106298) for funding this research. I also wish to thank my mentor Prof. Srinivas Tadigadapa and grad student mentor Venkata Sharat Parimi for their vast reserve of patience and knowledge. I appreciate you allowing me to work by your side as I would not have been able to complete this research without your guidance. Finally, a special thanks to my family for their unconditional support.

REFERENCES

[1] Niarchos D. Magnetic MEMS: key issues and some applications. Sensors and Actuators A: Physical 2003; 106(1-3):255.

[2] Rossi C, Esteve D. Micropyrotechnics, a new technology for making energetic microsystems: review and prospective. Sensors and Actuators A: Physical 2005; 120(2):297.

[3] Uhlir A. Electrolytic Shaping Of Germanium and Silicon. Bell System Technical Journal 1956; 35(2):333-347.

[4] McCord P, Yau S-L, Bard AJ. Chemiluminescence of Anodized and Etched Silicon: Evidence for a Luminescent Siloxene-Like Layer on Porous Silicon. Science 1992; 257(5066):68-69.

[5] Kovalev D, Timoshenko VY, Kunzner N, Gross E, Koch F. Strong Explosive Interaction of Hydrogenated Porous Silicon with Oxygen at Cryogenic Temperatures. Physical Review Letters 2001; 87(6):068301.

[6] Mikulec FV, Kirtland JD, Sailor MJ. Explosive Nanocrystalline Porous Silicon and Its Use in Atomic Emission Spectroscopy. Advanced Materials 2002;14(1):38.

[7] Clément D, Diener J, Gross E, Künzner N, Timoshenko VY, Kovalev D. Highly explosive nanosilicon-based composite materials. physica status solidi (a) 2005;202(8):1357.

[8] Canham L. Properties of Porous Silicon. In: Institution of Engineering and Technology; 1997.

[9] Ng D. and Fralick G. Use of multiwavelength pyrometer in several elevated temperature aerospace applications. NASA Glenn Research Center, Cleveland, Ohio. November 2000.

GROWTH OF PYRAMIDAL NANOWIRES ON ALUMINUM DIFFUSED SILICON WAFERS FOR PHOTOVOLTAIC DEVICES

Katelynn Jourdan,* Joan Redwing,[#] Sarah Eichfeld,[+] and Haoting Shen[++]

Department of Electrical Engineering
The Pennsylvania State University, University Park, PA 16802

Undergraduate Student of
Department of Electrical & Computer Engineering
University of Iowa
Iowa City, Iowa 52242

ABSTRACT

Photovoltaic devices are increasingly being utilized for clean energy. One way to increase the efficiency of these devices is to optimize the surface area using low cost methods. The element aluminum acts as a p-type dopant in silicon (Si) and catalyzes the growth of silicon nanowires (SiNWs). This project utilizes the diffusion of aluminum (Al) into n-type silicon wafers to create a p–n junction and catalyze the growth of nano-pyramids. The wafers undergo RCA (removal of organic contaminants and ionic contaminants) and BOE (Buffered Oxide Etch) cleanings to prepare them for deposition. Aluminum is deposited onto the wafer using a thermal evaporator. The aluminum is then diffused into the silicon during the process of annealing. The excess aluminum left on the surface after diffusion will be used to measure electrical properties. A contact will then be created on the n side of the junction using silver. This will allow for electrical characterization of the device. The sample could then be placed into a low pressure chemical vapor deposition (LPCVD) system to grow nano-pyramids. The nano-pyramids would be grown by flowing silane (SiH4) over the aluminum at a temperature between 500–800 °C. Our initial experiments will examine different thicknesses of aluminum deposition, annealing temperatures, and annealing time to determine the best conditions to form both a p-n junction and grow nano-pyramids. The thickness of aluminum examined will range from 5–20 nm, the annealing

---

* Undergraduate Student
[#] Faculty Mentor
[+] Graduate Mentor
[++] Secondary Mentor

temperatures will be between 300–700 °C, and the annealing time will range from 20–60 min. This project aims to determine an effective process to create the most efficient photovoltaic device that can reduce reflection, harvest the greatest amount of sunlight, and optimize the device's surface area.

INTRODUCTION

Cost Effective and Efficient Photovoltaic Devices

Solar energy is a form of clean energy that is desperately needed with the high cost of fossil fuels. Photovoltaic devices are an energy source with a large potential but too expensive to be competitive with grid electricity. Most of the production cost is due to the silicon wafer itself [1]. Consequently, a photovoltaic device needs to be created that is not only cost effective, but still as efficient as today's current devices.

Nanowire Growth

Most of today's solar cells are planar. Planar solar cells are less efficient due to absorption losses. Planar solar cells reflect some of the incident light instead of absorbing and converting it to useable energy. The planar surface is also not capable of trapping absolutely all the penetrating photons [2]. Therefore, research on the use of silicon nanowires has increased rapidly due to their possible use in future electronic and sensor nanodevices, including solar cells [3]. Researchers have been trying to optimize the surface area of photovoltaic devices by growing nanowires on the cell's surface. The nanowires help to absorb and trap more of the incident light, making the device more efficient. A typical nanowire solar cell fabrication process can be seen below in Figure 1.

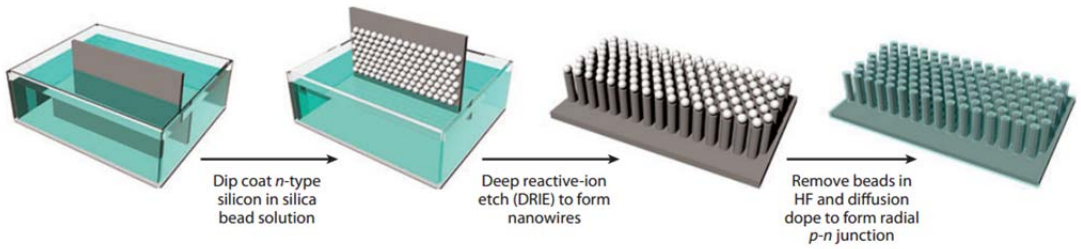

Figure 1: Nanowire Solar Cell Fabrication [2]

In today's research, the nanowire growth has been carried out in vertical, ordered arrays. Silicon nanowire arrays are grown using chemical vapor deposition (CVD) and the vapor-liquid-solid (VLS) growth mechanism [2]. This paper discusses the experiments done to create a p–n junction from which the growth of nano-pyramids can be performed. Once the process for creating an ideal p–n junction is found, the nano-pyramids can be grown using low pressure chemical vapor deposition (LPCVD). By creating these pyramids on the surface of the device, the light trapping and absorption increase. It also creates an

extremely anti-reflecting layer on the surface of the device. This makes the photovoltaic device more efficient and cost effective.

Diffusion of Aluminum into Silicon to Form a p–n Junction

In order to create a photovoltaic device, a basic p–n junction is needed. A p–n junction is created when p-type and n-type materials are brought in contact. Once the two types come in contact, the n-type material becomes positively charged while the p-type material becomes negatively charged, creating a built-in electric field. The electric field at the junction allows current to flow in only one direction under certain bias, from the p-type to the n-type material. Energy from sunlight enters the semiconductor materials as photons. When the photons hit the semiconductor materials they can energize valence electrons, sending them into the conduction band. Once the valence electrons are energized they leave behind holes. The photo-generated electrons and holes then diffuse in materials and can be swept to the n-type material and p-type material by the built-in electric field, respectively [4]. In Figure 2 below, it can be seen how the p–n junction is formed.

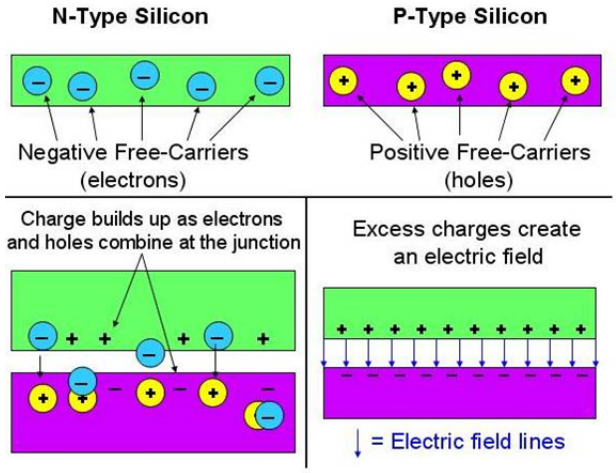

Figure 2: Formation of a p–n junction [4]

In our study, aluminum was diffused into silicon via thermal evaporation to form the p–n junction. Aluminum was chosen due to its low cost and high conductivity. Aluminum is also the fastest diffusing acceptor dopant in silicon and has been discovered to catalyze the growth of nanowires [5]. Gold is the most commonly used catalyst in silicon nanowire growth, but creates deep levels in the silicon band gap. Gold traps the electron-hole pairs in silicon and creates contamination, detrimental to the creation of metal oxide semiconductors. On the other hand, the use of aluminum as a growth catalyst is beneficial because since aluminum is a p-type dopant for silicon, it helps to avoid the formation of deep levels in the band gap [3]. Without deep levels in the band gap, this also helps to minimize the series resistance. And a series resistance of even a few ohms can greatly degrade the device performance [6].

EXPERIMENT DESCRIPTION

RCA Cleanings

To create a p–n junction, we used an n-type silicon wafer and doped it with aluminum. In order to create an uncontaminated p–n junction, we first needed to adequately clean the silicon wafer. Therefore, the wafers underwent an RCA cleaning, the removal of organic contaminants and then ionic contaminants. To start the RCA clean the wafers were immersed in acetone at 70 °C on a hotplate for 10 minutes. They were then immersed in isopropyl alcohol also at 70 °C on a hotplate for another 10 minutes. Once the 10 minutes were up, the wafers were rinsed with distilled water for 5 minutes. Next, the wafers were placed in RCA-01, consisting of 600 ml of distilled water, 150 ml of hydrogen peroxide, and 100 ml of ammonium hydroxide, at 70 °C for 10 minutes. Subsequently, the wafers were rinsed in distilled water for 5 minutes then placed in RCA-02 at 70 °C for 10 minutes. The RCA-02 was made with 700 ml of distilled water, 150 ml of hydrogen peroxide, and 100 ml of hydrochloric acid. The RCA-02 is used to remove the ionic contaminants. Finally, the wafers were rinsed with distilled water again for 5 minutes and dried.

Lithography

In order to control the device area, lithography was performed on the wafers. The first step in lithography was to apply photoresist upon the wafer. To do so, the samples were placed on a hot plate and pre-baked at 100 °C for 1–2 minutes to make sure all residing chemicals on the surface were evaporated. The sample was then put on a photoresist spinner and suction was applied via a vacuum. Suction was applied so that the sample did not move during spinning. When adequate suction was achieved, we used a pipette to place droplets of photoresist on the wafer until the surface was nearly covered. Next, the spinner speed was set to 4000 rpm and started. That allowed the photoresist droplets to spread out and uniformly cover the wafer surface. After 45 seconds of spinning, the sample was placed on a hotplate at 115 °C and baked for 1 minute. After that, until lithography was complete the sample could not be exposed to everyday light. Therefore, the sample was placed in a container and covered with aluminum foil to be transported to the next station.

After the photoresist was applied, a patterned mask was placed over the sample. The mask only allowed certain areas of the sample to be exposed to ultraviolet light when placed in the lithography machine. The mask had a pattern that created 1 mm devices. After the wafer was exposed to ultraviolet light, and the pattern was created on the surface, the sample was placed in a solution consisting of 1 part 351 solution and 4 parts distilled water. This solution developed the photoresist and removed the areas of the photoresist that were exposed to the ultra violet light. After development, only the 1 mm square areas of silicon were left exposed.

BOE Cleanings

Once lithography was finished, the second cleaning process the wafers went through was a BOE cleaning (buffered oxide etch). The BOE cleaning was necessary to remove the thin oxide layer left during the ammonium-peroxide cleanings. BOE consists of hydrofluoric acid and ammonium fluoride. To perform the process, the wafer was immersed in the BOE solution for 3 minutes. The surface of the wafer was then hydrophobic. After soaking, the wafer was removed from the solution, dried, and quickly loaded into the thermal evaporator for deposition so as not to contaminate the surface again.

Deposition and Lift-Off

The samples were then loaded into a thermal evaporator and 20 nm of aluminum were deposited onto the surface of the wafer. Inside the thermal evaporator, aluminum was deposited onto the 1 mm device areas and on top of the undeveloped photoresist areas. To remove the unwanted photoresist and aluminum layered areas, the wafers were submerged in 1165 solution for up to an hour depending on when the lift-off process was complete. The lithography and lift-off process is depicted in Figure 3 below.

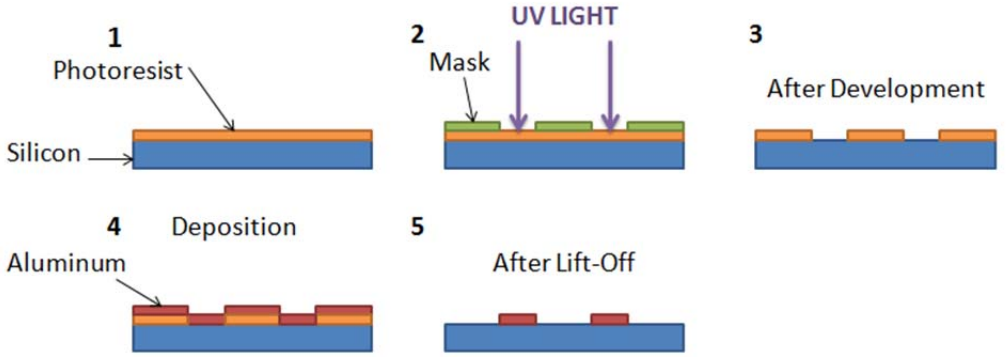

Figure 3: Lithography and Lift-Off Process

Annealing and Addition of Back Contact

Once the lift-off process was complete, we annealed the samples. The wafers were cleaved so that 4–6 of the 1-mm devices were on each piece. The samples were then placed on a quartz boat and loaded in the center of the annealing furnace. When the sample was loaded, the furnace was purged with nitrogen for 15 minutes prior to annealing. Previous studies done by Krause et al showed that the longer the annealing process, the higher the thermal cost and risk for contamination within the junction [5]. Therefore, we chose to anneal the samples at atmospheric pressure for short time periods between 20 and 60 minutes at temperatures between 300 and 700 °C. After the anneal it was apparent that the surface of the devices were not completely uniform, which could lead to a poor front contact. Therefore, we hand-painted photo-resist around our 1-mm devices and deposited more aluminum via thermal evaporation. That way there would be

a continuous and effective front contact on our devices. Once the aluminum was deposited, we removed the unwanted photoresist with acetone.

When the photoresist was completely removed the next step in order to make the wafers devices, was to add a back contact. We created the back contact out of silver to reduce the amount of series resistance as much as possible. To do that, we coated the front side of the wafers with photoresist. This was done to protect the sensitive front surface from, being scratched and silver molecules during deposition. The wafers were then placed in BOE for 5 minutes, rinsed with distilled water, dried, and loaded into the thermal evaporator to be deposited with silver. After the back contact was created, the wafers were devices that could be tested.

EXPERIMENT RESULTS

Current vs. Voltage and Ideality vs. Voltage Plots

Once the devices were created we probed them and created current-voltage and ideality-voltage plots to see which devices under which parameters behaved the most like an ideal diode. The plots of the best devices from each category we tried on the first trial are shown in Figure 4.

From Figure 4 it can be seen that the best devices were annealed at 300 and 500°C. The samples annealed at 300 °C had higher leakage current than the samples annealed at 500 °C, but had a high turn-on voltage. The samples annealed at 700 °C were almost linear or had too much leakage current. In order to decide what further parameters we would test, the ideality factor was also calculated for each sample. The ideality factor is a measure of the unknown effects which make the device non ideal [6]. The ideality factor calculation can be seen starting with Equation (1).

$$I_D = I_0 \exp(\frac{qV}{nkT} - 1) \tag{1}$$

$$\ln I_D = \ln[I_0 \exp(\frac{qV}{nkT} - 1)] \tag{2}$$

$$\ln I_D = \ln[I_0 \exp(\frac{qV}{nkT})] \tag{3}$$

$$\ln I_D = \ln I_0 + \ln \exp(\frac{qV}{nkT}) \tag{4}$$

$$\ln I_D = (\frac{q}{nkT} \times V) + \ln I_0 \tag{5}$$

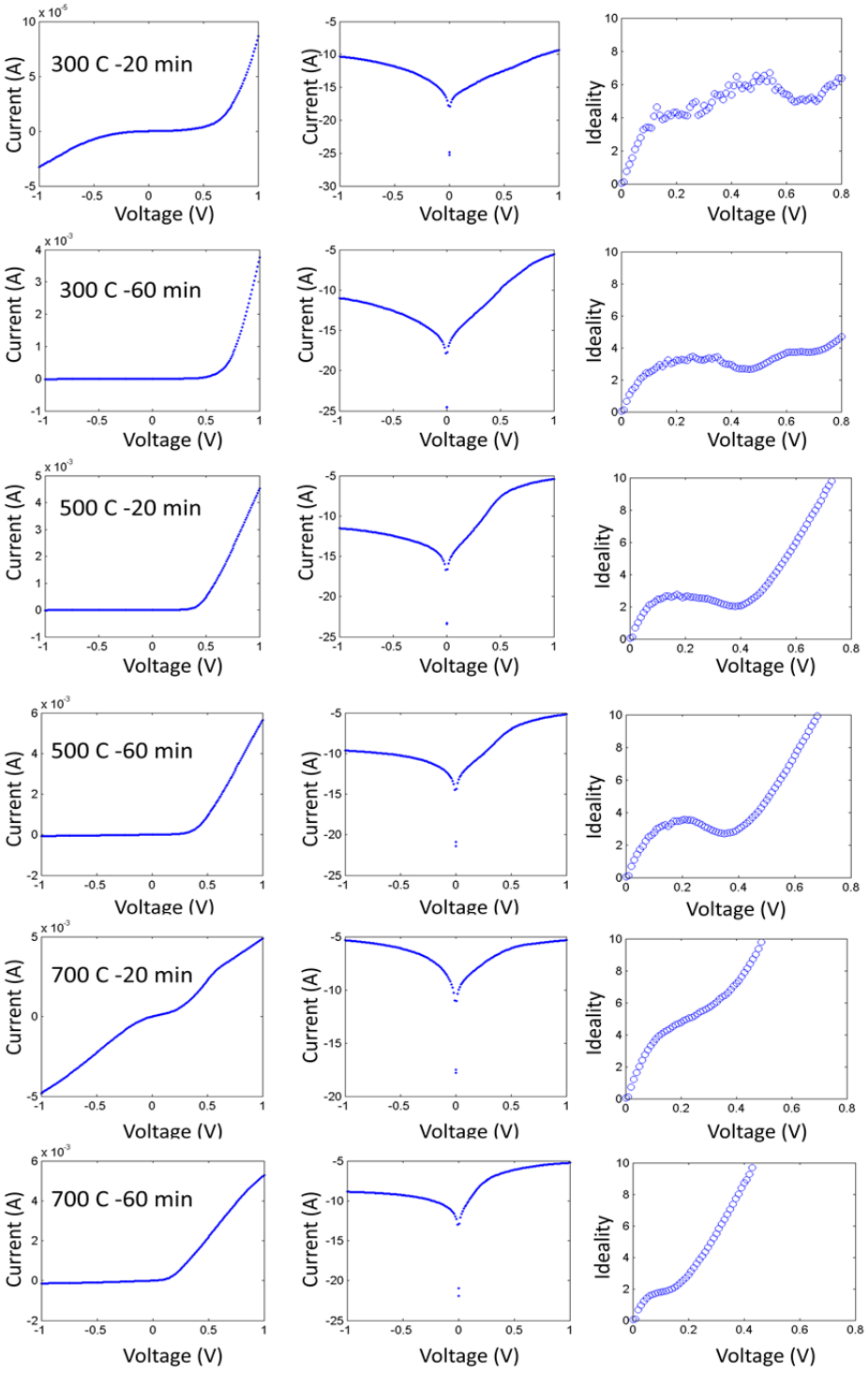

Figure 4: Current vs. Voltage and Ideality vs. Voltage Plots of best samples

In these calculations I_0 represents the reverse saturation current, I_D is the diode current, q is the charge of an electron, n is the ideality factor, k is Boltzmann's

constant, and T is temperature in Kelvin. From Equation (5), it is shown that the ideality factor can be calculated from the slope of the line on a plot of $\ln I_D$ versus voltage. For a good diode device, the ideality factor should be around 1 or 2. Therefore, based on our calculations we decided to create more devices and annealed them only at 300 and 500 °C, but at more time intervals.

DISCUSSION

The exact parameters of the diffusion of aluminum into silicon are still not completely understood. One reason we believe the p–n junctions may not be ideal is due to aluminum spiking during diffusion. The element silicon melts at 1412 °C and the element aluminum melts at 660 °C. Although, when the two elements are mixed together they display eutectic characteristics meaning, the mixture lowers the melting point to below that of either element. The eutectic temperature for aluminum-silicon is 577 °C. And based on the aluminum-silicon phase diagram, at annealing temperatures of 450–500 °C aluminum will absorb 0.5–1% silicon. Even though those annealing temperatures are below the eutectic temperatures, some silicon still diffuses into aluminum [7]. As the silicon dissolves, aluminum spikes are formed. And if the device has shallow p–n junctions, the spikes can cause shorts [7]. The formation of aluminum spikes can be shown below in Figure 5.

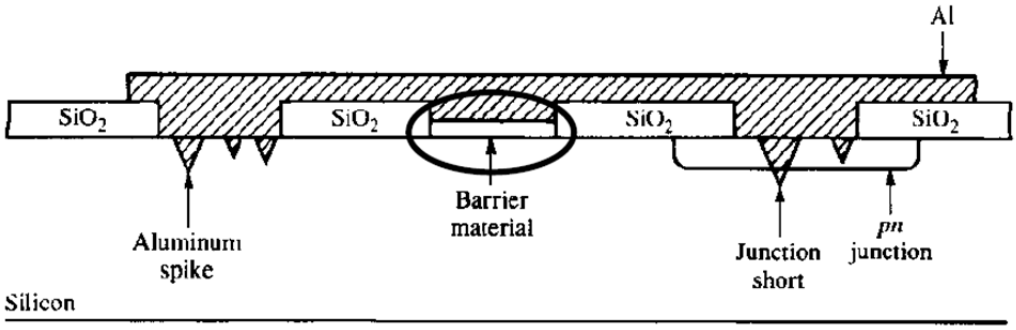

Figure 5: Formation of Aluminum Spike [7]

One way to prevent aluminum spiking is to saturate the aluminum with silicon. This could be done by depositing a polysilicon layer before depositing the aluminum. Consequently, the polysilicon would provide enough silicon to saturate the aluminum during deposition and avoid the formation of spikes. Another solution could be to add silicon to aluminum during deposition by coevaporation. Or lastly, a barrier metal could be deposited between the aluminum and silicon as shown in Figure 5. This option would be unfavorable for photovoltaic devices, because this would not allow the aluminum to diffuse into the silicon at all, necessary for p–n junctions [7].

Another reason the p–n junctions has defects could be due to the p–n junction creation process. Instead of the formation process stated earlier, aluminum could be deposited onto the silicon wafer and annealed before lithography. After annealing, the wafer could then undergo lithography leaving the photoresist

covering the square devices. Once the lithography is complete, reactive ion etching could be used to etch the uncovered areas until the diffused layer is gone. Therefore, only the aluminum diffused squares would be left. Creating the junction this way could reduce the amount of contamination.

CONCLUSION

Based on results to date, it appears that the annealing temperature of 700 °C is too high to create an ideal p–n junction. It leads to too much current leakage and does not show rectifying behavior on the *I-V* curve. The annealing temperatures of 300 and 500 °C create acceptable p–n junctions. The proper time duration of annealing at those temperatures has yet to be determined. More experiments need to be done to conclude which time is best. Upon further optimization of the annealing, future work includes growth of nano-pyramids on the p–n junctions.

ACKNOWLEDGMENTS

This material is based upon work supported by the National Science Foundation under Grant No. EEC-1062984. Furthermore, I would like to thank Sarah Eichfeld for mentoring me, guiding me, and answering all my questions throughout the project. I would also like to thank Haoting Shen for all his support, showing me how to perform the experiments, how to use the equipment every day, and answering any questions I had. I would like to thank Joan Redwing for providing me with this research opportunity as well.

REFERENCES

[1] Wolden, Colin A., Juanita Kurtin, Jason B. Baxter, Ingrid Repins, Sean E. Shaheen, John T. Torvik, Angus A. Rockett, Vasilis M. Fthenakis, and Eray S. Aydil. "Photovoltaic Manufacturing: Present Status, Future, Prospects, and Research Needs." *Journal of Vacuum Science and Technology A* 29.3 (2011). American Vacuum Society. Web. Cubesat Community Website. 2 October 2008. California Polytechnic State University. 5 June 2009. <http://cubesat.atl.calpoly.edu/media/CDS_rev11.pdf>.

[2] Garnett, Erik C., Mark L. Brongersma, Yi Cui, and Michael D. McGehee. "Nanowire Solar Cells." *Annual Review of Materials Research* 41.1 (2010): 269-95. Print.

[3] Wang, Yewu (2006). "Epitaxial growth of silicon nanowires using an aluminium catalyst". *Nature nanotechnology(1748-3387)*, 1 (3), p. 186.

[4] Gleue, Alan D. "The Basics of a Photovoltaic Solar Cell." N.p., June 2008. Web. 3 July 2012. <http://teachers.usd497.org/agleue/Gratzel_solar_cell%20assets/Basics%20of%20a%20Photo voltaic%20%20Solar%20Cell.htm>.

[5] J. Appl. Phys. 91, 5645 (2002)

[6] Schroder, Dieter K. *Semiconductor Material and Device Characterization*. 3rd ed. New York [etc.: John Wiley & Sons, 2006. Print.

[7] Jeong, Heado. "Interconnections and Contacts." Online PowerPoint. 10 July 2012. <http://www.cmplab.re.kr/board/pds/board_download.php?file=pds0155_2.pdf&dn=1>.

CHARACTERIZATION OF FLUORESCENT MICROSPHERES FOR USE AS A LASER GAIN MEDIUM AND RESONATOR

Porter Beus,* Perry Edwards,[+] Corey Janisch,[+] and Zhiwen Liu[#]

Department of Electrical Engineering
The Pennsylvania State University, University Park, PA 16802

*Undergraduate Student of
Department of Electrical & Computer Engineering
Arizona State University
Tempe, Arizona 85287-0112

ABSTRACT

This work explores the use of fluorescent microspheres as both the resonator and gain medium for a fiber-coupled microsphere laser. The experimental setup involved depositing a 10-micron diameter fluorescent microsphere to the waist of a tapered optical fiber with a diameter of approximately one micron. The microspheres were held in place on the taper by van der Waals forces and interacted with the evanescent mode of a pump laser propagating through the fiber. The coupled pump laser field excited fluorescence which resonated within the microsphere. Characterization of the fluorescence and attempts at determining the lasing threshold and laser spectrum were performed by coupling the output of the fiber taper to an optical spectrometer.

INTRODUCTION

The laser is one of the most important optical tools to come out of the 20th century. Since its inception, over five decades ago, lasers have been utilized in a myriad of applications including data storage (e.g., CD-ROM), in surgical procedures (e.g., laser eye surgery), and precision machining (laser cutting/welding, etc.). Simply speaking, a laser consists of three basic components: an optical pump source, a gain medium, and a laser cavity. However, since its creation, the laser has transformed from a simple cavity to a variety of realizations (e.g., diode lasers, fiber lasers) utilizing many different types of gain mediums (gas, liquid, crystal, doped substrates), and implementations employing either continuous-wave (CW) or pulsed operation

[#] Faculty Mentor
[+] Graduate Mentor

including Q-switched (e.g., nanosecond pulse-width) and ultrafast mode-locked (e.g., picosecond to femtosecond pulse-width) lasers [1]. In addition, many novel methods have been introduced for forming optical cavities. Much work has been done in the area of micro-resonators as optical cavities [2]; and a select few have explored the use of micro-resonators as platforms for lasing. One method in this area which has been tested involves taking advantage of the high quality factor that exists in micro-resonators. Specially fabricated Erbium:ytterbium doped microspheres were coupled to a tapered fiber carrying a pump laser and have been shown to lase under certain conditions [3].

In this work, however, the use of mass produced fluorescent dyed microspheres is explored as both the gain-medium and resonator for creating a micro-cavity laser. Traditionally, these fluorescent dyed microspheres are used for labeling specific cellular components or tissues in biological imaging. Here, we take advantage of the highly spherical nature of the microsphere particles to act as a micro-cavity (similar to previous demonstrations [4]), and the fluorescent dye as gain medium. The spheres were deposited on a tapered single-mode fiber. A pump laser was sent through the fiber to interact with the sphere and generate fluorescence. The fluorescence can then be guided within the microsphere by the supported cavity modes. The potential for lasing action is explored by varying the incident power and taper-sphere coupling conditions.

EXPERIMENT DESCRIPTION

Here we briefly discuss the concept of a microsphere laser and then discuss in detail the experimental setup which includes tapering an optical fiber and placement of a microsphere on the taper.

Microsphere resonators

Microspheres are a type of circular-resonators where the cavity is continuously folded on itself; they confine the optical pathways of light propagating through the resonator to promote cavity build-up or light "storing" capability. The losses that exist within the cavity determine the effective build-up. Much work has been done on optimizing this build-up factor by creating very high quality (Q) microspheres [e.g., ref. 3]. The Q factor of a microsphere cavity can be described as

$$Q = 2\pi \frac{E_s}{E_d}, \tag{1}$$

where E_s represents the energy stored within the microsphere and E_d represents the energy dissipated per round trip cycle within the cavity.

The physical dimensions of a resonator define its free spectral range, namely the frequency difference between the supported cavity modes. For the case of a spherical resonator, the free spectral range can be described in terms of wavelength ($\Delta\lambda$)

$$\Delta\lambda = \frac{\lambda^2}{2\pi nr}, \tag{2}$$

where λ is the averaged wavelength of the two peaks, n is the index of refraction of the medium, and r is the radius of the sphere.

Microsphere coupling

Several methods exist for coupling light to a micro-cavity. One of the most well demonstrated techniques involves tapering an optical fiber to expose the evanescent tail of the propagating mode of a fiber-coupled pump laser. .The derivation of the existence of these waves can be solved through Maxwell's equations in the case of a totally reflected wave. It is sufficient to mention that these waves decay exponentially with the distance from the boundary. It has been shown that the small diameter waists are required for efficient coupling to microresonators [5]. In addition, the tapered fiber maintains its waveguide properties, despite the small size (where core and cladding merge together) by using the glass-air boundary to guide light. The existence of the exposed evanescent tail of a tapered fiber makes it possible for effective coupling into and out of a microsphere. When a taper is brought sufficiently close to the microsphere, the exposed evanescent tail can couple into the microsphere cavity. This method has been shown to be a successful way to transfer light from a fiber to a microsphere [2].

It has been shown that efficient coupling of the pump laser to the sphere cavity can create the conditions for lasing [3]; however, in this work we characterize the use of mass produced microspheres for possible use in a simpler microsphere laser. The pump laser interacts with the sphere at the taper-sphere boundary to generate fluorescence which can be filtered by the cavity modes of the sphere. The microspheres were selected to optimally generate fluorescence from a 532-nm pump laser and were dyed internally with an organic fluorescence compound whose absorption peak is 525 nm and emission peak is at 565 nm (Bang Laboratories, Envy Green microspheres).

Optical fiber tapering

The usefulness of an optical fiber is primarily reliant on two things: the diameter of the waist and the transmission efficiency of the fiber. As described previously, a small diameter is needed to ensure sufficient exposure of the evanescent tail of the propagating mode. In addition to achieving a small tapered waist, the efficiency of a fiber is characterized by the adiabatic nature of the taper which defines the transition from a large diameter to a smaller diameter. Tapers which are more adiabatic have less loss and a higher transmission of light, due to smooth transition between modal interference within the fiber. Furthermore, losses can arise from scattering centers which occur due to fiber impurities or more commonly from cladding residue and dust left on a fiber after preparing a fiber for tapering.

The tapered fibers for this experiment were made using a visible wavelength single mode fiber (SM600) stripped of its outer coating. Then, using alcohol and optical wipes, the fiber was cleaned to the point of having very little residue left

on the fiber. This was verified by viewing the fiber through a microscope as shown in Fig. 1.A. The portion of the fiber to be tapered was placed between two fiber clamps, as seen in Fig. 1.A. Once clamped into place a hydrogen gas flame was introduced as the heating element for tapering. The optimal gas flame pressure and position were experimentally found through previous fiber pulls. The softened fiber was stretched by computer controlled actuators which pulled the fiber at 0.05 mm per second for approximately 28 mm. During the pull the end of the fiber was attached to a photodiode which was connected to an oscilloscope to monitor the fiber transmission during the tapering process (e.g., transmission plot in Fig. 1.C). The fiber was tapered from a relatively large 125 μm diameter (Fig. 1.B) down to roughly 1 μm in diameter (Fig. 1.D).

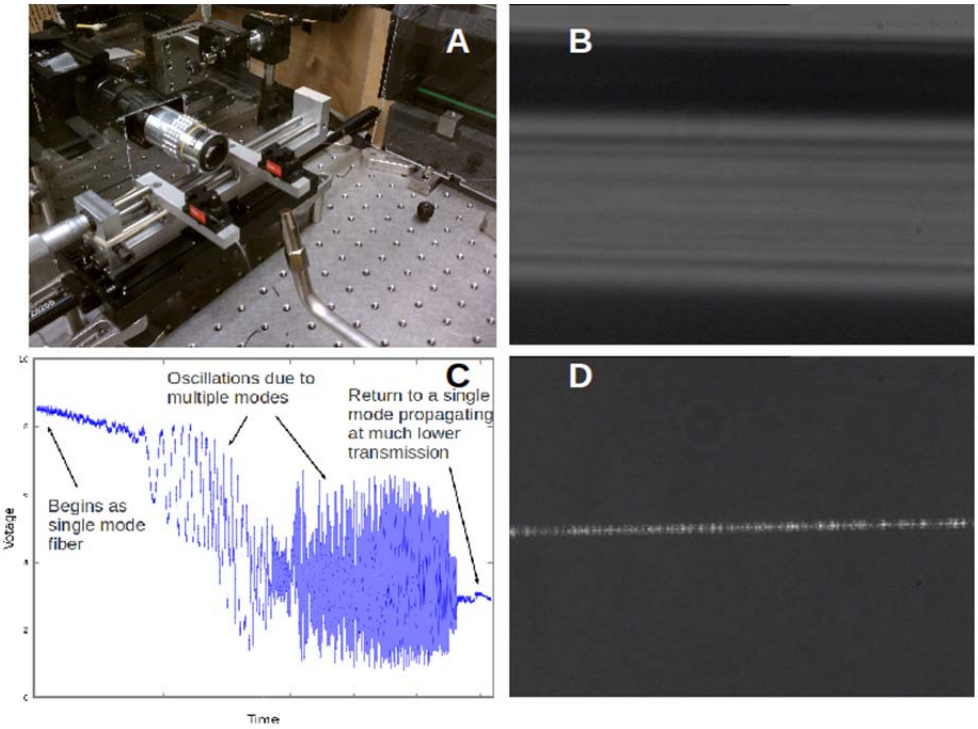

Figure 1: The pulling process. (A) Fiber pulling setup, including the microscope, fiber clamps, computer controlled actuators, and the hydrogen flame. (B) Cleaned fiber before pulling. (C) Transmission plot of a complete fiber pull. Initially single mode with no oscillations, then interfering modes cause transmission oscillation as the pull continues, and finally the fiber returns to single mode propagation without oscillations. This fiber taper has a transmission of approximately 33%, but only tapers with greater than 60% transmission were used in experiments. (D) The finished fiber, not quite resolvable with the microscope. The bright spots are defects in the now very thin fiber taper.

During the tapering process the core and cladding merge together to become a single index waveguide. However, when the fiber is still relatively thick and the

core-cladding merging is still occurring, the fiber can support multiple propagation modes. The different modes begin to interfere with each other and can be seen on the oscilloscope in the form of oscillations in the transmission readings. The period of these oscillations become shorter and the amplitude tends to shrink as the interference from the various modes is reduced. Pulling is continued until the transmission finishes oscillating, signaling a return to a single mode propagating through the fiber. Figure 1.C shows a time compressed image of the oscillations and return to single mode. By comparing the final power reading with the initial power reading, the transmission efficiency of the newly formed taper is determined.

Placing sphere

To place the microsphere on the taper, another probe fiber was tapered with a much sharper angle using a high voltage arc splicing machine. This sharp taper was then broken in half, and one half was used as a probe for delivering the spheres to the waist of high transmission fiber taper (see Fig. 2.A & 2.B). The microspheres, which came in a solution, were left in drops to dry on a glass slide. These spheres were rated to have an approximate diameter of 9.94 μm. Once dry, the probe fiber was dragged through the piles of microspheres in an attempt to attach the spheres to the fiber's tip. Using a microscope and manually operated actuators the microspheres were placed on and adhered to the waist (thinnest region) of the taper via van der Waals forces (setup pictured in Fig. 2.C).

Light from the 532-nm laser coupled into the fiber and passed through a polarization controller. Using the polarization controller on the fiber, pre-taper, the coupling of laser light into the sphere can be maximized. Following the controller the light entered the taper and coupled into the sphere. After the fiber taper, the fiber was coupled through a collimator, a focusing lens and a 532-nm long-pass filter (which filtered out most of the 532-nm laser light) before coupling into the spectrometer. Once the microsphere was in place, a 532-nm laser was sent through the fiber and was evanescently coupled into the microsphere (Fig. 2.D). Figure 3 describes the experimental setup in more detail.

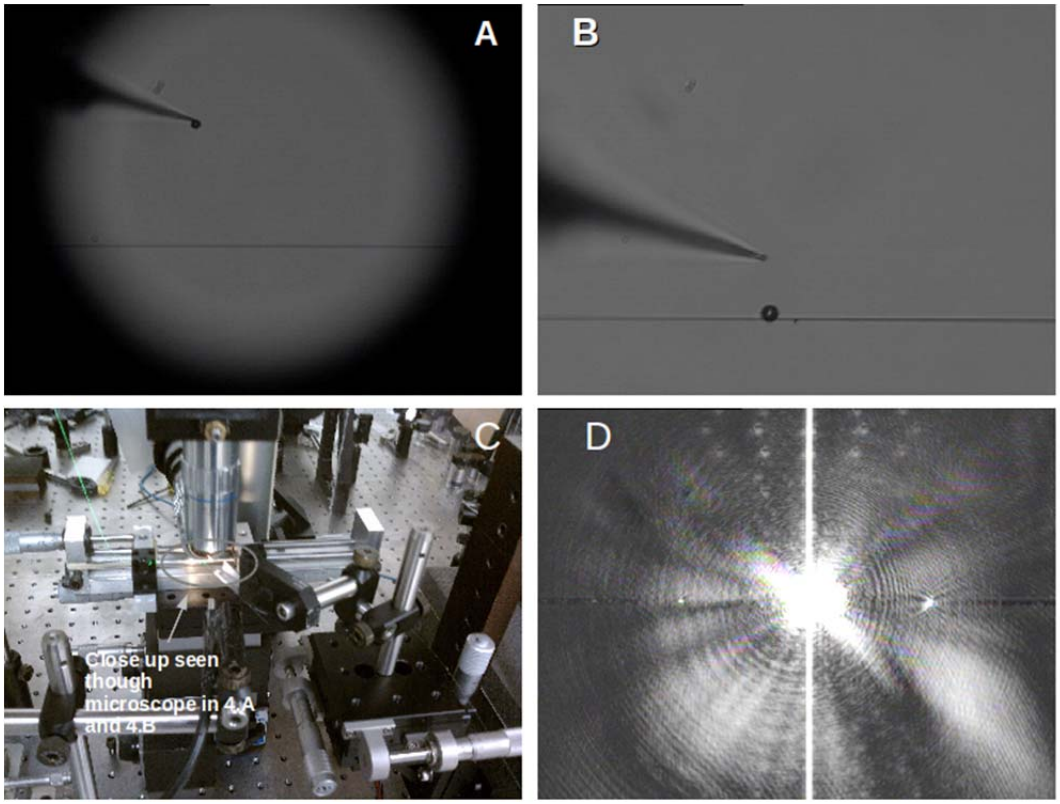

Figure 2: (A) Probe fiber with a microsphere on the tip. (B) Microsphere after placement on the waist of fiber due to van der Waals forces. (C) Setup of actuators used to place the spheres on the fiber taper. (D) Attached microsphere coupled with laser. Large amounts of scattering saturate camera pixels.

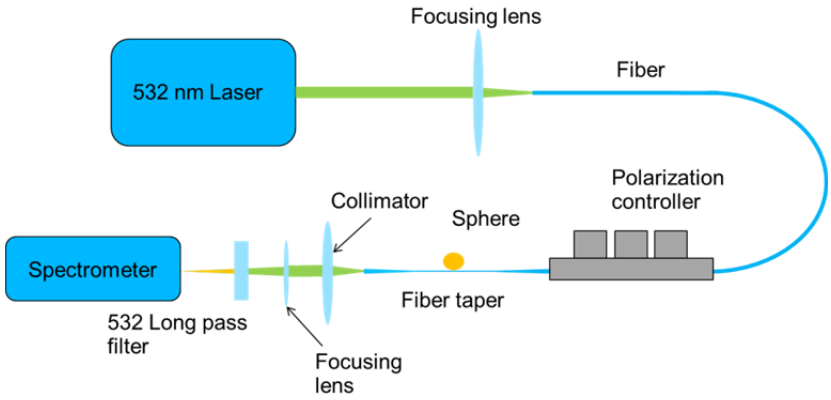

Figure 3: The laser is coupled into a single mode fiber with a polarization controller and a tapered portion. The roughly 1-µm-diameter fiber taper is coupled evanescently with a microsphere. The resulting light is sent though a collimator a focusing lens and a 532-nm long pass filter to filter out excess 532-nm laser light before entering the spectrometer (PI/Acton 2500i, LN-cooled CCD) for characterization.

EXPERIMENT RESULTS

To investigate the fluorescence activity from a microsphere attached to a fiber taper, the output of the taper was monitored with a spectrometer, as shown in Fig. 3. A typical spectrum acquired by the spectrometer is shown in Fig. 4, using a 30-ms integration period and pump power into the system of approx. 4 mW. This spectrum demonstrates excitation of fluorescence; however, the fluorescence is filtered by the microsphere cavity, which is evident by the multiple peaks demonstrated in the spectra. The separation indicates the FSR of the cavity, and can be confirmed by using the indicated FSP in Fig. 4 to calculate the diameter of sphere. This is done by first solving Eqn. 1 for the sphere diameter. Then using the values of $\Delta\lambda$ = 8.3 nm (mode separation in Fig. 3), λ = 608.3 nm, and n = 1.5917 for polystyrene (PS), the diameter is found to be 9.0 μm, which is close to the manufacturer's labeled size of 9.94 μm.

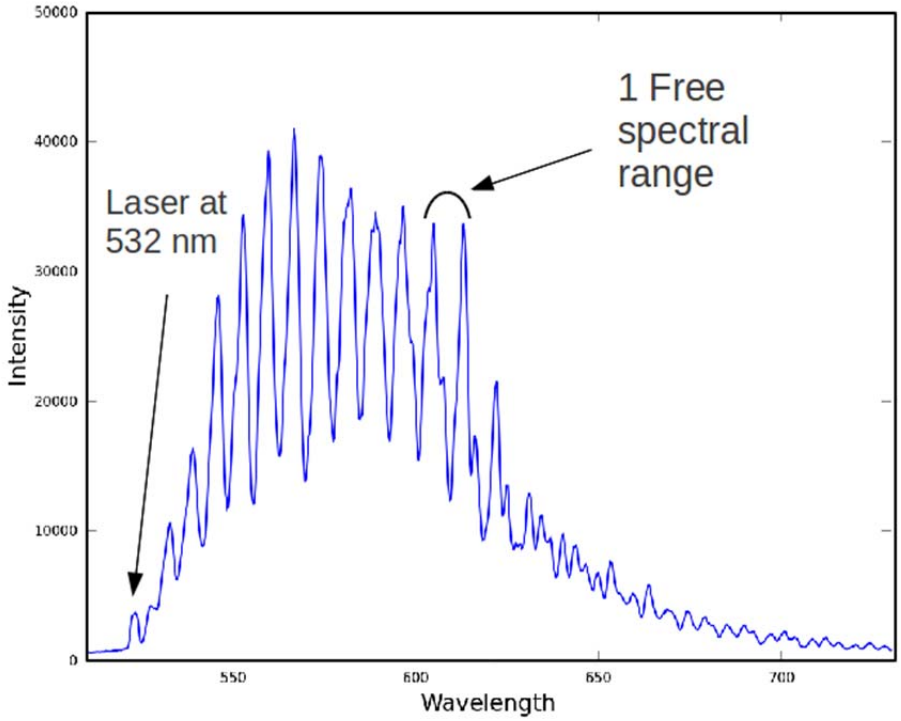

Figure 4: Emissions spectrum of a fiber coupled microsphere and the free spectral range of the sphere. The pump laser at 532 nm has been filtered by a 532-nm long pass filter.

Figure 5 shows the output spectrum of the fiber taper before and after sphere attachment. Prior to attachment, the taper passes a significantly larger portion of the laser; in addition a broad background is present at longer wavelengths (blue curve). This background is due to Raman scattering from silica, occurring from the laser propagating through the fiber. After a fluorescent microsphere is

attached, due to optical scattering and fluorescent generation from the microsphere, the observed 532-nm laser light passing through the taper reduces significantly (green curve). In addition, the interaction between the laser propagating mode and the sphere was optimized by rotating the polarization controller to maximize coupling to the sphere, thus reducing the output 532-nm laser energy further.

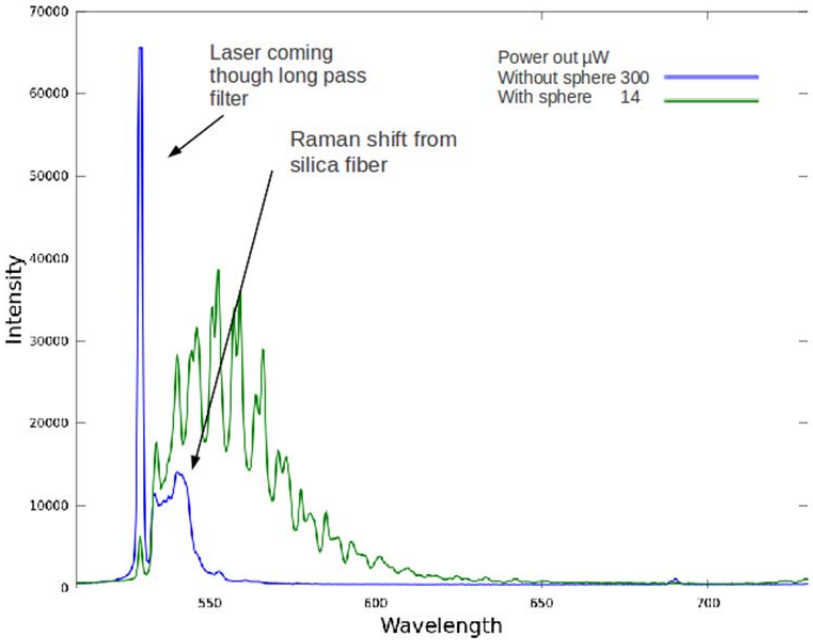

Figure 5: The spectra readings of a fiber taper without a sphere (blue) and with the sphere (green).

To investigate the lasing threshold of the fiber-taper coupled fluorescent microsphere, the incident pump power was varied. Several spectrums captured at increasing pump intensity are overlaid in Fig. 6. For each spectrum, the pump power was increased providing higher power to the cavity. As the power is increased, typically one would expect the cavity modes excited by the spontaneous fluorescence, to compete until a dominant mode reaches lasing threshold. However, after reaching a certain power level, no significant increase in florescent activity can be observed. In addition, a bleaching effect of the florescent dye can be seen as the fluorescent activity begins to reduce in subsequent measurements.

This bleaching effect was further investigated by monitoring the exposure time of the pump laser. Figure 7 shows a time lapse of several spectra acquired at the same pump intensity into the system of 4 mW as the microsphere is continuously exposed to the pump laser. From the initial measurement (0:00 min) to 5 min later the bleaching effect quenches nearly all fluorescent activity.

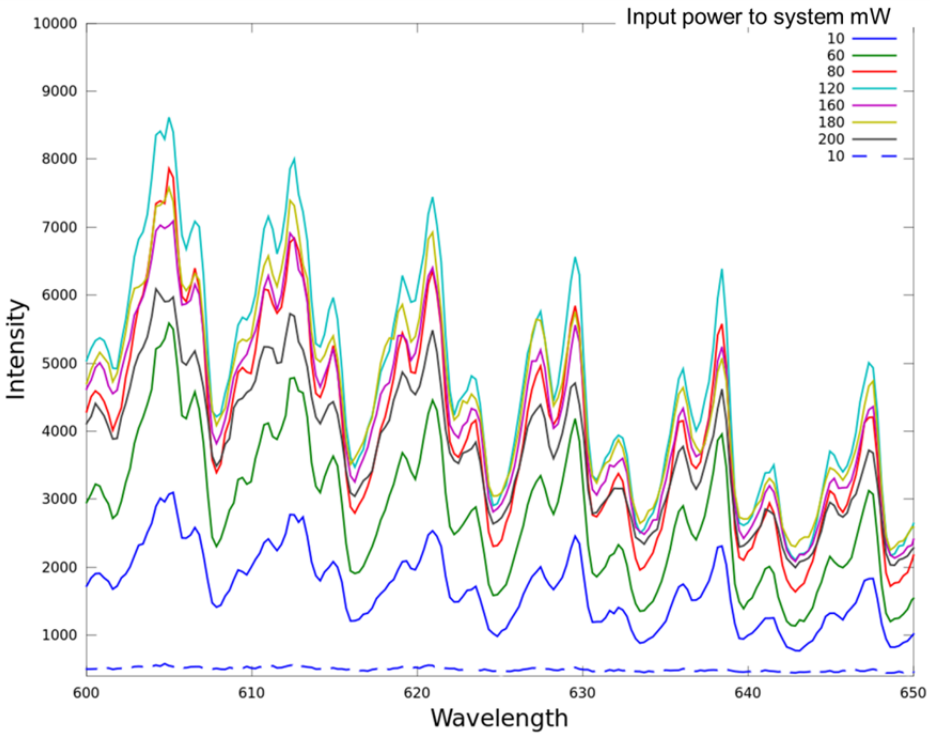

Figure 6: Measurements showing the spectrum changes as input power is increased into the system. The laser was only unshuttered long enough to take measurements. There is a maximum fluorescence which decreases due to bleaching. Upon returning to the initial power of 10 mW it is clear that bleaching has occurred.

To limit the photobleaching effect, a series of measurements were performed with the pump laser shuttered between exposures, that is, the laser was on only as long as necessary to collect data (1–3 seconds per exposure). In addition, it was discovered that the effect of bleaching could be slowed by using spheres that were freshly dried from their containing solution. The dry time was not regulated in the previous results, where the samples were nearly 3 weeks old (dried on glass slide). Fresh batches of newly dried spheres with limited exposure time to room lighting were used to perform the same experiment as was conducted in Fig. 7. While a sphere from the fresh batch did slow the bleaching process, it was not substantial enough to have a major impact on the experiment, and did not fully stop the initial drop in signal that occurs within a very short time after the laser is introduced to the system (represented by the dramatic change of intensity, on Fig. 7, from the first reading to the second, 25 seconds later).

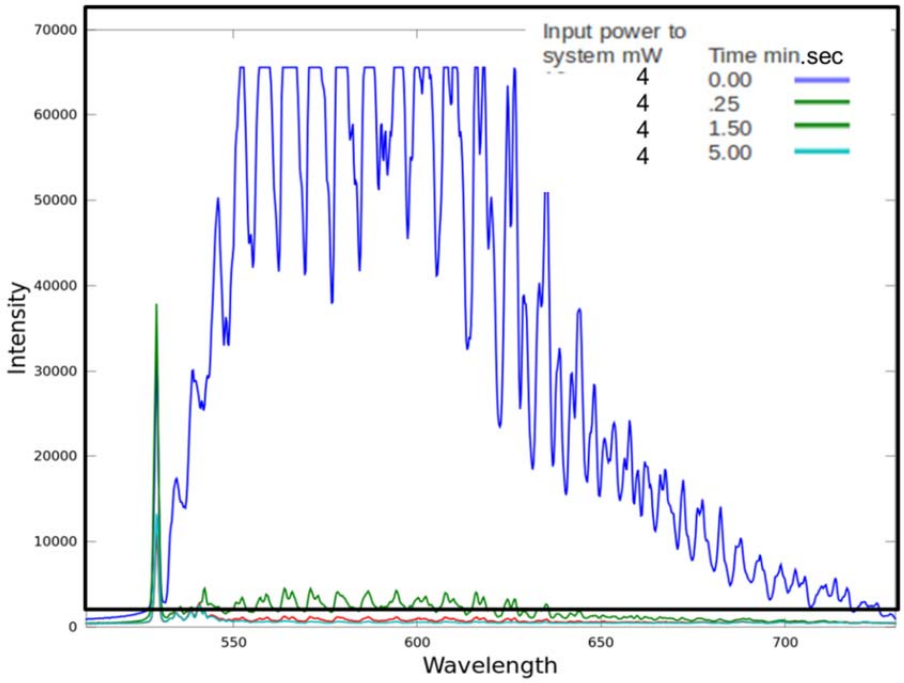

Figure 7: Time-series spectra of microsphere fluorescence while system power was maintained at 4 mW. Actual transmission at the taper, before the sphere was placed was 150 μW.

Shuttering the laser, in combination with the use of newly dried spheres, considerably slowed the photo bleaching effect. This can be seen by a time series of spectra measurements shown in Fig. 8. Each result was acquired by using the technique of short exposures (approximately one second) and maintaining the pump at a relatively low power setting (~4 mW system power). Florescence can be seen for a longer period of consecutive measurements. However, a noticeable drop does occur from the first measurement to the second, which is yet to be fully understood (also occurred during acquisition of other sets of data not shown).

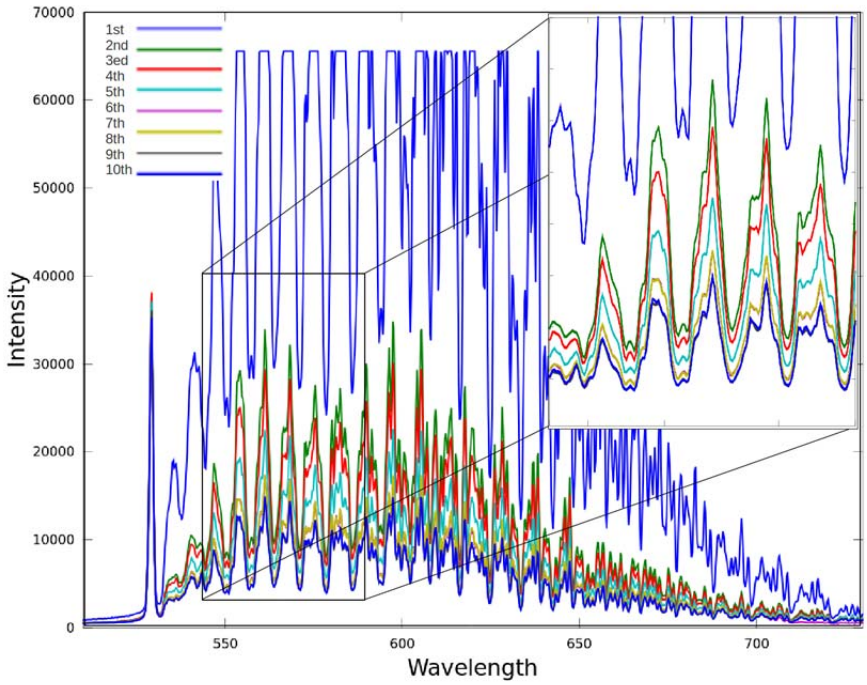

Figure 8: Bleaching when the laser is shuttered in-between spectra measurements, exposing the sphere for approximately one second per measurement. After the initial drop most measurements demonstrated a less drastic reduction in fluorescence allowing for a greater number of useful spectra measurements at this power level.

CONCLUSION

Fluorescent microspheres adhered to a fiber taper were explored as a simple method for developing a miniature fiber based laser. The experimental results indicate fluorescence generated from the microspheres was able to couple to the cavity modes of the microsphere. However, degradation of the fluorescence signal most likely due to photo bleaching, made it difficult to observe conditions for reaching a lasing threshold. The results presented only focused on one particular type of fluorescent microspheres which utilized an organic fluorescent dye that seemed to degrade quickly outside of their containment solution. Therefore, additional types of fluorescent spheres with more hardy dyes need to be explored as they may be able to better withstand the pumping conditions while adhered to the fiber taper. Pulsed pump laser sources, could also be explored as a possible solution; by achieve higher pump intensity while maintaining low total exposure energy, the effect of photo bleaching may be reduced. To this end, the results demonstrate the potential for developing a fiber coupled florescent microsphere laser.

ACKNOWLEDGMENTS

This material is based upon work supported by the National Science Foundation under Grant No. EEC-1062984. Furthermore, my thanks go out to Pennsylvania State University for hosting this program. Thank you program directors Sven Bilén, Kenneth Jenkins, assistant director Tom Tyson and Lena Getman for all the time you have put into making this a wonderfully successful program. Finally I'd like to thank Dr. Zhiwen Liu whose lab I so gratefully used.

REFERENCES

[1] Samuel, Ifor D. W, E. B. Namdas, G. A. Turnbull "How to recognize lasing," Nature Photonics 3, 546 - 549 (2009).

[2] Spillane, S. M., T. J. Kippenberg, O. J. Painter, and K. J. Vahala, "Ideality in a Fiber-Taper-Coupled Microresonator System for Application to Cavity," Physical Review Letters Vol. 91, Num. 4, (2003).

[3] Cai, M., O. Painter, K. J. Vahala, and P. C. Sercel, "Fiber-coupled Microsphere Laser," Optics Letters Vol. 25, No. 19, 1430-1432 (2000).

[4] Gorodetshy, M. L., A. A. Savchenkov and V. S. Ilchenko, "Ultimate Q of Optical Microsphere Resonators," Optics Letters Vol. 21, No 7 453-455 (1996).

[5] Tong, L., J. Lou, E. Mazur "Single-mode Guiding Properties of Subwavelength-diameter Silica and Silicon Wire Wave guides," Optics Express, Vol. 12 No. 6, 1025-1035 (2004).

OPTIMIZATION OF ELECTROMAGNETIC COUPLING IN CERAMIC RESONATORS FOR MAGNETIC RESONANCE IMAGING APPLICATIONS

Matthew Pyrz,* Michael T. Lanagan,[#] and Steven E. Perini[+]

Department of Electrical Engineering
The Pennsylvania State University, University Park, PA 16802

*Undergraduate Student of
Department of Biomedical Engineering
Bucknell University
Lewisburg, PA 17837

ABSTRACT

Research into the properties of dielectric resonators can provide insight to potential applications in magnetic resonance imaging (MRI) technology as replacements for the RF coils used in current designs. While radiofrequency (RF) coils are sufficient to produce the B_1 field in low field machines, increasing the strength of the field offers several advantages, including improved SNR, spatial resolution, and sensitivity. However, this increase in field strength requires an alternative coil design as traditional RF coils create numerous difficulties such as interference patterns and phase shifts in the signal. A potential solution may be to replace these coils with dielectric resonators. The objective of this research project is aimed at gathering information pertinent to dielectric resonators with various boundary conditions. Specifically, probe design and alternative coupling methods were investigated using network analyzers to provide insight into methods that could increase power supplied to the resonator, allowing it to generate strong RF magnetic fields within MRI equipment. By implementing a full loop probe design around the ceramic resonator, the effective power transmission was increased by 70.6% to −9.60 dB in the experimental design and by 75.7% to −15.6 dB when it was used in the MRI probe. However, this strong increase in signal transmission, made possible through the replacement of the original 12-mm-diameter coil, had unintentional consequences in that the resonant frequency could be tuned to a minimum of 605 MHz instead of the ideal 600

[#] Primary Mentor
[+] Secondary Mentor

MHz. In order to correct for this, a thin plate of $CaTiO_3$ was added to the side of the existing resonator disk to achieve a lower resonant frequency.

INTRODUCTION

Improvement on current magnetic resonance imaging technology in terms of image quality and signal-to-noise ratio is dependent on increases in the B_0 magnetic field strength. Modern clinical scanners operate at field strengths ranging from 1.5 T to 3.0 T; however, the implementation of high-field MRI designs offers several distinct advantages including an increased signal-to-noise ratio, spatial resolution, and sensitivity [1]. In addition, high-field MRI devices experience reduced scan times, a critical advantage over weaker field designs when investigating large biological systems, specifically human subjects. Transitioning to MRI systems operating at powerful B_0 field strengths ranging from 7 T to 20 T would offer these high-field advantages, however, the design of one critical element, the RF coil, has to be significantly improved. The focus of this research is on alternative designs to the RF coil via potential coupling configurations with a ceramic resonator.

An MRI device is composed of three primary hardware components, a superconducting magnetic, the RF coil, and the gradient coils, each designed to produce specific fields directed at distinct orientations within the biological sample under study. These fields stimulate the magnetic moment of the hydrogen atoms within the sample, and the image is produced by examining their behavior upon relaxation. The superconducting magnet serves to generate a powerful homogeneous magnetic field, known as B_0. The B_0 field serves to align the magnetic moment of the hydrogen atoms axially within the cylindrical bore. The majority of the hydrogen atoms have a partner that has aligned itself in the opposite direction and cancels out the pair; however, a small number remain unmatched. Simultaneously, the RF coils generate the B_1 field perpendicular to the B_0. As opposed to the static nature of the B_0 field, B_1 is a time-varying pulse, which affects the unmatched protons in the sample and causes them to switch their spin states. The gradient coils create non-uniformities within the B_0 field in order to distinguish between individual regions of the sample. The information required to generate the image of the sample is collected when the B_1 field is removed. At this point, the hydrogen nuclei return to their lower energy spin states and release energy in the process. This energy is measured by the RF coil and serves as the information required to produce the image of the inner structures within the biological sample [3].

A critical design challenge of producing effective high-field, clinical MRI scanners surround the production of viable RF coils. At field strengths at 7 T and above, the signal encoded by the energy released by the relaxation of the protons becomes difficult to receive by traditional RF coil designs. The electromagnetic wavelengths become a significant portion of the coil length, resulting in phase shifts, constructive and destructive interference patterns, and an overall decrease in the quality-factor, which is a measure of the relationship between energy stored

and lost [1]. Equations 1 and 2 describe the basis of the wavelength identification for high-field MRI devices and how the problem arises with restricted RF coil lengths.

$$\omega_0 = \gamma B_0 \tag{1}$$

The frequency of the Larmor precession (ω_0) of the protons within the sample is defined in terms of the B_0 field strength and the gyromagnetic ratio (γ), which is a value specific to the hydrogen nuclei [4].

$$S = \omega_o M_o B_1 V_s \tag{2}$$

This Larmor precession is directly related to the signal received from the proton relaxation, where the signal is defined by Equation 2. Here, M_0 represents the equilibrium magnetization and V_s voxel size [4]. From these equations, it becomes clear that as the strengths of the B_0 and B_1 magnetic fields increase, the corresponding wavelength of the signal decreases until it becomes a significant portion of the RF coil length, resulting in a multitude of difficulties stemming from interference and phase shift patterns. Furthermore, the oscillation frequency of B_1 increases proportionally to B_0, preventing the B_0 field from being increased independently of B_1. The coil also experiences a measureable amount of noise, described by the following equation as:

$$noise \propto \sqrt{4kT_{coil}\Delta f R_{eff}} \propto 1/Q \tag{3}$$

This proportionality is defined in terms of the coil thermal energy (kT_{coil}), the bandwidth (Δf), and the resistance contributions from the coil, electronics, and sample (R_{eff}) [4]. Q represents the quality factor of the coil, defined earlier as the ratio between stored and lost energy. Therefore, by increasing the quality factor of the RF coil, the noise experience in the receive signal is decreased. However, at high frequencies, this Q-value is reduced for RF coils due to increased losses, representing another disadvantage of their implementation in high-field MRI devices. Combining Equations 2 and 3 yields the relationship between the signal-to-noise ratio, quality factor, and resolution/data acquisition time, defined by

$$\text{SNR } \alpha \text{ Q } \alpha \text{ } 1/(\Delta x * \sqrt{T}) \tag{4}$$

By increasing Q, the signal-to-noise ratio is increased as well, allowing for a more focused and easily identified energy released from the protons dropping to a lower energy state. Furthermore, maintaining a high Q value allows for an improved resolution (Δx) and a reduced scan time (T) [4].

A potential solution to the challenge of RF coil design in high-field applications is replacing the traditional coil with a ceramic dielectric resonator, which have significantly higher Q-values than coils. Research into their design

and electrical properties has demonstrated that they offer a promising alternative to conventional configurations due to their high permittivity and quality factors [1]. This provides them with the ability to produce strong, uniform magnetic fields at high frequencies (falling within the microwave range). These ceramic resonators, typically fashioned into a cylindrical geometry, can be excited by placing them in close proximity with a wire probe, which causes them to resonate at distinct frequencies. This resonance allows the dielectric resonator to generate an electromagnetic field in the same manner as the conventional RF coil design. This resonator-probe coupling can be implemented in a way so that they generate self-sustaining B_1 fields in an MRI application. In addition, these resonators maintain high quality factors ranging from a few hundred to thousands. When compared to the quality factors of RF coils at 100 or less, the relative energy storage ability of these elements illustrates their potential in the field. In addition, these resonators can be produced in a wide range of sizes, which reduces the difficulties of design in MRI equipment with stringent size restrictions [1].

Though ceramic resonators display an arsenal of beneficial attributes that offer distinct advantages over traditional designs, there are still hurdles that exist that must be surpassed in order for them to become viable alternatives. Principally, the probe design that exists in MRI probes implementing them as the RF coils cannot transmit adequate power to produce clear images. In essence, the B_1 magnetic field generated does not have sufficient strength to align the protons within the sample so that when they relax, the signal can be reconstructed to produce clear images. The current designs produce relatively "fuzzy" images when reconstructed by the MRI software. Therefore, the objective of this research is to investigate probe configurations in order to maximize the power transmitted to the resonator, while maintaining a high quality factor.

EXPERIMENT DESCRIPTION

Due to the impracticality of conducting individual MRI scans to test all potential probe configurations, the properties of the signal transmission from probe to resonator needed to be conducted in an alternative laboratory setting. The primary device used in the experiment was the Anritsu 37369D Lightning network analyzer. A network analyzer is a device that allows for the measurement of the electrical properties of networks by quantifying the amount of a signal that is transmitted and reflected. This specific network analyzer accomplishes this by calculating s-parameters, corresponding to energy transmission and reflection to and from the two ports where the signal can be both generated and received. The device operates by sending signals with a range of frequencies from one of its ports. The amount of energy that passes through the device under examination (the ceramic resonator in this case) is received by the other port and is recorded as the S_{21} parameter. The amount of the incident signal that is reflected back from the sample, returning to the port of origin is reported as the S_{11} parameter. S_{21} is interpreted as amplitude of the signal measured at port 2 which originated at port 1; likewise S_{11} is the energy measured at port 1 which originated at port 1. The

network analyzer displays these measurements as graphs of frequency against signal amplitude. These graphical depictions of the data can be used to extrapolate properties of the resonator under examination, specifically the center frequency, bandwidth, loss at ref, and *Q*.

The S_{21} parameter was used for this experimental purpose because it allows for the identification of peaks, which correspond to the resonant frequencies of the ceramic resonator. In addition, the S_{21} measurement directly corresponds with the B_1 field strength within the resonator. The S_{11} parameter also produces distinguishing features on the graph; however, instead of producing peaks; there are dips in the signal. The peaks are necessary in order for the device to calculate the properties listed above. The center frequency identifies the specific frequency of the mode that the resonator produces the strongest signal intensity. The transverse electric mode (TE_{01}) is the most relevant mode for the purposes of MRI integration and was the focus of this experimental design. Figure 5 illustrates the electric and magnetic fields of the TE_{01} mode generated upon excitation of the ceramic resonator. The bandwidth provides a measure of the width of the signal peak, which can be interpreted as the range of frequencies where the resonance behavior occurs. An unloaded value of *Q* can be calculated by taking the frequency divided by the bandwidth, yielding a value that provides a method of the measurement of loss. A higher unloaded *Q* represents a lower loss configuration. The loss at ref value is a direct measure of the energy coupling ability of the probe-resonator arrangement measured in decibels (dB). Finally, the *Q* value reports the unloaded *Q* value, but can be read as a direct readout from the Anritsu 37369D Lightning network analyzer.

Experimentally, the Hakki–Coleman method was used as the primary setup for the measurement of the electrical properties of the ceramic resonators [2]. However, additional probe configurations required a modification of this method in order to accommodate for a suspended probe to be placed within the center bore of an annular resonator, the type used in an MRI application. The Hakki–Coleman method involved the resonator placed between two conductive plates, while two probes were positioned on opposing sides of the sample. The conductive plates ground the field lines at the boundaries of the cylindrical resonator [2]. In addition to the Hakki–Coleman method, configurations were measured that involved a probe suspended above the resonator, which prevented the ground plates from being in contact with the sample. As the experimentation progressed, the Hakki–Coleman method could no longer support the experimental design and was exchanged with a free space method of measurement to accommodate the suspended probe. The high *Q*-value of the resonator samples allowed for this transition since the relative losses to the surrounding environment are minimized. Instead of being placed between two conductive plates, the resonator rested on a non-conductive foam platform with the probes positioned around it accordingly. This allowed for a probe to be suspended above the circular bore of the annular resonator to measure the S_{21} parameter.

These two methods of experimentation were used to test a wide-variety of probe sizes, shapes, and orientations with respect to the sample in order to determine an optimum configuration that provided a high amount of energy transmission, while maintaining a high quality factor.

EXPERIMENT RESULTS

The current coupling wire implemented in the ceramic resonator MRI probe is a 12 mm loop of magnet wire situated approximately 5 mm from the resonator's side. Initial measurements of the coupling ability of this particular configuration indicated that it transmitted 0.01 of the signal amplitude from excitation probe to resonator to receiving probe, corresponding to a −21 dB loss at ref as measured by a free space network analyzer. In order to improve the MRI image quality, this value needed to increase to reflect a more significant portion of the excitation signal that passes through to the resonator.

In order to verify an increased power transmission for a particular probe design and configuration, the measurements on the network analyzer for the Hakki–Coleman method or a free space measurement must demonstrate an increase from this benchmark value of −21 dB. A model probe for the 12-mm-diameter loop used in the current ceramic resonator MRI probe was constructed so that its performance could be compared to other probes without the inconvenience of manipulating the MRI probe to measure each additional configuration. In essence, the model probe, formed from a 1.05-mm-thick magnetic wire and an SMA connector (Figure 1), allowed for direct comparison to others on a traditional network analyzer platform. Only when a configuration proved to exceed this model probe's performance on the free space platform or in the Hakki–Coleman arrangement would the MRI probe be deconstructed in order to add the new probe to its design.

The most effective configuration at balancing power transmission, while maintaining a high quality factor value, involved two novel probe designs that allowed for comparing performance on the traditional platform as well as in the MRI probe. A difficulty of direct comparison between these two configurations is that the MRI probe can only supply a S_{11} value due to its single element design. However, a measurement of the S_{21} parameter is required to quantitatively verify an increased power transmission as it provides a measurement of transmission, while S_{11} measures reflection. Figure 1 show the probes and their respective locations involved in measuring the performance of a full loop probe situated around the ceramic resonator. This coupling configuration involves two probes situated around a dielectric resonator in two distinct locations. The resonator itself contains an inner bore, in which probe one is suspended at the center point (7.72 mm from surface of the sample). This probe contains a 2-mm loop bent at a 90° angle to the shaft, making it parallel to the surface of the sample. Note that the probe does not make contact with the inner wall of the bore. Probe 2 contains a full loop that encircles the resonator. Again, the probe does not make contact with the resonator.

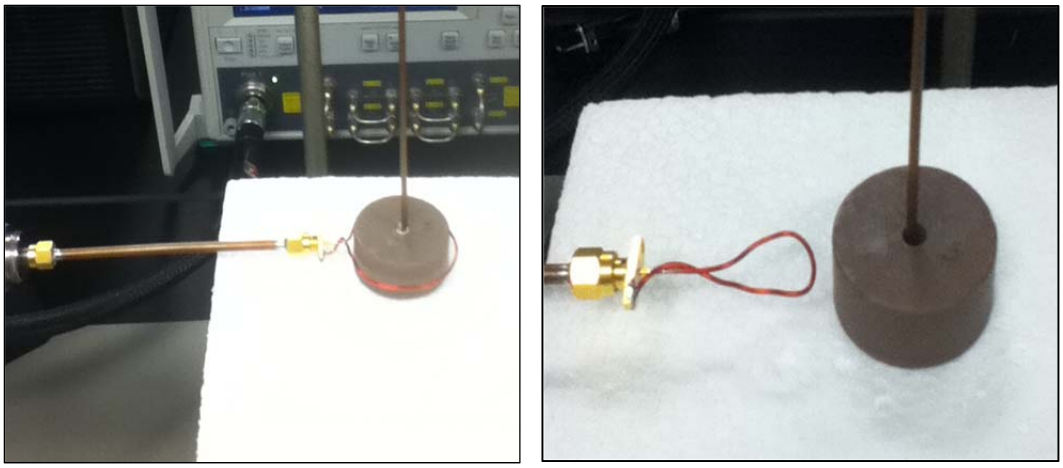

Figure 1: Top view of experimental setup of the full loop probe design (left) illustrating the positions of both the suspended probe and the full loop probe. The experimental setup of the traditional probe design, implementing a 12-mm loop situated approximately 5 mm from the side of the sample and a suspended probe, is pictured on the right.

Of this arrangement, the more significant probe is the full loop, as it provides the potential replacement design for the 12-mm loop of the current MRI probe; however, the suspended loop probe is critical in terms of experimental setup. The suspended probe (Probe 2 in Figure 1), allows for the measurement of the S_{21} parameter for both the traditional stage and in the MRI probe. In order to optimize the position of the suspended probe with respect to the annular bore, the energy transmission was measured at various heights. Figure 2 illustrates the relationship between the position of the suspended probe and its energy coupling ability. Additionally, this data compares various probe loop diameters positioned in close proximity to the side of the resonator disk. These measurements provided conclusive evidence as to eliminate the simple redesign possibility of increasing the diameter of the original 12-mm loop implemented in the MRI probe. Figure 1 illustrates that energy transmission of the loop plateaus as the loop size is increased past 5 mm, indicating that altering the current 12-mm loop of the MRI probe would be insufficient to improve the energy coupling. In addition to energy coupling, the quality factor, or the ratio of center frequency to bandwidth, is impacted by the suspended probe's distance from the center of the annular bore. Concurrent examinations of Figures 2 and 3 indicate that the optimized probe design requires a balance between energy transmission and quality factor.

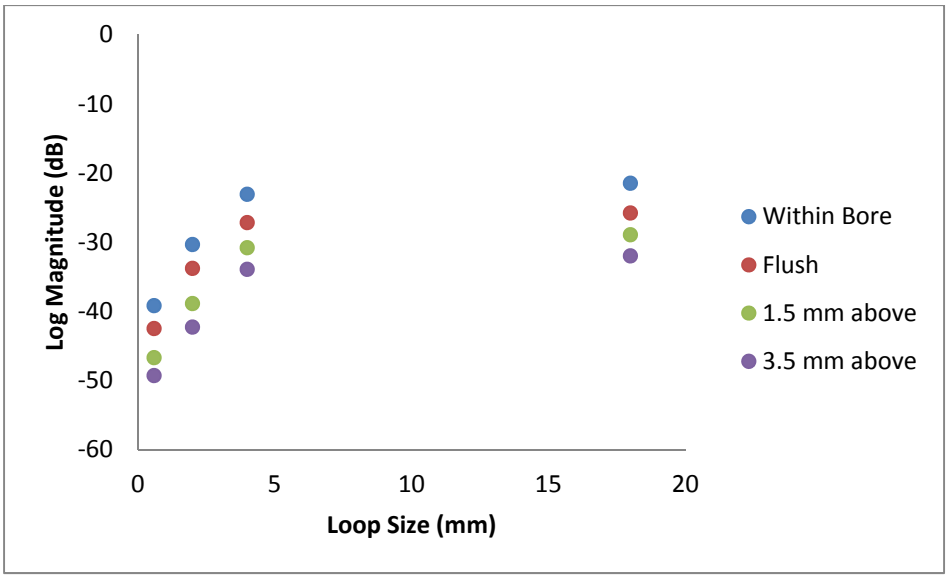

Figure 2: Comparison of the excitation probe loop size and S_{21} energy transmission values for suspended probe locations within, flush, 1.5 mm above, and 3.5 mm above the inner bore of the annular resonator. Note that the energy coupling ability plateaus once the probe diameter is increased past 5 mm.

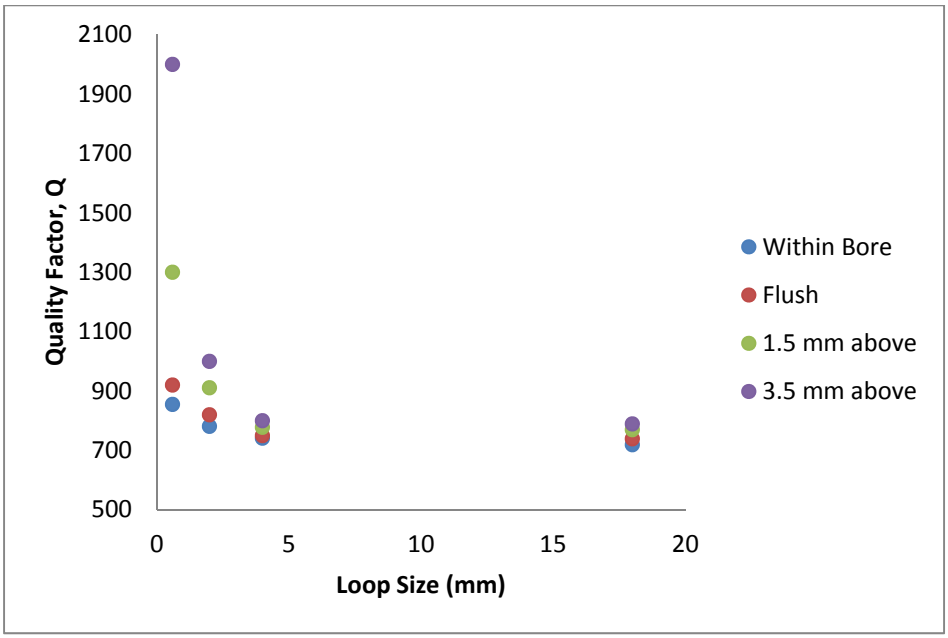

Figure 3: Comparison of the excitation probe loop size and quality factor for suspended probe locations within, flush, 1.5 mm above, and 3.5 mm above the inner bore of the annular resonator.

Implementing a full loop probe design pictured in Figure 1 significantly improves the coupling ability at all positions within the magnetic field. Figure 4 compares the B_1 field strength across the length of the resonator disk to the coupling results of the full loop probe. The suspended probe was positioned at various depths within the center bore as well as locations above the surface of the disk, as the fields are not restricted within the geometric confines of the resonator (Figure 4).

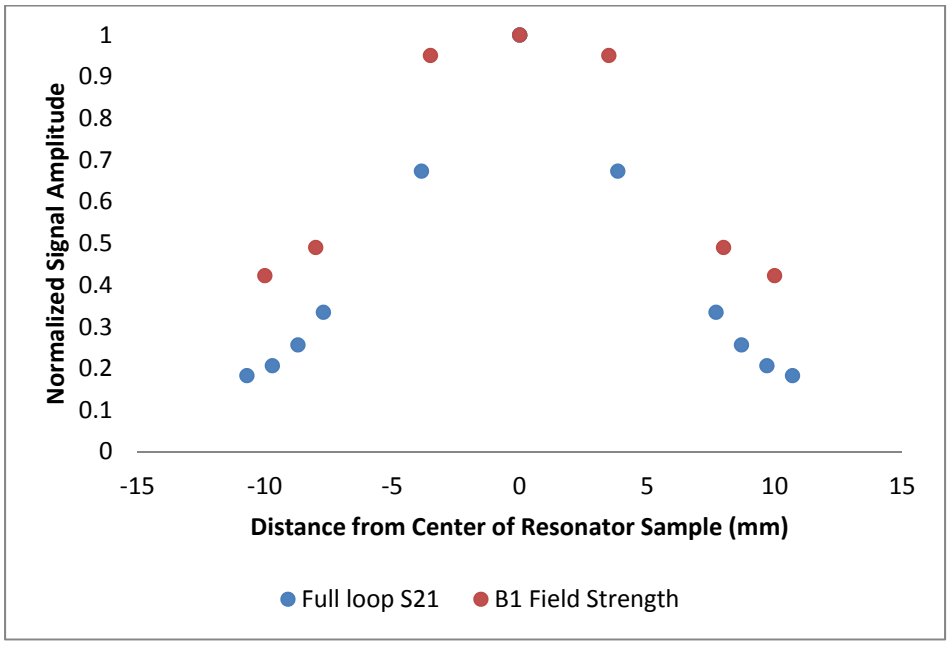

Figure 4: B_1 field strength data across the width of the resonator disk and the coupling ability of the suspended probe at various heights within the center bore.

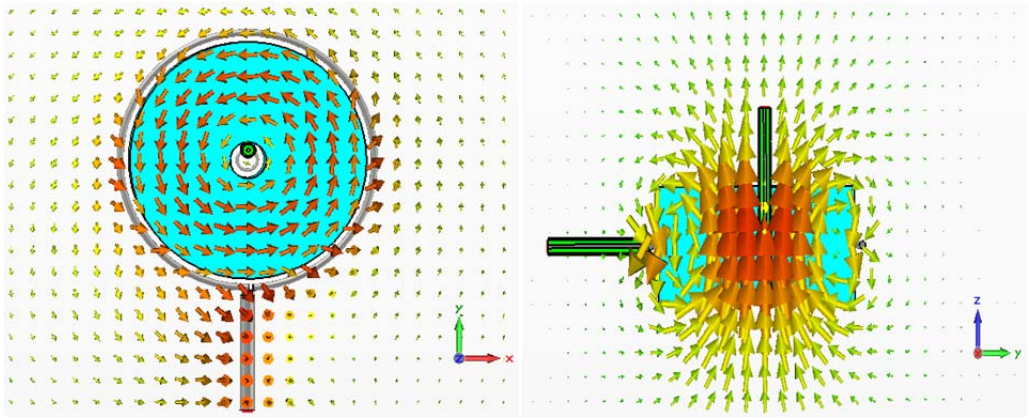

Figure 5: Electric (left) and magnetic (right) field patterns of the TE_{01} mode produced by the full loop coupling configuration. Images generated with CTS microwave modeling simulations conducted by Michigan Tech.

Table 1: MRI excitation probe designs and measured parameters in a free space traditional platform configuration. Note the shift in center frequency as well as the increased loss at ref power transmission for the 0.41 mm wire compared to the probes with 1.05 mm wire. Further decreases in wire thickness failed to reduce the center frequency.

Probe Design	Center Frequency	Bandwidth	Loss at ref	Q
Original 12 mm, 1.05 mm thick	0.725 GHz	0.002 GHz	−14.24 dB	305
Full loop, 1.05 mm thick wire	0.7997 GHz	0.020 GHz	−11.27 dB	40
Full loop, 0.41 mm thick wire	0.769 GHz	0.010 GHz	−9.60 dB	70
Full loop, 0.33 mm thick wire	0.775 GHz	0.012 GHz	−10.30 dB	65

DISCUSSION

Based on data collected using the traditional resonator stage as well as in the MRI probe design, the original objective of increasing the power transmission to the ceramic resonator can be accomplished using the full loop probe. This probe involves a wire that completely encircles the cylindrical resonator. The diameter of this loop is dependent on the size of the resonator, requiring an additional 2 to 3 mm of airspace between the wire and the surface of the resonator to prevent contact between the two materials. The ceramic resonators are non-conductive so this gap is not a matter of preventing a short circuit; rather, experimentation indicated that there is an optimum distance between the wire and the ceramic material. Using a free space measurement on the traditional resonator stage, a 39.0-mm loop was used to accommodate a 35.0-mm $CaTiO_3$ annular resonator disk. This design was adapted within the MRI probe and used a roughly 50-mm-diameter full loop probe with a 46.1-mm CaTiO3 annular resonator. Certain physical restrictions within the MRI probe prevented the full loop probe from being entirely circular in nature, and instead had an approximately square shape with smooth corners. In both instances, this configuration proved to be more effective at power transmission than the original 12-mm-diameter excitation loop in the MRI probe. The free space experimentation provided S_{21} values that were significantly greater than the model 12-mm-loop probe. This original design displayed a maximum energy coupling of −14.24 dB loss at reference compared to the −9.60 dB coupling for the full loop with 0.41-mm-thick magnet wire, reflecting a 70.6% increase in signal power. When implemented in the MRI probe itself, the full loop design increased the S_{21} parameter from −20.5 dB to −15.6 dB, or a 75.7% increase in signal power. From this standpoint, the full loop probe has a distinct advantage over a probe loop positioned away from the side of the resonator. Figure 2 confirms that increasing the diameter of this variety of probe results in minimal gains of its coupling ability. Therefore, simply increasing the size of this loop would not be sufficient in increasing the energy transmission

from probe to resonator in the MRI probe design. The full loop serves as a viable alternative to this original probe type.

Though the original objective of increasing energy coupling was accomplished by the full loop probe, there is a significant drawback in its implementation within this specific MRI probe. The probe involved in this experimental process is constructed for use in a 14-tesla MRI device and contains a $CaTiO_3$ ceramic resonator with a fixed diameter of 46.1 mm. In this specific MRI device, the hydrogen atoms within the sample precess at a Larmor frequency of 600 MHz based on the definition given by Equation 1 using the gyromagetic ratio for hydrogen nuclei of 42.576 MHz/T. Therefore, in order for the probe to excite the hydrogen atoms, the ceramic resonator must be tuned to resonate at 600 MHz. This is accomplished by manipulating a variable capacitor and by moving two foil contacts located on either side of the ceramic disk. Concurrent tuning of these instruments provides the ability to adjust the center frequency of the TE_{01} mode to 600 MHz. Free space measurements of the 46.1-mm $CaTiO_3$ resonator detached from the MRI probe with a full loop configuration provided a center frequency of 575 MHz. However, once this configuration was added to the MRI probe, including the protective shield that houses the resonator and tuning apparatus, this frequency was increased to 625 MHz. This value represents the lowest frequency that the resonator could be tuned to with the full loop probe of 1.05-mm magnetic wire. Reducing the thickness of the wire to 0.41 mm consequently lowered the resonant frequency to 605 MHz without impacting the power transmission of the probe geometry. This frequency could not be adjusted to the ideal 600 MHz. Though the ability to transfer power from the probe to the ceramic resonator was significantly increased by implementing the full loop probe, it compromised the tuning ability of the MRI probe design.

Successive attempts to reduce the resonant frequency of the existing $CaTiO_3$ through manipulation of physical parameters of the probe including wire thickness and distance from the ceramic material proved to be ineffective. Therefore, in order to reduce the TE_{01} resonant frequency to 600 MHz, the dimensions of the ceramic resonator were altered. Larger resonators with identical chemical compositions resonate at lower frequencies; however, based on time and economic restrictions; it was not a viable option to replace the resonator with a larger one. Instead, a thin plate of $CaTiO_3$ was attached to one side of the resonator, while maintaining the full loop of 0.41-mm-thick magnet wire. This adjustment allowed the probe to be tuned to the proper frequency of 600 MHz, giving it the capability of housing a sample to be scanned with the 14-tesla MRI instrument.

CONCLUSION

The primary objective of the probe design and configuration testing was to optimize the power transmission to the ceramic resonator in the MRI probe. The full loop design demonstrated that this objective could be achieved by encircling

the cylindrical resonator with a 0.41-mm-thick magnet wire with approximately 2 mm of air space separating the ceramic material from the wire.

In addition to the improved power transmission of the full loop probe configuration, it was found that data acquisition for an annular resonator on the traditional stage was most effectively accomplished using a free space experimental method as opposed to the Hakki–Coleman method because the conductive plates block the access point to the inner bore. The suspended probe allows for free space measurements to be conducted for a greater variety of potential probe configurations, namely the full loop probe. Additionally, the suspended probe design allowed for the S_{21} parameter to be measured in the MRI probe by providing a second probe to collect transmission data. It aided in bridging the experimental distance between the free space configurations and MRI probe performance by providing a route for direct comparison for the two resonator platforms via the S_{21} parameter.

Though the principal drawback of the full loop excitation probe is the compromised tuning ability to force a resonant peak at 600 MHz, the substantial increase in coupling proves that there may well be a place for the full loop in the MRI probe design. A potential solution to the tuning disability would be to replace the 46.1 mm $CaTiO_3$ with a larger sample; however, this exceeds the scope of the experimentation and would require a major redesign of the MRI probe. A resonator with increased geometric dimensions would resonate at a lower frequency, and since the difficulty lies in reducing the center frequency as opposed to increasing it, this replacement would allow the device to resonate at 600 MHz. The addition of the thin $CaTiO_3$ plate to the existing resonator proved that an increase in resonator size does reduce the resonant frequency. This alteration compromised the coupling power between the probe and the resonator, however, this be attributed to the asymmetrical nature of the modified resonator as the plate was added to a single side of the disk. Therefore, the coupling wire was no longer directly in the center of the sample where the coupling is typically the strongest. In order to further enhance the performance of the MRI probe, the existing resonator must be replaced with a larger sample with the same chemical composition of another ceramic resonator with a higher Q-value. Increasing the geometric dimensions of the resonator would have additional consequences because, not only would the resonator housing components need to be replaced, but the protective shield and tuning apparatus would require a redesign. However, this experiment provided convincing evidence towards the full loop configuration having superior coupling ability than the 12-mm loop of the previous probe design.

ACKNOWLEDGMENTS

This material is based upon work supported by the National Science Foundation under Grant No. EEC-1062984. Furthermore, I would first like to thank these people including Thomas Neuberger for operating the MRI instrument in order to test the performance of the redesigned probe. Without his contribution,

the conclusions of the experiment and the ability of the probe to produce an MRI image would remain in the purely theoretical realm. In addition, I would like to thank the CST modeling team at Michigan Tech for using the software to simulate many of the probe coupling configurations conducted in lab. This provided valuable data to verify the experimental results and gave computer generated depictions of the magnetic and electric fields that are entirely invisible in the physical experimentation.

REFERENCES

[1] Haines, K.N., "Applications of High Dielectric Materials in High Field Magnetic Resonance," Ph.D. dissertation, Dept. Elect. Eng., Pennsylvania State Univ., State College, Pa, 2010.

[2] Hakki R W., and Coleman, P.D. 1960. A dielectric resonator method of measuring inductive capacities in the millimeter range. *IRE Trans Microwave Theory Tech* 8: 402–410.

[3] J. P. Hornak, (2011). *The Basics of MRI* [Online]. Available FTP: www.cis.rit.edu/htbooks/mri

[4] M. X. Lanagan, Private communication, June 2012.

AUTHOR INDEX
(* Indicates REU Student Author)